VILNIUS UNIVERSITY
CENTER FOR PHYSICAL SCIENCES AND TECHNOLOGY

GEDIMINAS KREIZA

HIGHLY FLUORESCENT ORGANIC NANOPARTICLES, FILMS AND CRYSTALS FOR SENSING AND LASING APPLICATIONS

Doctoral Dissertation
Physical Sciences, Physics (02P)

Vilnius, 2018

The dissertation was prepared at Vilnius University, Institute of Photonics and Nanotechnology in 2014 – 2018.

Scientific supervisor – dr. Karolis Kazlauskas (Vilnius University, Physical sciences, Physics – 02P).

VILNIAUS UNIVERSITETAS
FIZINIŲ IR TECHNOLOGIJOS MOKSLŲ CENTRAS

GEDIMINAS KREIZA

NAŠIAI FLUORESCUOJANTYS ORGANINIAI NANODARINIAI, SLUOKSNIAI IR KRISTALAI TAIKYMAMS JUTIKLIUOSE IR LAZERIUOSE

Daktaro disertacija
Fiziniai mokslai, fizika (02P)

Vilnius, 2018 m.

Disertacija parengta 2014 – 2018 metais Vilniaus universitete, Fotonikos ir nanotechnologijų institute.

Mokslinis vadovas – dr. Karolis Kazlauskas (Vilniaus universitetas, fiziniai mokslai, fizika – 02P).

1 Introduction

Organic semiconductors based on small molecules or polymers have received tremendous amount of attention from scientific community and business sector over the past few decades due to their unique optoelectronic properties in combination with such appealing features as mechanical flexibility or biocompatibility.[1,2] Today's advanced chemical engineering opened up new pathways to deliberately control the molecular structure of organic compounds[3] and thus their optical and electrical properties[4], which enabled their applications in light emitting diodes[5,6], thin film transistors[1,2,7], solar cells[8], fluorescence sensors (for detection of various external stimuli)[9–12], lasers[13–16] etc. Undoubtfully, the possibility of low cost solution processing or printing on large area substrates simplifies device fabrication and creates a great technological advantage of organic materials as compared to the conventional inorganic semiconductors.[17–22]

Although organic light emitting diodes (OLEDs) based on highly luminescent isolated molecules dispersed in host matrix already found their way into our everyday life through smartphones, TVs, tablets and cameras[22], successful commercialization of fluorescent organic sensors or lasers still requires their technological improvement.[10,13,14,23,24] Strong absorption and intense fluorescence are considered a desirable attribute of such systems, which is ensured by high molecular concentrations.[25] At such conditions in a condensed phase, concentration effects (like fluorescence concentration quenching, molecular aggregation, etc.) caused by intermolecular interactions become of crucial importance.[26,27]

Fluorescent organic nanoparticles (FONs) expressing high surface to volume ratio have drawn considerable attention since the introduction of aggregation induced emission enhancement (AIEE) effect.[28,29] AIEE molecules (siloles[30], cyanostilbenes[31],

tetraphenylethylenes[32], etc.) are known to demonstrate very weak fluorescence in solutions and become highly emissive in the solid state. This holds a great potential for their successful application in fluorescence sensors, where sensing of some external stimulus could be accomplished through the distinct changes in emission in response to morphological modifications.[33–35] To this end, rational tuning of molecular packing in such systems by means of their preparation conditions or rational molecular design appears to be especially important.[36,37]

On the other hand, highly fluorescent organic semiconductors are also considered as an attractive gain medium for solid state laser sources.[13,15] Wide emission wavelength tunability determined by broad gain spectra combined with negligible temperature dependence of amplified spontaneous emission (ASE) threshold, emission wavelength and output power make organic lasers suitable candidates for application in spectroscopy, optical communications, sensing or displays.[15,23,38,39] Although optically pumped organic lasers were already demonstrated, serious technological challenges still remain in realizing electrically driven organic laser.[13] The most important issues were attributed to low charge carrier mobilities, exciton annihilation at high excitation densities, poor stability and polaron absorption leading to insufficient exciton concentrations required to achieve ASE threshold.[13,40]

While the highest charge carrier mobilities were achieved in the neat films (up to 1 $cm^2/V/s$)[41] and single crystals (up to 40 $cm^2/V/s$)[42] of organic semiconductors, the lowest ASE thresholds were demonstrated only in the films doped with low emitter concentrations. Highly concentrated films or single crystals typically suffer from enhanced reabsorption, formation of non-emissive aggregate species and concentration quenching resulting in high ASE thresholds. Thus, it is obvious, that deliberate control of intermolecular interactions through material design and device architecture is required for attaining low ASE

thresholds in condensed gain medium. Combination of low ASE threshold with superior charge carrier transport properties is expected to facilitate realization of electrically pumped organic laser.

1.1 Aim and objectives

The dissertation is aimed at designing new phenylenediacetonitrile- and fluorene-based compounds with high emission efficiency in a solid state (in the form of either nanoparticles, films or single crystals) and suitable for practical applications in fluorescence sensing or lasers. The designed phenylenediacetonitrile compounds for sensing, additionally, are sought to express morphology and emission tuning, fast response and high fluorescence on/off ratio in response to external stimulus, whereas the fluorene compounds for lasing applications are expected to show high radiative decay rate, small reabsorption and excited state absorption and weak fluorescence concentration quenching. The following tasks were set to reach this goal:

1. To investigate the structure-property relationship of phenylenediacetonitrile (PDACN) films and nanoparticles with emphasis on AIEE effect by various spectroscopy and microscopy techniques.
2. To evaluate the potential of PDACN films and nanoparticles for threshold temperature and volatile organic vapour fluorescence sensing applications.
3. To examine the concentration effects on the photophysical and particularly ASE properties of new fluorene- and benzo[c]fluorene-cored oligomers by varying their molecular structure.
4. To determine the impact of intermolecular interactions on the photophysical properties of single crystals grown from differently linked bifluorene derivatives by physical vapour transport.

5. To estimate the contribution of the radiative trap states to ASE in bifluorene single crystals.
6. To achieve low ASE threshold (<1 kW/cm^2) in highly concentrated bifluorene films and single crystals.

1.2 Novelty and relevance

In this work the photophysical properties of novel PDACN derivatives bearing systematically introduced different side-groups are investigated in their different forms (liquid and solid solution, neat films and nanoparticles). It was determined that emission properties can be tuned in a controlled manner by changing film/nanoparticle morphology by varying preparation conditions or altering molecular structure. Performed studies also revealed that isolated PDACN molecules in polystyrene (PS) matrix can form molecular aggregates upon exposure to organic solvent vapour or temperatures above the glass transition of the host matrix, which resulted in distinctly modified emission properties. Demonstrated tunability of fluorescence spectra and intensity via induced changes in morphology encourages technological application of PDACN compounds in threshold temperature or volatile organic vapour fluorescence sensing.

Although organic materials expressing efficient fluorescence and high radiative decay rates have been of interest as a gain medium in lasing applications for a few last decades, no systematic studies of ASE concentration behaviour in such a wide concentration range (0.1 – 100%) were carried out so far. Thorough assessment of concentration effects on ASE properties of new fluorene- and benzo[c]fluorene-cored oligomers allowed to achieve extremely low ASE thresholds at very high compound concentrations and in the neat amorphous films, which are required for future organic laser applications.

New bifluorene derivatives bearing different linking groups were inspected as building materials for highly fluorescent organic single crystals, attractive for electrically pumped laser applications due to potentially high carrier mobilities. Control of intermolecular interactions, achieved by chemical structure design, allowed to demonstrate record low ASE threshold values (700 W/cm^2) in organic single crystals grown by physical vapour transport. Moreover, it was shown that the introduction of radiative trap states into such system significantly lowers ASE threshold.

1.3 Statements of the dissertation

1. Tuning of the morphology and consequently emission properties of PDACN nanoparticles can be achieved by altering the non-conjugated side-groups or nanoparticle preparation conditions.
2. Polymer films with dispersed phenylenediacetonitrile derivatives and phenylenediacetonitrile nanoparticles are suitable for threshold temperature and volatile organic vapour fluorescence sensing applications.
3. 2^{nd} linking position of fluorene sidegroups in benzo[c]fluorene- and fluorene-cored oligomers is superior to 3^{rd} position for achieving high fluorescence quantum yield, high radiative decay rates and low amplified spontaneous emission threshold in dilute polymer films.
4. Incorporation of phenyl or biphenyl central linking groups in bifluorene compounds results in twisted molecular geometry and weaker intermolecular interactions and thus, enhances their single crystal ASE performance as compared to that of planar bifluorene compounds.

5. Crystal doping with emissive traps is suitable for attaining highly fluorescent organic single crystals expressing very low amplified spontaneous emission thresholds (<1 kW/cm^2).

1.4 Publications related to the dissertation

This dissertation is based on the following publications:

1. P. Baronas, G. Kreiza, P. Adomėnas, O. Adomėnienė, K. Kazlauskas, J.-C. Ribierre, C. Adachi and S. Juršėnas, Low-Threshold Light Amplification in Bifluorene Single Crystals: Role of the Trap States, *ACS Applied Materials and Interfaces*, 10, 2768–2775 (2018).
2. G. Kreiza, P. Baronas, E. Radiunas, P. Adomėnas, O. Adomėnienė, K. Kazlauskas, J.-C. Ribierre, C. Adachi and S. Juršėnas, Bifluorene Single Crystals with Extremely Low-Threshold Amplified Spontaneous Emission, *Advanced Optical Materials*, 5, 1600823 (2017).
3. G. Kreiza, K. Kazlauskas, A. Bieliauskas, V. Getautis, A. Šačkus and S. Juršėnas, Fluorescence sensing based on phenylenediacetonitrile doped into polymer host, *Journal of Luminescence*, 170, 293–298 (2016).
4. K. Kazlauskas, G. Kreiza, E. Radiunas, P. Adomėnas, O. Adomėnienė, K. Karpavičius, J. Bucevičius, V. Jankauskas and S. Juršėnas, Concentration effects on spontaneous and amplified emission in benzo[c]fluorenes, *Physical Chemistry Chemical Physics*, 17, 12935–12948 (2015).
5. K. Kazlauskas, G. Kreiza, O. Bobrovas, O. Adomėnienė, P. Adomėnas, V. Jankauskas and S. Juršėnas, Fluorene- and benzofluorene-cored oligomers as low threshold and high gain amplifying media, *Applied Physics Letters*, 107, 43301 (2015).
6. K. Kazlauskas, G. Kreiza, E. Arbačiauskienė, A. Bieliauskas, V. Getautis, A. Šačkus and S. Juršėnas, Morphology and Emission

Tuning in Fluorescent Nanoparticles Based on Phenylenediacetonitrile, *Journal of Physical Chemistry C*, 118, 25261–25271 (2014).

1.5 Other publications

1. P. Baronas, P. Ščajev, V. Čerkasovas, G. Kreiza, P. Adomėnas, O. Adomėnienė, K. Kazlauskas, C. Adachi and S. Juršėnas, Exciton diffusion in bifluorene single crystals studied by light induced transient grating technique, *Applied Physics Letters*, 112, 33302 (2018).
2. A. Ivanauskaitė, R. Lygaitis, S. Raišys, K. Kazlauskas, G. Kreiza, D. Volyniuk, D. Gudeika, S. Juršėnas and J. V. Gražulevičius, Structure–property relationship of blue solid state emissive phenanthroimidazole derivatives, *Physical Chemistry Chemical Physics*, 19, 16737–16748 (2017).
3. T. Serevičius, R. Komskis, P. Adomėnas, O. Adomėnienė, G. Kreiza, V. Jankauskas, K. Kazlauskas, A. Miasojedovas, V. Jankus, A. Monkman and S. Juršėnas, Triplet-Triplet Annihilation in 9,10-Diphenylanthracene Derivatives: The Role of Intersystem Crossing and Exciton Diffusion, *Journal of Physical Chemistry C*, 121, 8515–8524 (2017).
4. O. Opuchovič, G. Kreiza, J. Senvaitienė, K. Kazlauskas, A. Beganskienė and A. Kareiva, Sol-gel synthesis, characterization and application of selected sub-microsized lanthanide (Ce, Pr, Nd, Tb) ferrites, *Dyes and Pigments*, 118, 176–182 (2015).
5. P. Baronas, K. Kazlauskas, G. Kreiza, V. Jankauskas, A. Tomkevičienė, J. Simokaitienė, S. Grigalevičius, J. V. Gražulevičius and S. Juršėnas, Differently linked fluorene-carbazole triads for light amplification, *Dyes and Pigments*, 123, 370–379 (2015).

6. T. Serevičius, P. Adomėnas, O. Adomėnienė, K. Karpavičius, J. Bucevičius, R. Komskis, G. Kreiza, V. Jankauskas, K. Kazlauskas and S. Juršėnas, Impact of non-symmetric 2,9,10-aryl substitution on charge transport and optical properties of anthracene derivatives, *Dyes and Pigments*, 122, 147–159 (2015).
7. P. Data, R. Motyka, M. Lapkowski, J. Suwinski, S. Jursenas, G. Kreiza, A. Miasojedovas and A. P. Monkman, Efficient p-phenylene based OLEDs with mixed interfacial exciplex emission, *Electrochimica Acta*, 182, 524–528 (2015).
8. V. Buinauskaite, V. Martynaitis, S. Mangelinckx, G. Kreiza, N. De Kimpe and A. Šačkus, Facile synthesis of spiro[benzo[e]indole-2,2′-piperidine] derivatives and their transformation to novel fluorescent scaffolds, *Tetrahedron*, 68, 9260–9266 (2012).

1.6 Conference presentations

1. G. Kreiza, P. Baronas, E. Radiunas, P. Adomėnas, C. Adachi, K. Kazlauskas, S. Juršėnas „Low threshold amplified spontaneous emission in organic crystals based on fluorene derivatives“, 42nd Lithuanian National Physics Conference (October 4-6, 2017, Vilnius, Lithuania).
2. P. Baronas, P. Ščajev, V. Čerkasovas, G. Kreiza, P. Adomėnas, K. Kazlauskas, J.C. Ribierre, C. Adachi, S. Juršėnas, “Exciton diffusion in bifluorene single crystals”, 14th European Conference on Molecular Electronics (29 August – 2 September, 2017, Dresden, Germany).
3. S. Juršėnas, G. Kreiza, P. Baronas, E. Radiunas, P. Adomėnas, O. Adomėniene, K. Kazlauskas, J.-C. Ribierre, C. Adachi, “Bifluorene Single Crystals for Lasing Applications”, 12th International Conference on Optical Probes of Organic and Hybrid Semiconductors (19-23 June, 2017, Quebec, Canada).

4. P. Baronas, G. Kreiza, P. Ščajev, V. Čerkasovas, E. Radiūnas, P. Adomėnas, O. Adomėnienė, K. Kazlauskas, J.C. Ribierre, C. Adachi, S. Juršėnas, „Bifluorene Single Crystals For Organic Lasers“, 60th International Conference for Students of Physics and Natural Sciences - Open Readings 2017 (Vilnius, Lithuania, March 14-17, 2016).
5. G. Kreiza, P. Baronas, E. Radiunas, P. Adomenas, C. Adachi, K. Kazlauskas, S. Jursenas “Low Threshold Amplified Spontaneous Emission in Organic Crystals Based on Fluorene Derivatives”, Organic Semiconductors Conference (22-25 September, 2016, Cavtat, Croatia).
6. K. Kazlauskas, G. Kreiza, E. Radiunas, P. Adomėnas, O. Adomėnienė, K. Karpavičius, J. Bucevičius, V. Jankauskas, S. Juršėnas „Light amplification in benzo[c]fluorenes“, Conference Functional Materials and Nanotechnologies (October 5-8, 2015, Vilnius, Lithuania).
7. G. Kreiza, R. Burokas, E. Radiunas, K. Kazlauskas, P. Adomėnas, O. Adomėnienė, O. Bobrovas, V. Jankauskas, S. Juršėnas, „Low-threshold light ampification in highly concentrated films of fluorene-based oligomers“, The 13th European Conference On Molecular Electronics (ECME) (1-5 September, 2015, Strasbourg, France).
8. G. Kreiza, R. Burokas, K. Kazlauskas, P. Adomėnas, O. Adomėnienė, O. Bobrovas, V. Jankauskas, S. Juršėnas, „Mirrorless Lasing In Oligofluorenes“, 41st Lithuanian National Physics Conference, (June 17-19, 2015, Vilnius, Lithuania).
9. K. Kazlauskas, G. Kreiza, E. Radiunas, P. Adomėnas, O. Adomėnienė, K. Karpavičius, J. Bucevičius and S. Juršėnas, „Low-threshold amplified spontaneous emission in benzo(c)fluorenes“, Optics & Photonics international congress 2015 (22-24 April, 2015, Yokohama, Japan).

10. G. Kreiza, E. Radiunas, P. Adomėnas, O. Adomėnienė, K. Kazlauskas, S. Juršėnas, “Emission properties of bifluorene compounds bearing charge transfer character“, 578th WE Heraeus Seminar, „Charge-Transfer Effects in Organic Heterostructures: Fundamentals and Applications“ (December 9-12, 2014, Bad Honnef, Germany).
11. K. Kazlauskas, G. Kreiza, E. Arbačiauskienė, A. Bieliauskas, V. Getautis, A. Šačkus, S. Juršėnas, „Emission and morphology tuning in divinylbenzene-based fluorescent nanoparticles“, The international and interdisciplinary conference “Nanotechnology: Research and Developement“ (15-16 May, 2014, Vilnius, Lithuania).
12. S. Raišys, G. Kreiza, S. Grigalevičius, K. Kazlauskas, S. Juršėnas, „Bifluorene derivatives for fluorescent organic nanoaggregates“, 7th International conference on Molecular Electronics (August 24-29, 2014, Strasbourg, France).
13. G. Kreiza, S. Raišys, E. Radiunas, S. Grigalevičius, K. Kazlauskas, S. Juršėnas, “Fluorescence properties of diphenylfluorene derivatives and their nanoparticles“, 7th International Symposium on Flexible Organic Electronics (ISFOE14) (July 7-10, 2014, Thessaloniki, Greece).
14. G. Kreiza, E. Radiunas, K. Kazlauskas, S. Grigalevičius, and S. Juršėnas, „Aggregation-induced emission enhancement in bifluorene derivatives“, XV International Krutyn Summer School, Challenges to open up the new era of organic photonics and electronics from material to market - from Asian perspective“ (June 8-14, 2014, Krutyn, Masurian Lake District, Poland).
15. K. Kazlauskas, G. Kreiza, E. Arbačiauskiene, A. Bieliauskas, A. Šačkus, S. Juršėnas, “Shape and morphology tuning of p-phenylenediacetonitrile-based fluorescent nanoparticles“, SPIE 2013 Optics+Photonics, Organic Photonics and Electronics (San Diego, California, USA, August 25-29, 2013).

16. K. Kazlauskas, G. Kreiza, A. Gruodis, S. Šakirzanovas, A. Miasojedovas, S. Juršėnas, "Tuning of the optical and morphological properties of p-divinylbenzene-based fluorescent nanoparticles", The 10th international conference on Optical Probes of Conjugated Polymers and Organic Nanostructures (Durham, United Kingdom, July 14-19, 2013).
17. K. Kazlauskas, G. Kreiza, E. Arbačiauskienė, A. Bieliauskas, A. Šačkus, S. Juršėnas, „p-Divinylbenzene-based fluorescent nanoparticles of controlled shape and morphology", 11th International symposium on functional pi-electron systems (Arcachon, Aquitaine, France, June 2-7, 2013).
18. G. Kreiza, K. Kazlauskas, A. Miasojedovas, E. Arbačiauskienė, A. Bieliauskas, A. Šačkus, S. Juršėnas, „Self-assembly of fluorescent nanoaggregates based on 1,4-divinylbenzene derivatives", 56th Scientific Conference for Young Students of Physics and Natural Sciences - Open Readings 2013 (Vilnius, Lithuania, March 20-23, 2013).

1.7 Participation in scientific projects

1. May 2013 – June 2015. "Flexible structure bearing bifluorene compounds for optoelectronics industry, BiFluorenas", (EU structural funds, 2013-2015).
2. June 2013 – July 2015. "Control of the photophysical properties of multifunctional molecular systems", (Global Grant, The Research Council of Lithuania, 2012-2015).
3. October 2015 – September 2017. "Towards Organic Laser Transistor" (Joint Lithuania-Japan research project, The Research Council of Lithuania, 2015-2017).

4. October 2017– present. “Enhancing light upconversion efficiency in organic films for optoelectronic applications” (The Research Council of Lithuania, 2017-2020).
5. January 2018 – present. “Triplet state engineering in organic optoelectronic compounds” (Global Grant, The Research Council of Lithuania, 2017-2022).
6. January 2018 – present. “Development of advanced optoelectronic materials using smart molecular engineering.” (EU structural funds, 2017-2022).

1.8 Author’s contribution

The author performed all experiments and calculations presented in this dissertation, including sample preparation, their spectroscopic and microscopic investigation, determination of ASE properties as well as quantum chemical calculations. The author actively participated in the discussions of results as well as preparation of the publications.

Synthesis of new phenylenediacetonitrile compounds was carried out in the research groups led by prof. Vytautas Getautis and prof. Algirdas Šačkus (Kaunas University of Technology). Whereas new fluorene and benzofluorene compounds were synthesized in the group of dr. Povilas Adomėnas (Vilnius University). Dr. Simas Šakirzanovas carried out SEM measurements of phenylenediacetonitrile nanoparticles. Paulius Baronas performed excited state absorption measurements of bifluorene single crystals. Dr. Vygintas Jankauskas realized charge carrier mobility measurements of fluorene and benzofluorene neat films. Regimantas Komskis assisted with differential scanning calorimetry experiments. The author kindly acknowledges the colleagues for their contribution.

1.9 Layout of the dissertation

In Chapter 1 the introduction of the dissertation is presented, in which the importance of concentration effects and high fluorescence efficiency in organic solids are pointed out. This is followed by the aim and objectives of the dissertation, novelty and relevance, statements of the dissertation, list of publications related to the dissertation, other publications, list of presentations in the conferences, participation in scientific projects and author's contribution to the dissertation.

Chapter 2 consists of an overview of efficient solid state fluorescence in organics solid materials utilized for sensing and lasing applications. Aggregation induced emission enhancement phenomenon and its technological applications are presented. Light amplifying organic solids and the main issues are overviewed.

In Chapter 3 preparation of samples and the main experimental and theoretical methods are described. This includes steady state absorption and fluorescence measurements, evaluation of fluorescence quantum yield, measurements of fluorescence transients, various microscopic techniques as well as quantum chemical calculations.

In Chapter 4 experimental results and discussion with three main sections are presented. Section 1. presents the morphology and emission tuning in phenylenediacetnitrile nanoparticles and films for their application in fluorescence sensing. Molecular structures and their optimized geometries of new phenylenediacetonitrile compounds are introduced. Further, concentration quenching bahaviour and aggregation induced emission enhancement effect is discussed. This is followed by spectroscopy measurement data and excited state dynamics in phenylenediacetonitrile nanoparticles. Finally, vapour and threshold temperature sensing is demonstrated. Section 2. presents highly concentrated fluorene and benzo[c]fluorene films for low threshold light

amplification. Molecular structures and their thermal and optical properties are introduced. It is followed by excited state dynamics and fluorescence concentration quenching analysis. Thereafter, amplified spontaneous emission properties, photostability and carrier drift mobilities are studied and the impact of fluorene sidegroup linking topology is evaluated. Section 3. starts with presentation of compounds used to grow single crystals investigated in this work. Quantum chemical simulations and thermal properties are described. It is followed by absorption and emission properties and light amplification study of bifluorene compounds and their crystals. A short summary finalizes each section.

In Chapter 5 conclusions of the dissertation are formulated.

2 Efficient solid state fluorescence for sensing and lasing applications

2.1 AIEE phenomenon and technological applications

Fluorescence quantum yield and intensity are one of the key factors in developing new organic materials for light emitting devices.[43–45] Typically, highly fluorescent hydrocarbon compounds possess rigid and planar molecular structures ensuring excellent π-conjugation and efficient emission in isolated form.[46] A few examples of such highly emissive compounds are given in Fig. 2.1.[47–52] Unfortunately, conventional efficient emitters based on planar molecular geometry tend to form aggregates with strong intermolecular π-π interaction in a condensed phase (usually in neat films or single crystals). Small-molecule organic semiconductors typically form either H- or J-type aggregates in the solid state.[53] The aggregation type is determined by the alignment of the transition dipole moments of the neighbouring molecules. In the case of H-aggregates molecules stack in a face-to-face arrangement, whereas in J-type aggregates head-to-tail intermolecular packing dominates.[54] The formation of such aggregate species can modify the energies of the excited states, and correspondingly, the oscillator strengths of transitions involved, what makes significant impact on the optical properties, such as photoluminescence spectra, optical absorption, fluorescence quantum yield, lifetime etc.[53] Formation of J-aggregates results in a red-shifted optical transition featuring higher oscillator strength and increased fluorescence intensity as compared to those of isolated molecules.[55] H-type stacking is generally associated with strongly reduced oscillator strengths, blue-shifted absorption/fluorescence spectra and dramatically reduced fluorescence quantum yields.[56] This must be taken into account

since the solid phase is highly desirable for practical applications, such as OLEDs, lasers, fluorescence sensors or organic field effect transistors

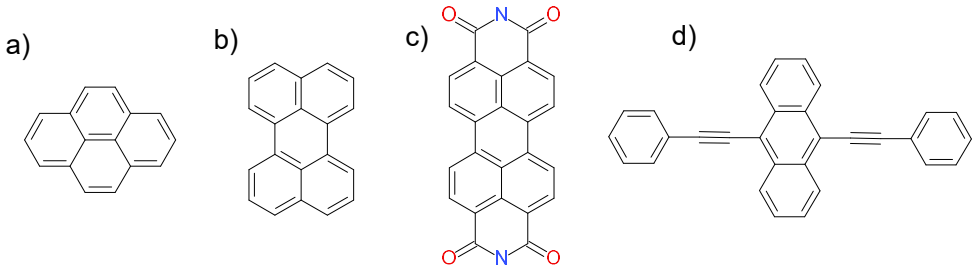

Fig. 2.1 Examples of typical planar chromophores exhibiting high fluorescence efficiency in isolated state: a) pyrene; b) perylene; c) perylene-diimide; d) 9,10-bis(phenylethynyl)anthracene.

(OFETs).[27,57,58] Aggregation can be extremely detrimental to device performance due to often occurring fluorescence concentration quenching phenomenon associated with Förster resonance energy transfer (FRET) to non-emissive molecular aggregates or excimers formed in highly concentrated medium.[59,60]

A number of successful attempts was made to prevent the aggregation and face-to-face packing of emitter molecules. These include decoration of molecular structure with long non-conjugated -alkyl groups, introduction of bulky cyclic units or polar moieties as well as dispersion of target compound in inert polymer hosts.[61–65] Alas, such approaches often result in complicated chemical synthesis, complex molecular structure or reduced device performance due to low charge carrier mobility.[25]

One of the most successful strategies to achieve high fluorescence efficiency in a solid state was proved to be the implementation of compounds exhibiting aggregation induced emission enhancement (AIEE). This is an attractive material property, which is defined by the structure of molecules forming aggregates. It has been aimed at by many research groups in order to investigate and even apply AIEE in their own materials or devices.[25,35] The enhancement of

fluorescence intensity caused by environment rigidification or molecule aggregation was already reported and explained for oligophenylenevinylene based compounds in 1996.[36,66] However, the thorough theory of AIEE phenomenon was developed and widely promoted only from 2001 by investigating siloles and cyano-stilbenes.[28,67] The realization of compounds with enhanced emission in the solid state through AIEE property created entirely new possibilities for their implementation in such applications as OLEDs[68–70], OFETs[71,72], organic lasers[73,74], fluorescence sensors (for detection of explosives, ions, pH, temperature, viscosity, pressure)[30,75], biological probes[32,76,77], chemical sensors[78,79] etc.

Different intramolecular and intermolecular mechanisms or a combination of them, both defined by unique electronic and geometrical properties, have been proposed to explain the AIEE phenomenon demonstrated by various types of compounds. Intramolecular mechanisms associated with molecular structure confinement were reported to enhance the fluorescence in a solid state. This covers restriction of intramolecular torsion, rotation or vibration[80–83], geometry planarization[28,84] or hindered intramolecular charge transfer[85]. Furthermore, intermolecular mechanisms like formation of specific supramolecular stacking architectures (such as J-aggregates)[86,87] or inhibited face-to-face packing by molecular geometry[88] were proved to significantly enhance fluorescence efficiency in the aggregated phase.

To this day, the mostly investigated compounds claimed to express AIEE behaviour are phenylsiloles[32,89], distyrylbenzenes[90,91], tetraphenylethenes[92–94], triphenylethylenes[72,95,96], dibenzofulvenes[97] and cyano-vinylenes[98,99] (Fig. 2.2). Cyano-vinylene based compounds have received considerable attention due to their unique intramolecular feature – twist elasticity enabled by steric cyano groups, and also capability of

secondary intermolecular bonding interactions. Such properties allow realization of various molecular packing and multiple solid state

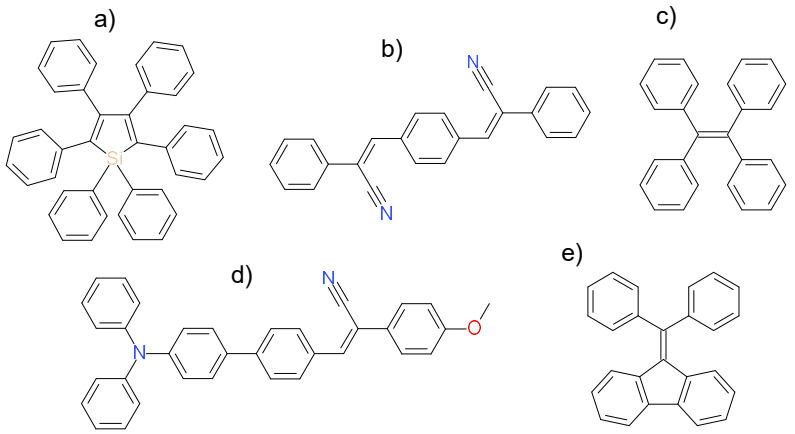

Fig. 2.2. Examples of compounds exhibiting AIEE properties. a) hexaphenylsilole; b) cyanostilbene; c) tetraphenylethylene; d) triphenylamine-cyanovinylene compound; e) dibenzofulvene.

morphologies.[33,100] Since the photophysical properties of functional layers in the molecule-based devices are strongly influenced by the layer morphology, the possibility of easy morphology tuning is essential. Fluorescence switching enabled by the morphology tuning for AIEE compounds based on diphenyldibenzofulvenes[33,100], cyanodistyryl-benzenes[31,101,102], phosphaphen-anthrene[103], arylamines[104,105] and others was demonstrated using thermal, mechanical and volatile organic vapour stimuli. Development of new stimuli-responsive materials with tunable morphology and high fluorescence signal contrast was recognized to be important for a variety of practical applications such as optical memories, functional fluorescence sensors, optical displays, etc.[30,104,106–110]

2.2 Light amplification in organic solids

Laser sources based on low-cost highly fluorescent organic materials have received a lot of attention due to their attractive electronic and optical properties, mechanical flexibility and easy device fabrication

process.[15,23] Possibility of simple optoelectronic device fabrication by means of solution processing (e.g. printing or spray-coating) is considered as one of the key advantages of organic semiconductors.[5,111] Even evaporation of amorphous organic layers in high vacuum is less challenging than epitaxial growth of inorganic crystals.[16] Moreover, lasers based on organic semiconductors can be potentially compact and ready for integration with other optoelectronic devices since amorphous films can be deposited on a variety of substrates.[23] Broad gain spectra and wide choice of organic materials enable widely tunable emission wavelength covering the entire visible range. Negligible temperature dependence of ASE threshold, output power and wavelength, which is a result of the molecular origin of the electronic transitions, (i.e. strongly localized excited states - excitons), make organic lasers advantageous over conventional semiconductors.[16,112] Because of these properties, organic lasers are considered well suitable for implementations in such applications as spectroscopy, optical data communications, memory, sensing and displays.[16,113]

Breakthroughs in material and device design allowed to attain lasing thresholds as low as few watts per square centimetre in the optically-pumped distributed feedback (DFB) polymer lasers.[114] In spite of that, great challenges in realizing electrically driven organic lasers still are to overcome.[15,23] The main issues are related to reabsorption losses, insufficient charge carrier mobility, polaron absorption, quenching by electrodes and poor photostability of organic materials.[15,16,23,39,112,115] The poor photostability shortens the lifetimes of organic lasers and thus, makes them unsuitable for practical applications.[23] This can also be associated with insufficiently low ASE thresholds. It causes the usage of high excitation densities and thereby accelerates degradation of organic compounds. In addition, it is essential to minimize reabsorption for obtaining high optical gain, since low losses at the ASE wavelength lead to

reduced excitation densities required for population inversion. Organic compounds possessing twisted molecular geometry are highly beneficial, due to the presence of considerable Stokes shift, which enables emission wavelength in a spectral region wherein reabsorption losses are significantly smaller.[39] Förster resonance energy transfer (FRET) mechanism can be utilized for a larger energetic separation of absorption and emission spectra by using guest–host systems.[116] However, the redshifted fluorescence can be more efficiently quenched by polaron absorption.

Low charge carrier mobility prevents sufficiently high current densities required for achieving threshold exciton concentrations. Insufficient mobility also leads to a high concentration of polarons especially near the contacts. This causes charge quenching (due to polaron absorption) and quenching from the electrodes.[16] Additionally, singlet exciton annihilation at high exciton concentrations is identified as another crucial loss mechanism in organic lasers.[23,117] Both of these loss mechanisms are conditioned by intermolecular interactions, which are known to be influenced by the solid film packing morphology and by their preparation conditions.[39] On top of that, at high emitter concentrations or in the neat films, intermolecular interactions are significantly enhanced. Since this can lead to the formation of poorly emissive aggregate or excimer species[118], a most obvious way to preserve highly efficient emission and low ASE threshold is to minimize intermolecular coupling through increased intermolecular separation. Different approaches were made to hinder intermolecular interactions in organic laser gain medium. This includes introducing chromophore molecules into host material, exploiting bulky molecular side groups or using spiro- compounds.[16] However, high exciton densities and high charge carrier mobilities are required for realization of directly electrically driven organic laser. Alas, these features and reduced intermolecular coupling are often seen as

incompatible with each other. This suggests that a certain trade-off exists regarding the properties of organic laser compounds and also points out the significance of developing new materials exhibiting not only extremely low ASE threshold, but also weak fluorescence concentration quenching and high carrier mobility.

To that end, highly fluorescent organic single crystals are highly promising as a gain medium in electrically driven organic lasers.[13,40] Due to the ordered molecule alignment in high-quality single crystals and high ambipolar charge carrier mobilities leading to current densities up to several kA/cm^2, high exciton concentrations required for population inversion can be achieved.[117,119] Favourable molecular dipole orientation and the absence of light scattering centres facilitate light out-coupling and holds a great promise to minimize lasing threshold.[120,121]

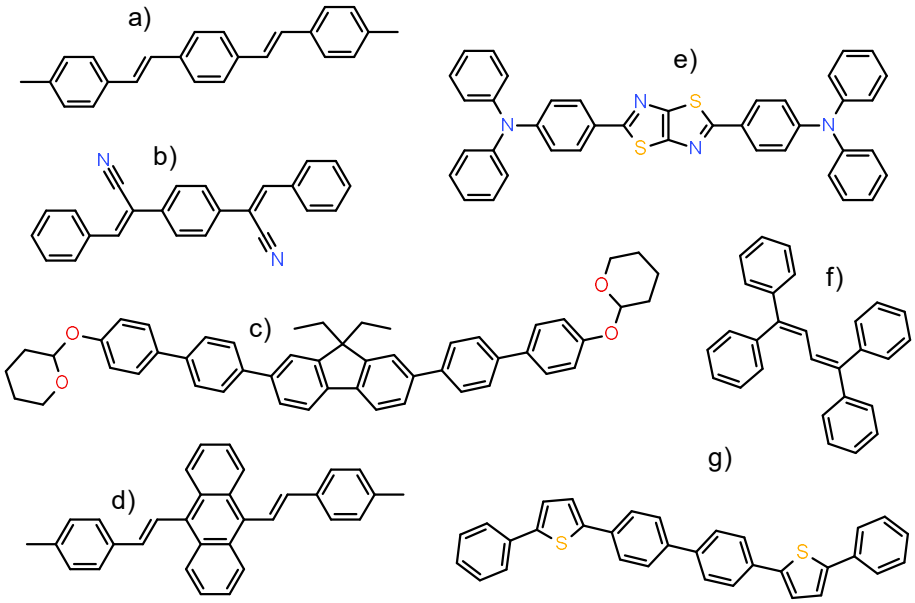

Fig. 2.3 Chemical structures of compounds used to grow single crystals demonstrating ASE activity. (a) 1,4-bis(4-methylstyryl)benzene; (b) dicyanodistyrylbenzene; (c) fluorene/phenylene derivative; (d) 9,10-distyrylanthracene; (e) 4,4′-(thiazolo[5,4-d]-thiazole-2,5-diyl)bis(N ,N-diphenylaniline); (f) 1,1,4,4-tetraphenyl-1,3-butadiene; (g) thiophene-/phenylene cooligomer.

A number of organic materials was already developed and employed as building blocks for single crystals demonstrating high emission efficiency and ASE activity: 1,4-bis(4-methylstyryl)benzene[122], dicyanodistyryl-benzenes[100,123], thiophene-/phenylene cooligomers[120], 9,10-distyryl-anthracene[124], 1,1,4,4-tetraphenyl-1,3-butadiene[125], 4,4′-(thiazolo[5,4-d]-thiazole-2,5-diyl)bis(N ,N-diphenylaniline)[126], fluorene/phenylene cooli-gomers[127] etc. (see Fig. 2.3 for molecular structures). However, the lowest ASE thresholds achieved in single crystals are still few times higher than those demonstrated in the amorphous neat or doped films.[128–131]

The photophysical properties of organic crystals mainly are governed by intermolecular coupling, which can be deliberately controlled via molecular packing – intermolecular distances, orientation and inclination. It was demonstrated that strong excitonic coupling (as in J- and H-type aggregates) might lead to poor ASE properties. The J-type coupling exhibits considerably enhanced reabsorption losses and H-type coupling results in low radiative decay rates. This implies that the lowest ASE thresholds could be achieved in organic crystals demonstrating weak excitonic coupling. This task can be accomplished by introducing spacers in molecular structure or by designing molecules with slipped arrangement in crystalline state.[13] Weak intermolecular coupling in crystals also reduces exciton diffusion which results in minimized exciton annihilation at high pump intensities required to achieve ASE. One of the most critical factors limiting ASE performance is considered to be induced absorption to higher singlet, triplet, or polaron states. Thus materials with virtually no ground or excited state absorption overlap in the gain region are in demand.[132,133] To overcome absorption losses, doping strategy has been successfully implemented not only in thin films but also in single crystals, which have been investigated for lasing applications. However, ASE threshold values are still above the lowest values recorded for undoped crystals.[134]

3 Methods

3.1 Sample preparation

Solutions of PDACN and fluorene compounds were prepared in spectroscopic grade tetrahydrofuran (THF) solvent with a concentration of 10^{-5} M to evaluate the photophysical properties of isolated molecules.

Neat films of the investigated organic semiconductors were prepared by drop-casting or spin-coating concentrated solutions (10^{-2}-10^{-3} M) of spectroscopic grade THF or toluene on pre-cleaned glass substrates. The substrates were cleaned with Hellmanex solution, acetone, isopropyl alcohol, distilled water and placed in UV-Ozone cleaner. The concentration of solution, solvent type and spin-coating speed were intentionally adjusted depending on compound solubility and on desirable film thickness and roughness.

Polymer films doped with a wide concentration range (0.1 – 100 wt %) of the investigated compounds were used for concentration quenching analysis. These films were prepared by dissolving PDACN or fluorene compounds and polystyrene (PS) in toluene at the appropriate ratio and spin-coating or drop-casting the solutions (70 mg/mL) on pre-cleaned and UV-ozone treated glass substrates.

ASE measurements were performed only on spin-coated films (~1 μm thickness) with a freshly cleaved edge.

Nanoparticles based on PDACN compounds were formed by a simple reprecipitation method. In this method the target compound is dissolved in a good solvent and the solution is mixed with a bad solvent under vigorous stirring. This leads to fast nucleation of a target material and, thus, formation of nano/microparticles in a mixture of good and bad solvent. Schematic representation of organic nanoparticle formation by reprecipitation method is given in Fig. 3.1. In this work spectroscopic

grade THF was used as a good solvent and deionized water was chosen as bad solvent for PDACN compounds. According to the procedure appropriate amount of deionized water was rapidly (<1 s) injected into the THF solutions of the studied compounds. The final concentration of PDACN in THF/H_2O mixture was kept constant at 10^{-5} M. The volume of the prepared mixtures was 2.5 mL, i.e. sufficient for spectroscopic measurements in quartz cuvettes. The water volume fraction in the mixtures was varied from 0% to 98% to reveal the influence on nanoparticle morphology and their properties.

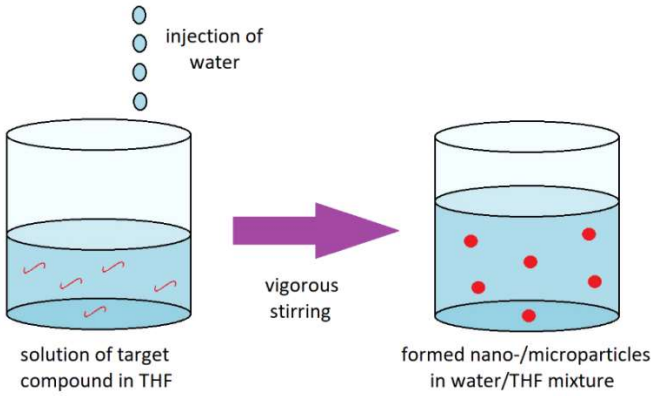

Fig. 3.1. Schematic representation of reprecipitation method used to form organic nanoparticles.

Single crystals based on fluorene compounds were grown by physical vapour transport technique (See Fig. 3.2.). Horizontal tube-based sublimation system DSU-20 (CreaPhys) with 3-zone heating furnace, gas flow and pressure control was employed for this task. Starting materials in powder form were heated up to temperatures 10 - 30 K below their melting points to achieve evaporation without melting of the initial powder. Crystal growth temperature was set to be similar to material crystallization temperature obtained by means of differential scanning calorimetry (DSC). Pure nitrogen was used as a carrier gas with a gas flow of 10 mL/min. Sublimation chamber pressure was varied from 0.1 to 1 bar by utilizing vacuum pump system. Crystal growth process usually took

from 12 to 24 hours, after which thin (up to 10 μm) plate-like single crystals with lateral dimensions up to 1 cm were obtained. Crystals were placed on pre-cleaned glass substrates for spectroscopic and microscopic analysis.

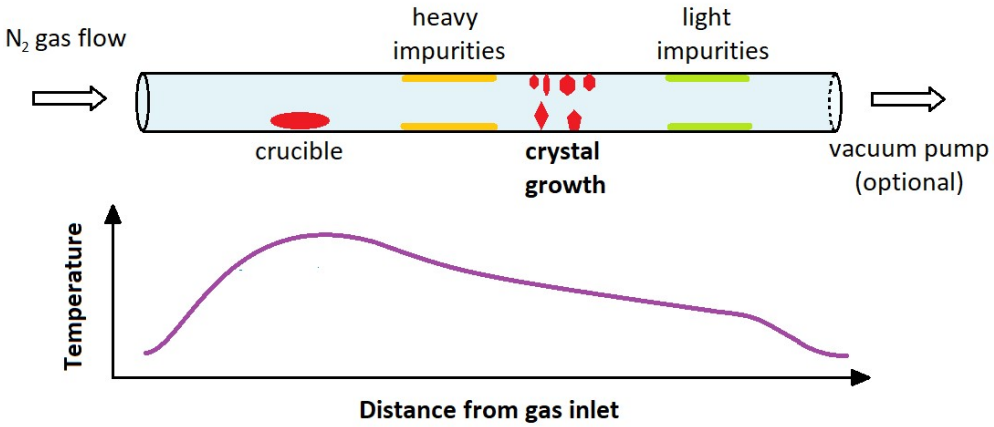

Fig. 3.2. Organic single crystal growth by physical vapour transport.

3.2 Spectroscopic and microscopic characterization

Absorption spectra of the investigated dilute solutions, THF/H_2O mixtures, PS films, neat films and single crystals were obtained by using UV-vis-NIR spectrophotometer Lambda 950 (Perkin-Elmer) equipped with an integrating sphere for highly light-scattering samples.

Steady state fluorescence spectra of the investigated samples were recorded on a back-thinned charge coupled device (CCD) spectrometer PMA-11 (Hamamatsu). 365 nm light emitting diode (Nichia) or xenon arc lamp coupled to a monochromator were used as an excitation source. Excitation wavelength was chosen to be as near as possible to absorption maxima of samples while avoiding the interference to fluorescence signal.

Fluorescence quantum yield (Φ_F, relative error – 5%) of dilute solutions, films, nanoparticle suspensions and single crystals was determined by utilizing integrating sphere (SphereOptics).[135]

Fluorescence transients of inspected samples were measured by using a time-correlated single photon counting system PicoHarp 300 (PicoQuant). Pulsed semiconductor laser diode (PicoQuant, repetition rate – 1 MHz, pulse duration – 70 ps, emission wavelength – 375 nm) or pulsed light emitting diode (PicoQuant, repetition rate – 1 MHz, pulse duration – 500 ps, emission wavelength – 330 nm) were utilized as an excitation source. Fluorescence signal was collected at the maxima of fluorescence spectra by using a monochromator.

Fluorescence microscopy and polarized light microscopy (POM) images of the neat films, polystyrene blends, microparticles and single crystals were captured on optical fluorescence microscope (Olympus BX51) equipped with an UV excitation source.

Scanning electron microscopy (SEM) images of formed nanoparticles were obtained at 2 kV acceleration voltage by using SU70 (Hitachi) SEM. Nanoparticle films for SEM analysis were prepared by drop-casting from THF/H_2O mixtures on pre-cleaned heavily doped crystalline silicone substrates. The films were coated with 5 nm thick chromium layer by using magnetron sputtering to enhance image quality. SU8230 (Hitachi) SEM equipped with cold field emission electron gun was utilized for microscopic investigation of fluorene-based single crystals.

Atomic force microscopy (AFM) measurements were performed with Dimension Icon (Bruker) AFM by using tapping mode.

Hydrodynamic radius of investigated nanoparticles was evaluated by employing Zetasizer Nano (Malvern) dynamic light scattering (DLS) measurement system.

Differential scanning calorimetry measurements were carried out by using DSC 1 (Mettler Toledo) instrument under continuous nitrogen gas flow. Heating and cooling rates were set to 10 K/min.

ASE measurements of investigated thin films and single crystals were carried out by using thin excitation stripe geometry (See Fig. 3.3.).

Laser stripe (width – 40-50 μm, length – 5 mm) was focused on the sample surface near the edge by using a cylindrical lens. Emission propagating along the stripe was recorded on a CCD spectrophotometer PMA-11 (Hamamatsu). Wavelength tunable optical parametric amplifier pumped by nanosecond Nd:YAG laser (repetition rate 10 Hz, pulse duration 5 ns) was utilized to excite the samples at their absorption maxima. The optical gain coefficients in the investigated samples were estimated by using variable stripe length method.[136] Excitation stripe length was increased from 0 to 2 mm by mechanical shutter during this measurement.

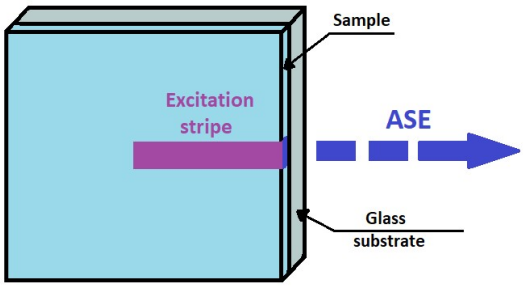

Fig. 3.3. Schematic representation of ASE measurement by using thin excitation stripe technique.

3.3 Quantum chemical calculations

All quantum chemical calculations were carried out by using Gaussian 09W software package.[137] Molecular geometry pre-optimization was performed by utilizing semiempirical PM6 method. Final ground state geometry optimization in vacuum was accomplished by means of density functional theory (DFT) calculations with B3LYP/6-31G(d) basis set.

Optimized ground state geometry was used to calculate vertical absorption energies and oscillator strengths for electronic transitions from singlet ground state (S_0) to higher singlet (S_n) or triplet (T_n) excited states and to obtain charge distribution in highest occupied (HOMO) and lowest unoccupied (LUMO) molecular orbitals. Time-dependent density functional theory (TD-DFT) with B3LYP/6-31G(d) basis set was employed for these calculations.

4 Experimental results and discussion

4.1 Morphology and emission tuning in phenylenediacetonitrile nanoparticles and films for sensing applications

Aiming for AIEE compounds with easy morphology tuning and highly efficient fluorescence in a solid state, the series of PDACN molecules functionalized with pyrazole moieties and various alkoxy or cyclic side groups were synthesized and investigated (Fig. 4.1). The cyano-vinylene bridges were intentionally introduced into the backbone to provide the twist elasticity along with the AIEE property induced by the sterically demanding cyano groups.[90,138]

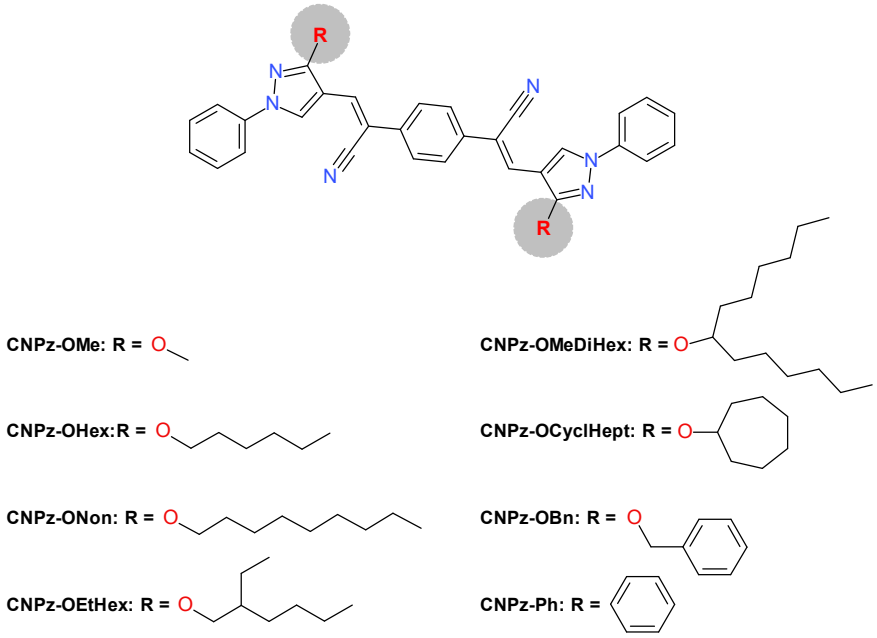

Fig. 4.1. Chemical structures of investigated phenylenediacotonitrile compounds.

The choice of pyrazole moieties was based on their ability to deliver high fluorescence efficiency as well as to cause strong intermolecular hydrogen bondings and π-π interactions important for construction of functional supramolecular structures.[106,139] The length and the branching degree of alkoxy side chains linked to the pyrazole moiety was chosen to vary for

elucidation of the optimal configuration, which in turn could enable simple morphology tuning. The studied compounds were checked for the presence of AIEE behaviour by measuring fluorescence efficiency of the compounds dispersed in polymer host as a function of their concentration. PDACN nanoparticles formed by precipitation in the solvent/non-solvent mixture were probed spectroscopically as well as utilizing fluorescence lifetime and quantum yield evaluation methods, which in combination with electron and polarized optical microscopy allowed discrimination of the different aggregate morphologies. Remarkably, some of the compounds bearing alkoxy side groups were found to yield different packing morphologies in the nanoparticles, which could be easily tuned (between crystalline and amorphous) invoking also emission tuning by simply altering solvent/non-solvent ratio in the mixture.

4.1.1 Molecule geometries determining low emission in solution

Equilibrium ground state geometries of the backbones of all the studied PDACNs optimized by quantum chemical calculations were found to be identical irrespectively of the side groups attached. Correspondingly, calculated HOMO and LUMO in all the compounds were found to be unperturbed by the side groups and localized solely on the backbone. Examples of HOMO and LUMO for a few representative compounds CNPz-OMe, CNPz-OMeDiHex and CNPz-OCyclHept are shown in Figure 4.2. The optimized geometry of the selected PDACN derivative CNPz-OMe as a typical example is illustrated in Figure 4.3a. For the reference, the geometry of analogous compound without cyano groups in the backbone is shown in Figure 4.3b. While the backbone of cyano-free compound is planar within the extent of pyrazole moieties, the backbone of dicyano-substituted counterpart is distorted at the vinylene linkages. The distortion of CNPz-OMe backbone at these linkages is somewhat smaller

(dihedral angles 19° and 3°) with respect to similar dicyano-substituted distyrylbenzene backbone (dihedral angles 29° and 8°)[90] as a result of less

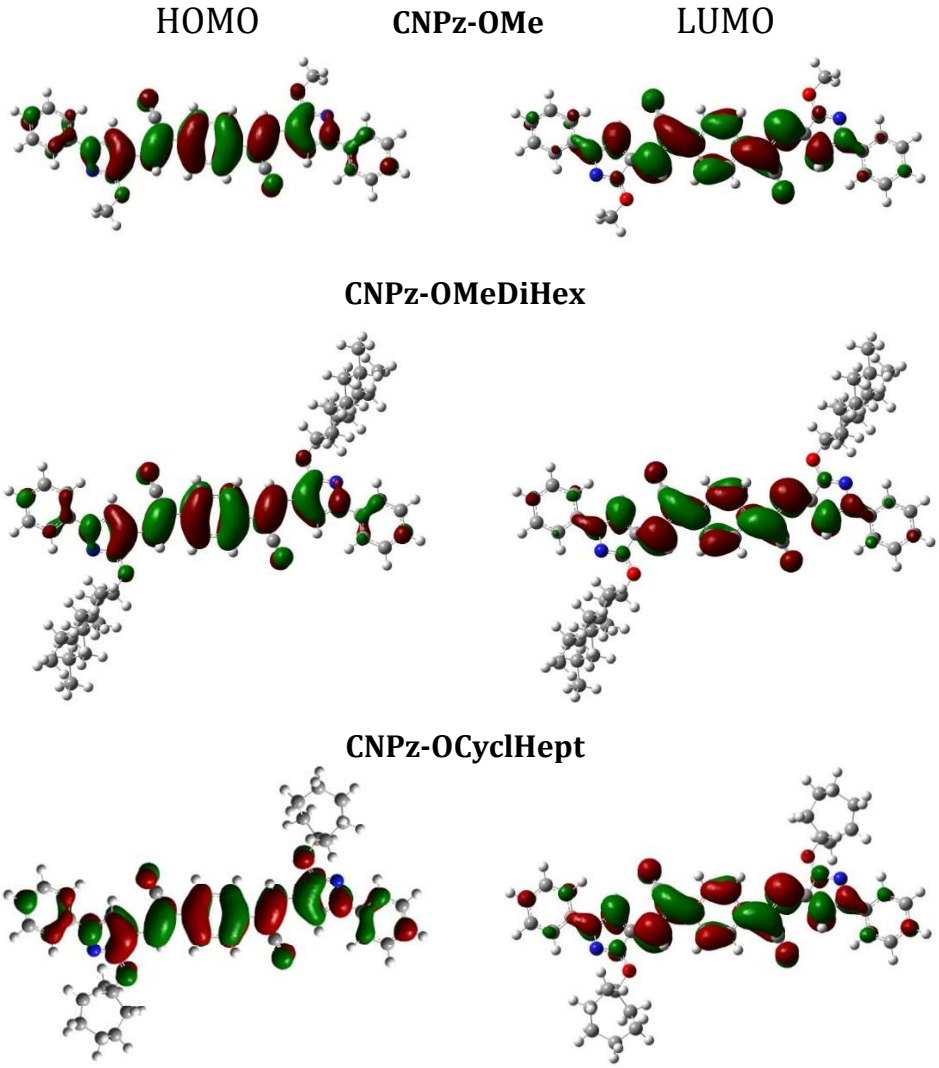

Fig. 4.2. HOMO and LUMO of geometrically optimized PDACN compounds CNPz-OMe, CNPz-OMeDiHex and CNPz-OCyclHept calculated at the B3LYP/6-31G* level.

bulky, and thus, less sterically hindered pyrazole moieties. Nevertheless, such distortion as well as additional one induced by the phenyl end-groups forming 18° angle with the pyrazole moieties (see Figure 4.3a) suffices to promote efficient intramolecular torsions/vibrations alike to those reported for other cyano-vinylene compounds.[36,85,138] The outcome is an extremely fast non-radiative deactivation of the excited state

associated with torsional/vibrational motions of the molecular fragments resulting in a very faint emission of the compounds in dilute solutions.[80,140]

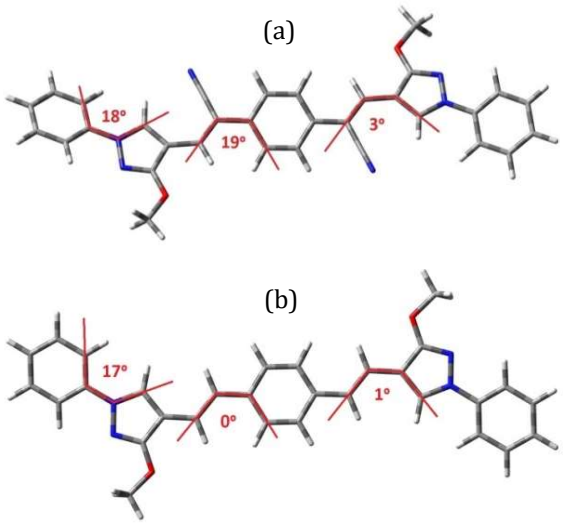

Fig. 4.3. Optimized geometries of the PDACN derivative CNPz-OMe (a) and the analogous compound w/o cyano groups (b), as calculated by DFT in the gas phase. Dihedral angles between neighbouring fragments are indicated.

Indeed, the Φ_F of PDACN compounds in solution is very low and ranges from 0.3% to 0.7% (Figure 4.4). For alkoxy or cyclic side groups bridged to the pyrazole moieties via oxygen, Φ_F falls within 0.5 – 0.7% or is even half as that (0.3%) for CNPz-Ph. Exceptionally low Φ_F of CNPz-Ph may be caused by the additional phenyl side-rotors directly linked to the backbone via short methyl bridges. Meanwhile somewhat longer alkoxy bridges in the rest compounds induce smaller steric repulsion, and thus less effectively couple vibronic relaxation. Partial suppression of the intramolecular torsions, which can be achieved, for example, by anchoring additional phenyl[141] or much heavier carbazolyl[142] moieties to the labile phenyl end-groups of the phenylenediacetonitrile backbone immediately boosts Φ_F up to 1% or 3%, respectively (see Figure 4.4).

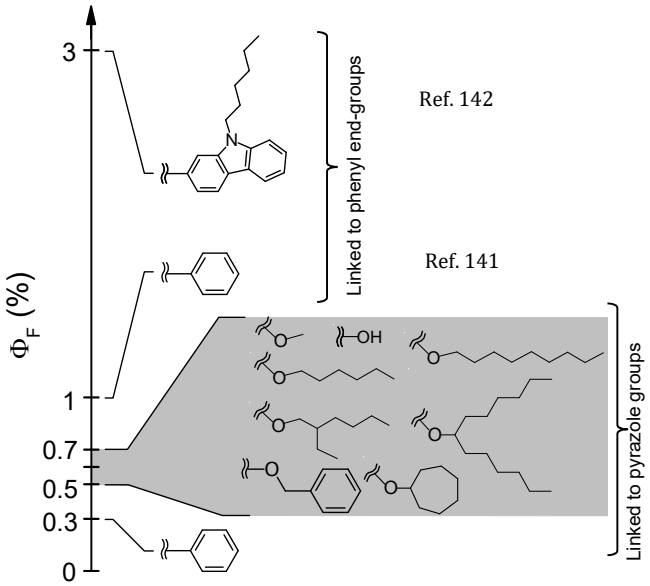

Fig. 4.4. Fluorescence quantum yield of the PDACN derivatives in 10^{-5} M THF solution as a function of different side groups (indicated). Data on phenyl and carbazolyl moieties linked to phenyl end-groups of the studied compounds are shown for reference.

4.1.2 Concentration quenching *vs* AIEE

The presence of AIEE property in the PDACNs was examined by evaluating Φ_F of the compounds dispersed in polystyrene host as a function of their concentration (Figure 4.5). The evaluation also permitted unambiguous discrimination of the intra- and inter-molecular effects determining Φ_F at low and high compound concentration, respectively. Typically, most fluorophores exhibit fluorescence quenching with increasing concentration.[59,60,143] This is a result of enhanced excitonic coupling in aggregates significantly reducing radiative decay rate as compared to the rate of competing nonradiative processes, *e.g.*, exciton migration-assisted trapping at the quenching sites (impurities, defects or other imperfections), intersystem crossing to triplet states, etc.[144] Concentration quenching was observed in PDACN compound CNPz-OCyclHept bearing cycloheptyl side-groups, for which Φ_F was quenched from 20% at low concentrations down to 2% in the neat film (see

Figure 4.5a). Meanwhile, the rest compounds expressed pronounced AIEE effect for the concentrations roughly above 2% by weight in PS.

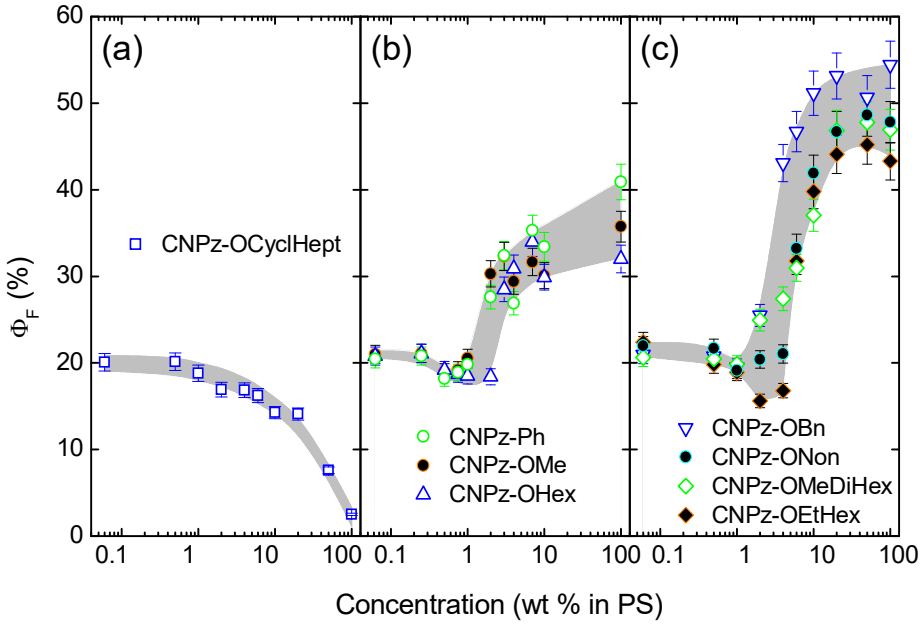

Fig. 4.5. Fluorescence quantum yield of the PDACN derivatives as a function of their concentration in PS host.

At the lowest compound concentrations in PS host (<1 wt %) all the PDACN derivatives exhibited $\Phi_F \approx 21\%$ independently of the side-groups attached. This is almost by two orders of magnitude larger as compared to Φ_F values obtained in solution. The Φ_F enlargement in PS host, which occurred solely due to the intramolecular effects, was accompanied by considerable slowing of fluorescence transients with respect to those in solution (see an example for CNPz-OCyclHept in Figure 4.6) and clearly signified suppression of intramolecular torsions in the environment of increased rigidity. Further Φ_F enhancement with increasing compound concentration above 2 wt % in PS was unambiguously caused by intermolecular AIEE mechanism, that is, specific molecule stacking likely followed by intramolecular planarization similar to that revealed in cyano-stilbenes.[145] Electron microscopy and fluorescence microscopy data also provided support for such molecule stacking into nanostructures

occurring in PS films. Interestingly, Φ_F enhancement for some of the side-groups was notably larger (Figure 4.5c) than for the others (Figure 4.5b).

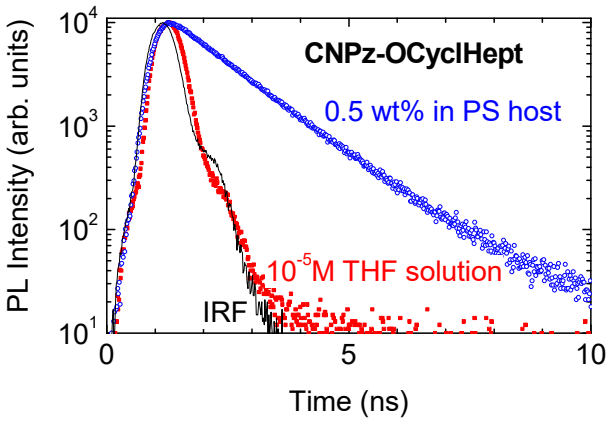

Fig. 4.6. Fluorescence transients of CNPz-OCyclHept in 10^{-5} M THF solution (red curve) and polystyrene host at 0.5 wt % concentration (blue curve). Instrument response function (IRF) almost coinciding with the transient in solution is shown for reference (black curve).

Mainly the compounds with relatively long and branchy side-groups, such as nonyloxy or dihexylmethoxy, demonstrated greater than 2-fold enhancement, from 20% to about 50%, due to the more favorable molecule packing. We note that AIEE could only be achieved for slowly dried PS films, such as those obtained by drop-casting from toluene solution, whereas films prepared by quickly evaporating solvent, *e.g.*, by spin-coating, showed no AIEE behavior. The slow drying was essential in providing extra time necessary for diffusion-driven specific molecule stacking leading to AIEE. Intriguingly, just before manifestation of AIEE, an increase of compound concentration from 0.06 to 2 wt % in PS host caused slight decrease of Φ_F (Figure 4.5b and 4.5c). This decrease could be explained by the absence of critical compound concentration in PS inhibiting proper intermolecular arrangements (necessary for Φ_F enhancement) and formation of molecular dimers (i.e. non-emissive H-aggregates) due to the molecules being too far apart and trapped in

between the polymer chains. Such molecule arrangements resulted in a usual concentration quenching of fluorescence such as that observed for CNPz-OCyclHept in the whole concentration range 0.06 - 100 wt % (Figure 4.5a).

4.1.3 Absorption and fluorescence spectroscopy of PDACN nanoparticles

The AIEE effect as a function of the different side groups was more closely inspected during the process of molecule aggregation, which was accomplished by precipitation of PDACN nanoparticles in aqueous solution. To elucidate the emission enhancement in the aggregated state and to relate the enhancement with molecular structure, in fact predetermining packing morphology in the aggregates, absorption and fluorescence spectroscopy in combination with fluorescence quantum yield and lifetime measurements were carried out. Three PDACN compounds bearing cycloheptyloxy (CNPz-OCyclHept), hexyloxy (CNPz-OHex) and dihexylmethoxy (CNPz-OMeDiHex) side groups and expressing aggregation-caused quenching, moderate and strong AIEE effect, respectively (see Figure 4.5a-c), were selected as representatives for demonstrating essential differences in their spectroscopic behavior. Figure 4.7, 4.8 and 4.9 show absorption and fluorescence spectra dynamics of each representative compound in THF/water mixtures with increasing water fraction. Roughly below 50 v/v % of water, absorption and fluorescence spectra of all the studied PDACN derivatives look identical and are typical of isolated molecules. This is in agreement with identical HOMOs and LUMOs of the studied derivatives, which were found to be unperturbed by the side groups (Figure 4.2). However, above the limiting water fraction (50 v/v %) separating isolated molecules and formed aggregates (nanoparticles), the spectral dynamics with increasing

water content becomes strongly dependent on the side groups. Namely CNPz-OCyclHept, above the limiting water fraction exhibits single structureless absorption band centered at 370 nm, which remains unchanged up to 98 v/v % of water (Figure 4.7a). Correspondingly, increasing water fraction negligibly affects fluorescence spectrum of

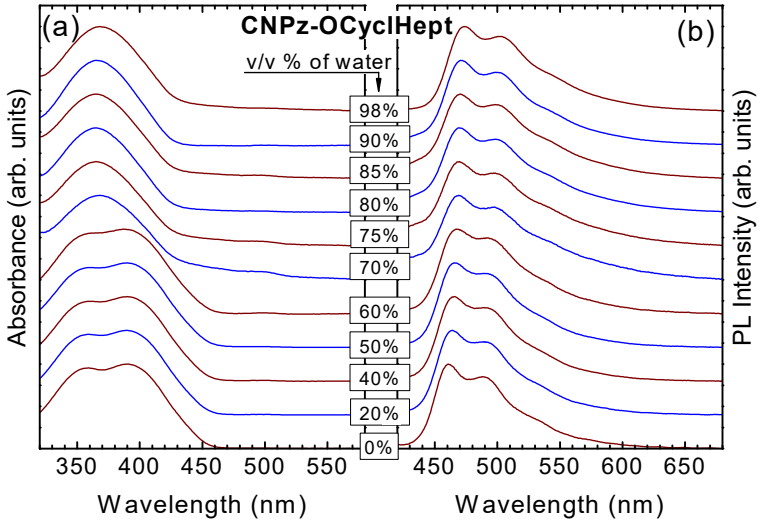

Fig. 4.7. Absorption (a) and fluorescence (b) spectra of CNPz-OCyclHept in THF/water mixture with different volume percent (v/v %) of water. The intensity of each spectrum has been scaled and arbitrarily shifted for clarity.

CNPz-OCyclHept up to the largest water fraction (Figure 4.7b). The spectrum remains very similar to that of isolated molecules, although slight broadening at high water contents can be noticed. Relatively small changes of the spectrum, particularly of the fluorescence spectrum, occurring upon CNPz-OCyclHept aggregation imply weak intermolecular interactions and thus loose molecule packing in the formed nanoparticles. Analogous dynamics was also obtained for CNPz-OEtHex compound bearing ethylhexyloxy side groups, which justified the importance of rather bulky and branchy side groups for loose packing morphology.

In sharp contrast to CNPz-OCyclHept, the spectral dynamics of CNPz-OHex above 50 v/v % of water indicate an emergence of new absorption band at 470 nm due to aggregates with well-resolved vibronic

replicas (Figure 4.8a).The replicas smoothen at the largest water fractions (>75 v/v %) as another band, in this case broad and structureless, appearing in the background at shorter wavelengths (~400 nm) strengthens in intensity.

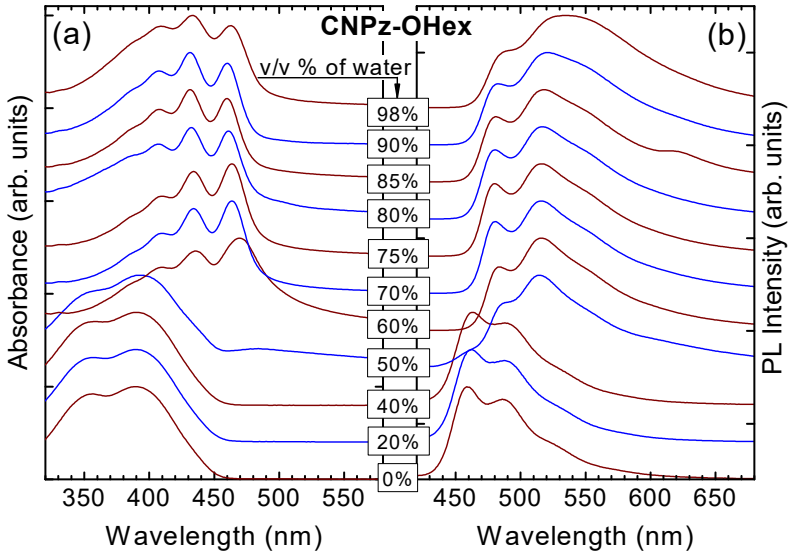

Fig. 4.8. Absorption (a) and fluorescence (b) spectra of CNPz-OHex in THF/water mixture with different volume percent (v/v %) of water. The intensity of each spectrum has been scaled and arbitrarily shifted for clarity.

Similar tendency is observed in the fluorescence spectra dynamics with increasing water content (Figure 4.8b). Above the limiting water fraction molecular spectrum suddenly transforms into the spectrum of aggregates, which manifests with a new band located at 520 nm. Further increase in the water fraction broadens the aggregate band similarly to that of absorption spectra. The well-expressed vibrational modes of the aggregate band indicate increased rigidity and highly-ordered arrangement of the molecules, which are typical to crystalline solids due to strong intermolecular interactions. Conversely, in amorphous solids due to the absence of long-range periodicity, intermolecular interactions are slightly different at different local sites resulting in the shift of vibronic frequencies, and consequently, in

broadened and washed out spectra. The later features can be traced in the structureless absorption band emerging at about 400 nm.

Importantly, the adjustment of alkoxy chain length was found to enable tuning of the relative intensities of both aggregate bands, *i.e.*, the vibronically modulated absorption band and that with broad and structureless shape. CNPz-OHex and CNPz-ONon compounds with long hexyloxy and nonyloxy side chains expressed analogous dynamics, where aggregate absorption were dominated by vibronically modulated band for all THF/water ratios. In contrast, the structureless aggregate band in the absorption spectra of CNPz-OMe compound bearing short methoxy side groups overtook domination at the largest water fractions. This result illustrates that by varying alkoxy side chain length the PDACN nanoparticles with the different prevalent aggregate state can be obtained. Selective excitation of the vibronically modulated and of the structureless band of CNPz-OHex aggregates formed at 98 v/v % of water yielded similar Φ_F implying efficient energy transfer between the different states. Since the efficient energy transfer is only possible for the states being within the Förster radius (a few nanometers)[146], it is likely that the states are intermixed in the aggregates.

Absorption and fluorescence spectra dynamics of CNPz-OMeDiHex bearing branchy alkyl side groups is found to be more complex (Figure 4.9). In fact certain spectroscopic signatures can be traced back to the two previous compounds. An increase of the water fraction above 50 v/v % causes the appearance of a new band at about 470 nm in the absorption spectra, and simultaneously, a band at 520 nm in the fluorescence spectra. Although the new absorption band associated with the aggregated phase is rather broad, it still contains discernible vibronic modes. Meanwhile, the new fluorescence band is found to be identical to that of compound CNPz-OHex observed for water fraction above 50 v/v % (Figure 4.8). Surprisingly, addition of water from 70 v/v % to 85 v/v %

gives rise to the new aggregate bands in the absorption and fluorescence spectra, which are very similar to the aggregate bands of compound

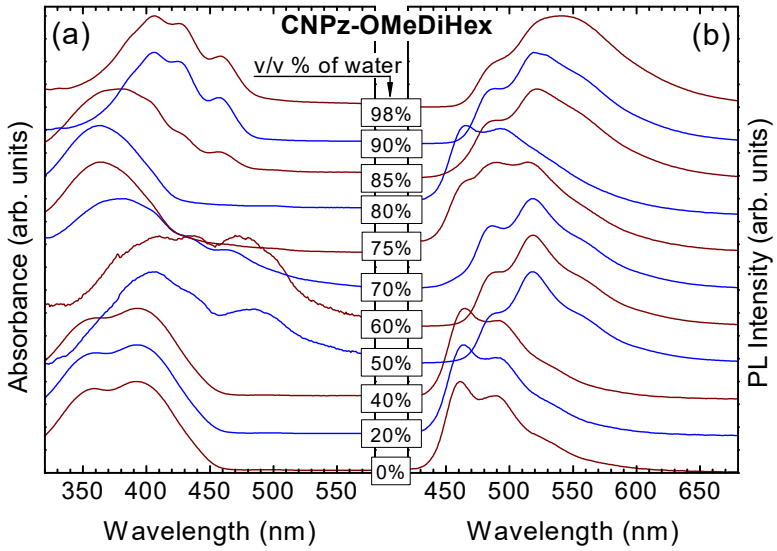

Fig. 4.9. Absorption (a) and fluorescence (b) spectra of CNPz-OMeDiHex in THF/water mixture with different volume percent (v/v %) of water. The intensity of each spectrum has been scaled and arbitrarily shifted for clarity.

CNPz-OCyclHept (Figure 4.7). The absorption band is structureless and centered at 370 nm, whereas the fluorescence band resembles spectrum of isolated molecules. However, further increase of the water content above 85 v/v % restores the spectra back to those analogous of compound CNPz-OHex. The similarity is particularly obvious for the fluorescence spectra of compounds CNPz-OMeDiHex and CNPz-OHex at the highest water fractions. Thus, spectral dynamics of CNPz-OMeDiHex with increasing water content actually hint on the different aggregate phases (or packing morphologies) formed in accordance to the chosen solvent/non-solvent ratio in the mixture. Clearly resolved spectroscopic signatures in Figure 4.9 suggest that three different packing morphologies are formed in the THF/water mixtures for the following water fractions, 50 - 70 v/v %, 70 - 85 v/v % and 85 -98 v/v %. Most importantly, the nanoaggregates of different morphologies can be easily realized by

utilizing single PDACN compound functionalized with long and branchy dihexylmethoxy-type of side chains.

Spectroscopically identified dominating aggregate morphologies along with the extrema Φ_F values for all the studied PDACN compounds are listed in Table 1. Since the absorption-based measurements permit probing all optically-active states including the non-emissive ones, directly inaccessible by fluorescence, the measurements have been chosen as the most suited for evaluation of dominant morphologies.

Table 1. Dominant morphology and extrema Φ_F values of the PDACN nanoparticles as revealed from the Φ_F and absorption spectra dynamics with increasing water fraction. Percentage error of QY values is 5%.

Compound	Dominant aggreg. morphology (H_2O fraction in THF/H_2O mixture)	Extrema values of Φ_F, %
CNPz-OMe	Cryst. (50 - 90 v/v %), Amorph. (90 - 98 v/v %),	38 @60 v/v % 17 @98 v/v %
CNPz-OHex	Cryst. (50 - 98 v/v %)	60 @60 v/v % 20 @98 v/v %
CNPz-ONon	Cryst. (50 - 98 v/v %)	32 @60 v/v % 15 @70 v/v % 52 @90 v/v %
CNPz-OEtHex	Amorph. (50 - 98 v/v %)	6.0 @98 v/v %
CNPz-OCyclHept	Amorph. (50 - 98 v/v %)	6.0 @98 v/v %
CNPz-OMeDiHex	Cryst. (50 - 70 v/v %), Amorph. (70 - 85 v/v %), Cryst. (85- 98 v/v %)	40 @60 v/v % 2.0 @80 v/v % 70 @90 v/v %
CNPz-OBn	Cryst. (50 - 98 v/v %)	41 @70 v/v % 18 @85 v/v %
CNPz-Ph	Cryst. (50 - 90 v/v %), Amorph. (90 - 98 v/v %),	30 @85 v/v % 8.0 @98 v/v %

Table 1 evidences that crystalline phase is favored for the compounds featuring long alkoxy side groups such as CNPz-OHex and CNPz-ONon, whereas purely amorphous phase is inherent for the less structurally-

regular compounds possessing bulky or branchy side groups like CNPz-OCyclHept and CNPz-OEtHex. Generally for structurally-regular compounds, at relatively low water fraction molecules tend to arrange in an ordered fashion constituting crystalline phase. This is a typical crystallization process driven by molecule diffusion in the bulk.[147,148] Meanwhile at increased water fraction, and consequently reduced compound solubility in THF/water mixture, rate of nanoparticle formation increases drastically. This increases amount of amorphous phase in the nanoparticles of the most compounds (CNPz-OMe, CNPz-OHex, CNPz-ONon, CNPz-OMeDiHex, CNPz-OBn, CNPz-Ph), what is manifested by diminished Φ_F values (see Table 1). However, only for the few compounds (CNPz-OMe and CNPz-Ph) bearing relatively small side groups the amorphous phase prevails over crystalline at the largest water fractions. The most unusual case is that of CNPz-OMeDiHex (discussed above), where the crystalline ordering being the dominant one at low water fraction (~60 v/v %), and yet surpassed by amorphous phase at somewhat higher water fraction (~80 v/v %), start dominating again at the highest water fraction (>90 v/v %). This intricate phenomenon is discussed below.

4.1.4 Fluorescence quantum yield and lifetime dynamics of PDACN nanoparticles

Figure 4.10 depicts Φ_F and fluorescence lifetime of the three representative compounds CNPz-OCyclHept, CNPz-OHex and CNPz-OMeDiHex in THF/water mixtures with increasing water content. The presence of non-interacting molecule species below 50 v/v % of water implies geometrically unrestricted relaxation to the ground state via low-frequency intramolecular torsions/vibrations resulting in nearly zero Φ_F and extremely short excited state lifetime (<70 ps). Although the

limitations of our experimental setup do not permit evaluation of shorter lifetimes, such values can be assumed to be zero in the nanosecond time scale within the accuracy of 7%.

Generally, nanoparticle precipitation initiated by the increased water fraction promoted AIEE in all the PDACN compounds. However, the AIEE effect was found to be relatively small for the compound CNPz-OCyclHept exhibiting concentration quenching in PS host (Figure 4.10a).

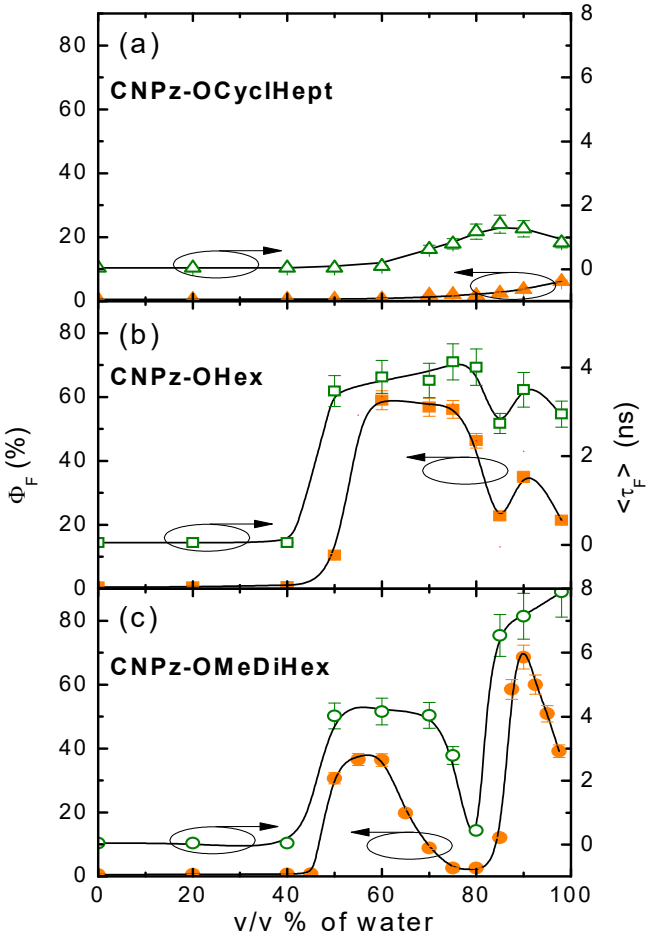

Fig. 4.10. Fluorescence quantum yield (solid points) and average fluorescence lifetime (white points) of CNPz-OCyclHept (a), CNPz-OHex (b) and CNPz-OMeDiHex (c) as a function of volume percent (v/v %) of water in THF/water mixture. Zero point of the $<\tau_F>$ axis has been arbitrarily shifted for clarity.

For this compound Φ_F was enhanced by only an order of magnitude, from 0.6% to 6%. The small AIEE complied with the weak intermolecular

interactions in the nanoparticles revealed from the spectroscopic data (Figure 4.7a). On the other hand, the AIEE was much more profound for the rest PDACN derivatives. In this case, Φ_F was enhanced by almost two orders of magnitude, from 0.6% to 40% and above. The examples of remarkable AIEE are illustrated in Figure 4.10b and 4.10c for CNPz-OHex and CNPz-OMeDiHex, respectively. Interestingly, here Φ_F behavior with increasing water fraction is found to be nonmonotonous. In the case of CNPz-OHex, Φ_F first increases up to 60% at the 60 - 75 v/v % of water and then decreases down to 20% above 75 v/v % of water (Figure 4.10b). Note that the later decrease is consistent with the concomitant growth of unstructured slope at ~400 nm in the absorption spectra (Figure 4.8a). Variations in fluorescence intensity accompanied by changes in color upon nanoparticle formation are highlighted in the pictures of the THF/water mixtures with increasing water fraction (see Figure 4.11). In the case of

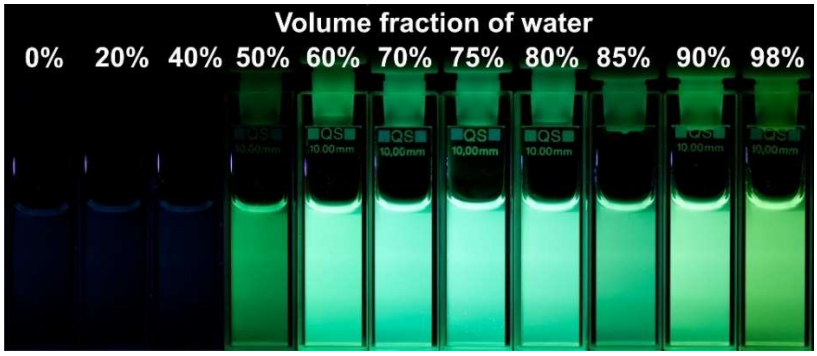

Fig. 4.11. Pictures of the compound CNPz-OHex in THF/water mixtures with increasing volume percent (v/v %) of water under UV excitation.

CNPz-OMeDiHex, an increase of Φ_F up to 40% at the 50 - 60 v/v % of water is followed by the steep decrease of Φ_F down to 2% at the 75 - 80 v/v % of water, and then again, sudden increase of Φ_F up to 70% at about 90 v/v % of water, which is followed by rapid decrease of Φ_F above 90 v/v % of water (Figure 4.10c). Such wavy Φ_F profile agrees well with the complex spectra dynamics of compound CNPz-OMeDiHex shown in Figure 4.9. Particularly, each boost in Φ_F is accompanied by the

appearance of new aggregate bands enriched with vibronic modes and redshifted with respect to molecular spectra. Meanwhile the drop in Φ_F is followed by the emergence of structureless aggregate band located at the shorter wavelengths.

The distinctive Φ_F behaviors with increasing water content were reflected in the excited state relaxation dynamics of the PDACNs revealed from fluorescence transients. The transients of a few representative compounds CNPz-OCyclHept and CNPz-OMeDiHex at different water fractions are displayed in Figure 4.12. Estimated average

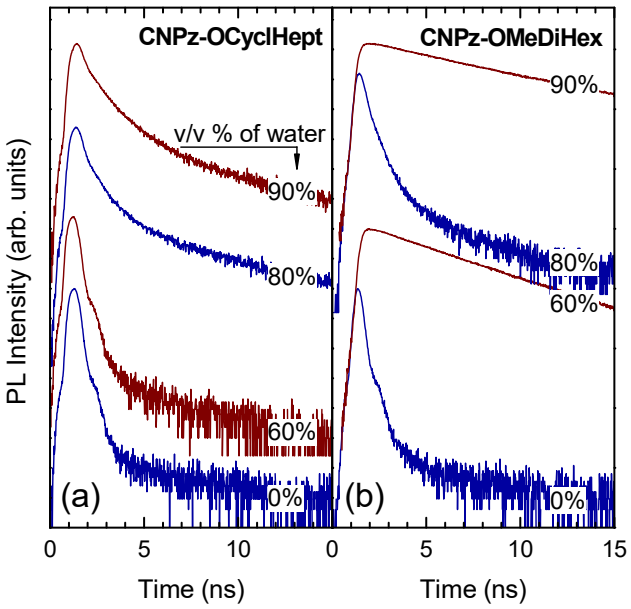

Fig. 4.12. Fluorescence transients of CNPz-OCyclHept (a) and CNPz-OMeDiHex (b) in THF/water mixtures with different volume percent (v/v %) of water shown in logarithmic scale. The intensity of each transient has been scaled and arbitrarily shifted for clarity.

fluorescence lifetimes ($<\tau_F>$) are depicted in Figure 4.10. The rapid fluorescence decay observed for the isolated CNPz-OCyclHept molecules in solution (below 50 v/v % of water) gradually slows down upon molecule aggregation (above 50 v/v % of water) as a result of increasing restriction of intramolecular motions. The relatively weak and gradual changes of the

lifetime are associated with rather weak intermolecular interactions in CNPz-OCyclHept aggregates due to the bulky cycloheptyloxy side groups. The bulky groups prevent tight molecule packing into special patterns in the nanoparticles, what disallows complete suppression of vibrational/torsional relaxation modes responsible for fast excited state deactivation. In sharp contrast, the rapid fluorescence decay of CNPz-OMeDiHex molecules in solution is abruptly slowed down upon aggregate formation resulting in a remarkable increase of τ up to 4 ns at 60 v/v % of water. An addition of water fraction up to 80 v/v % gives rise to the aggregates showing sub-nanosecond relaxation time, whereas further increase of the water content up to 90 v/v % immediately restores the τ back to the nanosecond time scale again. Such abrupt variations of the lifetime are likely associated with the dramatic changes in molecule packing morphology, and also with suppression or permission of vibrational/torsional relaxation, thus enabling fluorescence on-off switching. These distinct attributes of radically different molecular arrangements of CNPz-OCyclHept and CNPz-OMeDiHex (or CNPz-OHex or CNPz-ONon) are also easily traced from the direct comparison of their fluorescence spectra and transients obtained in solution and solid state. Note that independent estimates of average fluorescence lifetimes nicely follows Φ_F and spectra dynamics with increasing water content, what confirms reliability of the experimental data and strengthens the argument about the existence of different aggregate morphologies, which can be tuned by simply altering solvent (THF) to non-solvent (water) ratio in THF/water mixture.

4.1.5 Electron and polarized optical microscopy of nanoparticles

Scanning electron microscopy (SEM) and polarized optical microscopy (POM) were employed to visualize PDACN nanoparticles, and

additionally, to confirm the different packing morphologies, which were indirectly revealed from the fluorescence quantum yield, lifetime and spectral dynamics. SEM images of CNPz-OCyclHept, CNPz-OEtHex and CNPz-OBn nanoparticles prepared in the THF/water mixtures with 90 v/v % of water and casted on pre-cleaned silicon substrates are shown in Figure 4.13a, b and c. The images indicate a spherical shape of the nanoparticles with mean diameters of about 50 nm for CNPz-OCyclHept and CNPz-OEtHex (Figure 4.13a, b), which demonstrate structureless spectral bands of the aggregates due to random and loose molecule

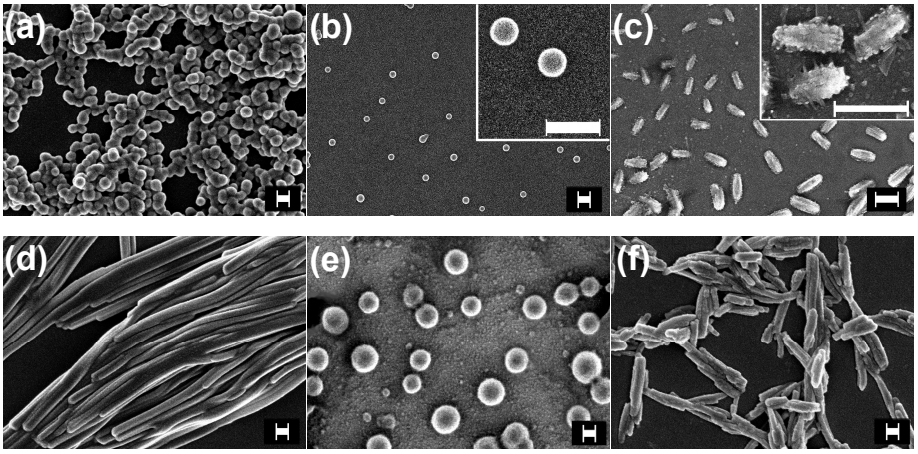

Fig. 4.13. Electron microscopy images of CNPz-OCyclHept (a), CNPz-OEtHex (b), CNPz-OBn (c) nanoparticles formed in THF/water mixtures with 90 v/v % of water and CNPz-OMeDiHex nanoparticles formed in the mixtures with 60 (d), 80 (e) and 90 v/v % (f) of water. The scale bar for (a, b, d, e, f) is 100 nm and for (c) is 500 nm.

packing. On the other hand, CNPz-OBn nanoparticles have rather intricate shape (see Figure 4.13c and the inset). They are seen to be composed of many nanoneedles of a well-defined shape. Clearly resolved vibronic modes in the absorption spectra of nanoneedles suggest crystalline morphology as a dominant one (Table 1). Reducing water fraction down to 60 v/v % is found to cause a continuous increase in the nanoparticle sizes up to about 1 μm. The size tunability in the sub-micron range was confirmed *in situ* in the THF/water mixtures by DLS technique (see

Figure 4.14). Note that the correct estimation of nanoparticle sizes by DLS was only possible for CNPz-OCyclHept and CNPz-OEtHex compounds forming spherical particles due to the limitations of evaluation method used. The technique tends to overestimate actual particle diameters, what is more noticeable for the smaller nanoparticles. The DLS measurements also indicated that additional size tuning can be achieved via altering compound concentration in the mixture. A decrease in nanoparticle diameter with decreasing compound concentration has been clearly evidenced.

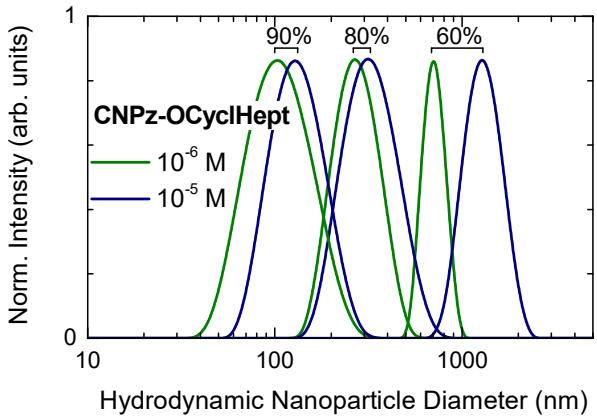

Fig. 4.14. Size distributions of CNPz-OCyclHept nanoparticles formed in THF/water mixtures with 60, 80, and 90 v/v % of water and at 10^{-6} M (green line) and 10^{-5} M (blue line) compound concentrations.

SEM images of CNPz-OMeDiHex nanoparticles prepared at different water fractions demonstrate drastic differences in aggregate size and shape (Figure 4.13d, e and f). Highly fluorescent aggregates formed at 60 and 90 v/v % of water have a shape of long and short nanowire-like structures, respectively. The long nanowires are about 6 μm in length and have a mean diameter of 80 nm, whereas the short ones are 50 nm in diameter and at most 500 nm in length. The smaller nanowires exhibit almost twice as high fluorescence efficiency (Φ_F=70%) as compared to the longer ones (Φ_F=40%), which is likely due to the different molecule packing. Attempts to reveal packing morphology in the nanowires by x-

rays diffraction were unsuccessful due to inability to obtain larger crystals, however different absorption bands, different fluorescence lifetimes and efficiencies associated with the longer and shorter nanowires hinted that different molecular packing is indeed very probable. Interestingly, poorly fluorescent (Φ_F=2%) CNPz-OMeDiHex nanoaggregates formed at 80 v/v % of water and expressing structureless spectral bands have spherical shape with a mean diameter of about 150 nm.

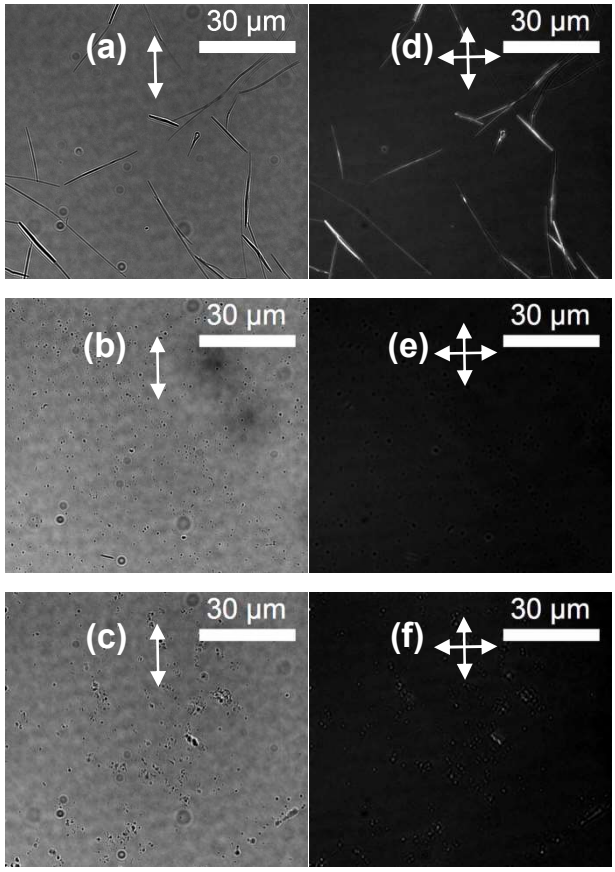

Fig. 4.15. Polarized optical microscopy images of the CNPz-OMeDiHex nanoparticles formed in the THF/water mixtures with 60 (a,d), 80 (b,e) and 90 v/v % (c,f) of water under parallel (a,b,c) and crossed (d,e,f) polarizers.

To confirm the amorphous nature of spherical aggregates and crystalline morphology of the nanowire-like particles, POM experiments were carried out (Figure 4.15). Long and short nanowire-like aggregates equally nicely discernible under parallel and crossed polarizers (compare Figure 4.15a with d and c with f) imply strong birefringence, which

unambiguously indicates their crystallinity. Conversely, completely dark optical image of the round nanoparticles observed under crossed polarizers (compare Figure 4.15b with e) signifies the absence of birefringence, and is a signature of their amorphous nature. Unfortunately, it was impossible to resolve particles with diameter smaller than 400 nm (the case of Figure 4.15b, c, e and f) due to the limitations imposed by optical diffraction, nevertheless somewhat enlarged aggregates as dark(bright) spots under parallel(crossed) polarizers could still be clearly discerned.

Thus, POM results support previously discussed SEM and spectroscopic data, which imply facile tuning of the nanoparticle morphology (crystalline → amorphous → crystalline) and the corresponding emission switching (emissive → non-emissive → emissive) with a maximum contrast of over 30 achieved for CNPz-OMeDiHex by adjusting solvent/non-solvent ratio in the mixture. While the appearance of non-emissive amorphous phase with the increasing water fraction (*i.e.* decreasing THF/water ratio) can be naturally understood by the inhibition of diffusion-driven ordered molecule packing due to decreased compound solubility and thus enhanced nanoparticle formation rate, the re-appearance of the crystalline phase at the highest water fractions (for THF/water ratio <1/9) is rather unusual. Such intricate nanoparticle morphology change governed by solvent/non-solvent ratio has not been observed yet. The re-appearance of the crystalline phase at high molecule concentration (low compound solubility) can be explained by the surfaced-enhanced crystallization phenomenon,[147,149,150] which becomes increasingly important with the reduced nanoparticle size, and thus increased surface to volume ratio. The phenomenon implies much faster growth of the crystals from amorphous phase on the nanoparticle surface than in the interior and is sustained by enhanced molecular diffusion at the surface. Moreover, highly fluorescent nanocrystallites formed at

THF/water ratio <1/9 constitute a different polymorph as compared to that formed at the ratio of 1/1. The different polymorphs can be justified by the different spectral bands ascribed in the absorption spectra (Figure 4.9) as well as by the distinct fluorescence lifetimes and quantum yields (Figure 4.10). Remarkably, such sharp alteration of nanoparticle morphology accompanied by high-contrast variation in emission efficiency is facilitated by long and branchy dihexylmethoxy-type of side chains. The other studied alkoxy or cyclic side groups have either failed to achieve such sharp morphology tuning or the tuning was marginal.

4.1.6 Vapour sensing by fluorescent nanoparticles

For a simple demonstration of the applicability of the PDACN nanoparticles in vapor sensing, the compound CNPz-OMeDiHex with Φ_F of up to 70% and the compound CNPz-OCyclHept with Φ_F of only up to 6% in the aggregated state were used. Amorphous neat films of CNPz-OMeDiHex and CNPz-OCyclHept were prepared on the glass substrates from solution by quickly evaporating the solvent (Figure 4.16a and 4.17a). The absence of crystallinity of the as-prepared films was confirmed by fluorescence spectrum, which was found to be similar to the spectrum of the compounds in a dilute solution. Exposure of the defined area of the CNPz-OMeDiHex film to THF vapor for a few seconds resulted in a sudden change of the color of that area from greenish-blue to vivid yellowish-green. A close inspection of the exposed area by using fluorescence microscope revealed highly fluorescent fiber-like particles with a sub-micron diameter (Figure 4.16b). The nanoparticles were confirmed to be

crystalline from their fluorescence spectra, which were identical to those

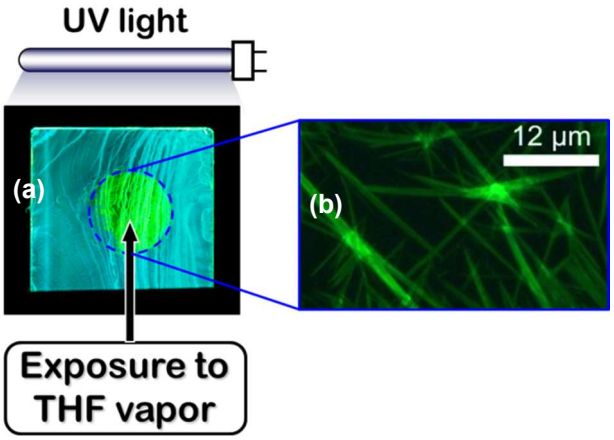

Fig. 4.16. Fluorescence image of the neat CNPz-OMeDiHex film with the highlighted area exposed to THF vapor (a). Fluorescence microscopy image of the highlighted area (b). The images were taken under UV excitation.

of the long nanowire-like aggregates formed in THF/water mixture at 50 – 60 v/v % of water. The formation of the crystalline nanowires was obviously caused by a sudden drop in a viscosity of the rigid surroundings due to the penetration of solvent vapour into the film, what facilitated diffusion-driven ordering of the molecules into crystalline nanoparticles. The formed crystalline particles were found to be very stable implying such sensor based on the amorphous-to-crystalline phase changes irreversible.

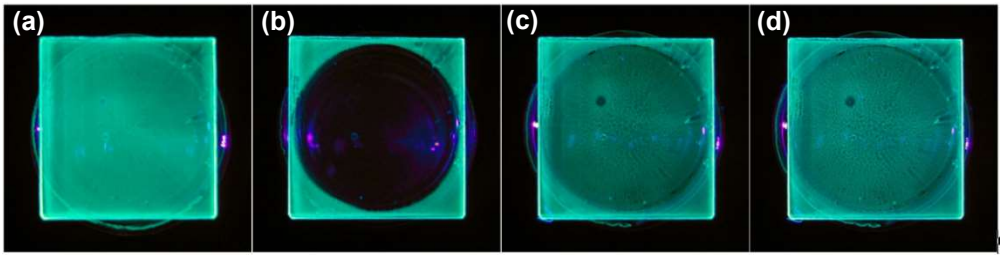

Fig. 4.17. Fluorescence image of the neat CNPz-OCyclHept film under UV excitation and before exposure (a), 0 s after exposure (b), 10 s after exposure (c) and 30 min after exposure (d) to THF vapor. The images (b), (c) and (d) were taken with THF vapor stimulus removed.

Unlike for CNPz-OMeDiHex, exposure of amorphous neat film of CNPz-OCyclHept to THF vapor did not result in a color change, but rather caused fluorescence quenching (Figure 4.17a and b). Formation of highly crystalline nanoparticles in this case was precluded by the bulky cycloheptyloxy side groups, which conditioned weak intermolecular interactions, and therefore, favoured dissolution over association. The fluorescence quenching was related to the lessened suppression of intramolecular torsions due to the vapour-induced solubilization of the film. The exposed area of fluorescent amorphous film could be recovered to a large degree under ambient conditions after removing THF vapor stimulus and letting the film dry for a few minutes (Figure 4.17c and d). The change in fluorescence signal of these films was noticeable by the naked eye at THF/air molar ratio as low as 1 to 100. Thus, the above demonstrations clearly show the applicability of the PDACN-based compounds for unassisted eye sensing of volatile organic vapor via distinct change in fluorescence color or intensity.

4.1.7 PDACN in PS host for vapour and threshold temperature sensing

Change of the phase (from molecular to aggregated) can also be promoted, e.g., by diffusion of molecularly dispersed dye in the dye/polymer blend induced by the thermal annealing of blend (above the glass transition temperature (T_g) of the polymer)[151]. Such mechanism allowed demonstration of fluorescent threshold temperature and deformation sensors based on bis(benzoxazolyl)stilbene/ and bis(cyano-styryl)benzene/polymer blends obtained by melt-processing technique[152,153]. Formation of aggregates triggers the redshift of fluorescence spectra, which is easily visible by a naked eye. A similar

diffusion-induced aggregation of molecules was also observed via exposure of dye-doped polymer matrices to organic solvent vapour [154–156].

CNPz-OMeDiHex compound showing a particularly strong optical response to the alteration of aggregate morphology was chosen as the best candidate to be dispersed in dye-doped polystyrene films. These films can be easily prepared by a simple spin-coating technique and possibly can be utilized as fluorescent threshold temperature or organic solvent vapour sensors. For comparison, a similar PDACN derivative (CNPz-OMeDiHex-2) featuring extended conjugation backbone was synthesized and studied in regard to its ability to form fluorescent aggregates upon application of the mentioned external stimuli. Extention of the conjugation of the *p*-divinylbenze backbone is expected to affect the molecular geometry thereby influencing intermolecular interaction, packing morphology, and consequently, optical response to the stimuli.

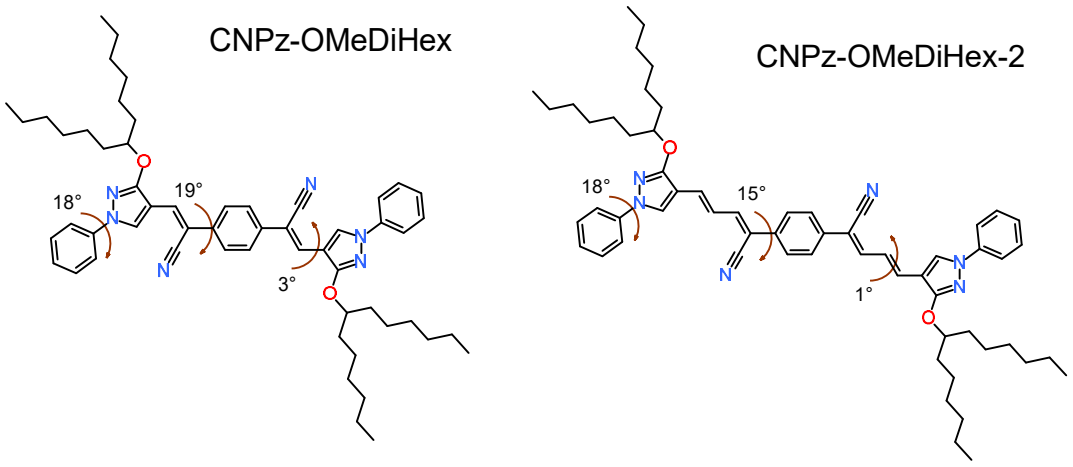

Fig. 4.18. Chemical structures of the PDACN compounds CNPz-OMeDiHex and CNPz-OMeDiHex-2. Dihedral angles of the backbone are indicated.

Ground state geometry optimization of the two PDACN compounds carried out using density functional theory revealed some differences in the dihedral angles of the backbone (Figure 4.18). Namely,

somewhat stronger twisted backbone (the larger angles) was obtained for CNPz-OMeDiHex as compared to that for CNPz-OMeDiHex-2 featuring extended conjugation backbone. No other distinct differences in the equilibrium geometries were found.

Φ_F of the two PDACNs was examined as a function of their concentration in a rigid PS host. The PS films for this study were prepared by drop-casting from THF solutions to examine the aggregation process under slow solvent evaporation conditions. At the lowest concentrations CNPz-OMeDiHex and CNPz-OMeDiHex-2 exhibited Φ_F as high as 20% and 25%, respectively (see Fig. 4.19). Somewhat higher Φ_F obtained for CNPz-OMeDiHex-2 was caused by more conjugated and more rigid molecular backbone. Meanwhile, increase of the concentration above 5 wt % greatly affected Φ_F values due to the prevalence of intermolecular interactions. Typical concentration quenching effect was observed for CNPz-OMeDiHex-2, which conditioned the reduction of fluorescence quantum yield down to 8% in the neat film. Conversely, increase of Φ_F with the concentration of CNPz-OMeDiHex indicated AIEE behaviour. Φ_F of up to 47% was attained in the neat film of CNPz-OMeDiHex.

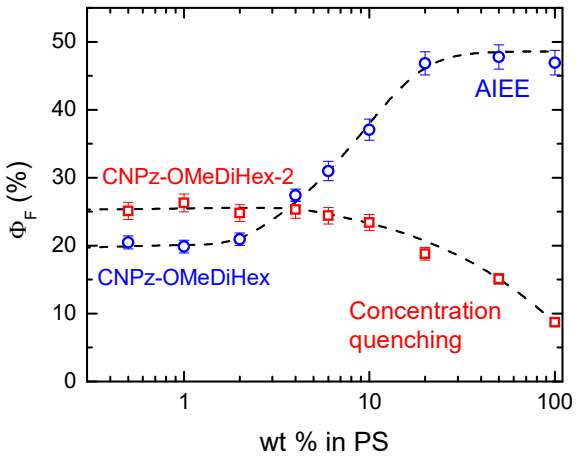

Fig. 4.19. Emission quantum yield of CNPz-OMeDiHex and CNPz-OMeDiHex-2 as a function of their concentration in PS matrix.

Fluorescence spectra of the spin-coated PS films doped with different wt % of CNPz-OMeDiHex and CNPz-OMeDiHex-2 are shown in Figure 4.20. PS films containing 1 and 5 wt % of CNPz-OMeDiHex demonstrate vibronicaly-modulated emission spectra with maxima in the blue spectral range (at 460 nm). The spectra look identical and are typical of isolated molecules in THF solution. Such fluorescence behaviour suggests weak intermolecular coupling of CNPz-OMeDiHex in the polymer film. Increase of compound concentration above 5 wt % in PS matrix results in the more intense fluorescence at 490 nm for 10 wt % in PS and in appearance of a new fluorescence band at about 540 nm for 20 wt % in PS due to the aggregation of CNPz-OMeDiHex. An extension of the

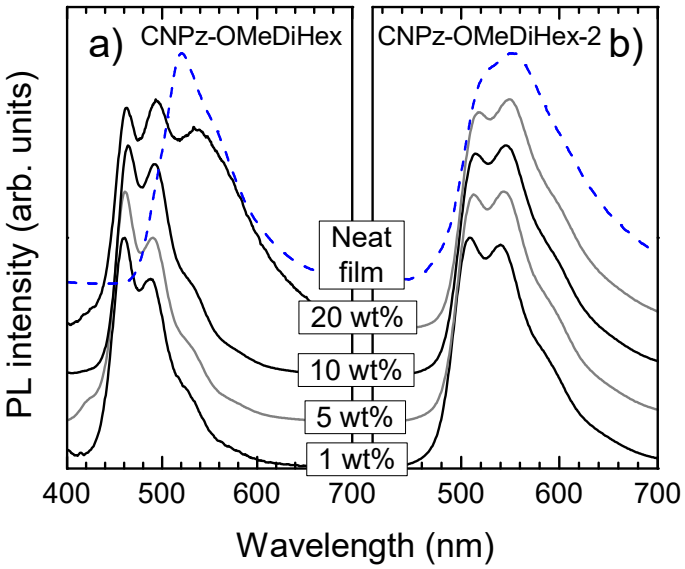

Fig. 4.20. Normalized fluorescence spectra of CNPz-OMeDiHex (a) and CNPz-OMeDiHex-2 (b) as a function of compound concentration (indicated) in PS matrix. Dashed lines represent data for the neat films. Spectra are arbitrarily shifted for clarity.

conjugation (the case of CNPz-OMeDiHex-2) results in a green fluorescence of isolated molecules with maxima at 505 nm, whereas variation of the compound concentration in PS host has negligible effect

on its emission spectra. This clearly indicates much weaker intermolecular interactions for CNPz-OMeDiHex-2 as compared to CNPz-OMeDiHex even at the highest concentrations.

Absorption and fluorescence spectra of CNPz-OMeDiHex in PS matrix as a function of thermal annealing duration is shown in Fig. 4.21a and b, respectively. Spectra of dilute THF solution and PS film with 1 wt % are included for comparison. The annealing temperature (110 °C) was intentionally chosen to be above T_g of the PS to cause polymer host softening and diffusion of CNPz-OMeDiHex molecules. For this and further external stimuli experiments PS films doped with 5 wt % of compounds were utilized as demonstrating behaviour related to weak intermolecular interactions before the treatment.

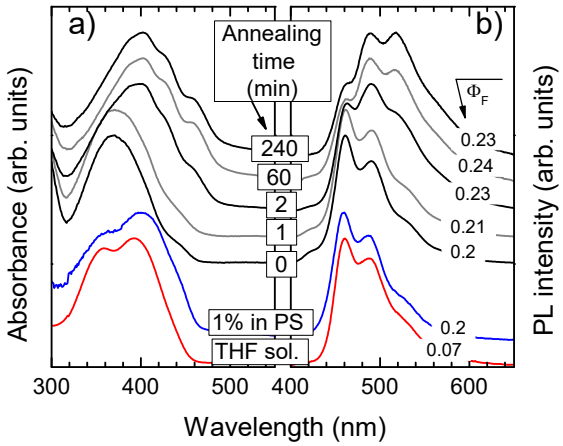

Fig. 4.21. Normalized absorption (a) and fluorescence (b) spectra of PS films with 5 wt % of CNPz-OMeDiHex as a function of annealing duration. Spectra of dilute THF solution and PS film of 1 wt % are included for comparison. Spectra are arbitrarily shifted for clarity. Fluorescence quantum yield values are indicated.

The untreated PS film doped with 5 wt % of CNPz-OMeDiHex demonstrates structureless absorption spectra with maximum at 370 nm, which differs from monomolecular absorption observed in THF solution or dilute (1 wt %) PS film. This can be attributed to instantaneous formation of molecular dimers during the film preparation. Similar phase

containing H-aggregates of CNPz-OMeDiHex was observed in nanoparticles prepared by precipitation method (see Figure 4.9). Further annealing of the films results in the sharper and more pronounced vibronic structure of absorption spectra. These transformations are in good correspondence with fluorescence spectra dynamics of CNPz-OMeDiHex/PS films for the same annealing time range. Annealing of the blue-emissive films for 2 min at 110 °C results in a 35 nm redshift of fluorescence maximum and an emergence of the new fluorescence peak at 520 nm after 4 h of thermal treatment. Interestingly, annealing of PS films doped with 5 wt % of CNPz-OMeDiHex-2 at the same temperature for 4 h has no effect on its fluorescence properties.

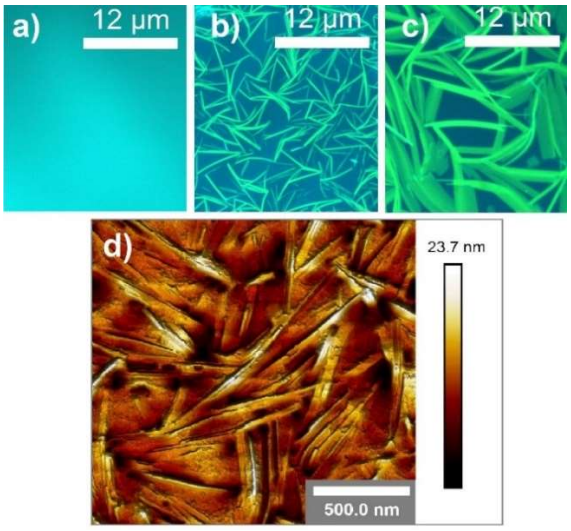

Fig. 4.22. Fluorescence microscopy images of PS films doped with 5 wt % of CNPz-OMeDiHex before annealing (a) and after annealing for 2 min (b) and 4 hours (c). AFM image of the film annealed for 4 hours (d). Images (a), (b) and (c) were taken under UV excitation.

The appearance of a green fluorescence, which was observed upon annealing of CNPz-OMeDiHex/PS films above T_g of PS is related to the molecular diffusion, which induced formation of crystalline CNPz-OMeDiHex aggregates. Fluorescence microscopy measurements confirmed aggregate formation by revealing homogeneous amorphous-like films before the treatment (see Fig. 4.22a) and micron-sized crystalline

aggregates just after 2 min of annealing (see Fig. 4.22b). Amorphous phase transformation to an ordered crystalline (glass-to-crystal mode) is known to be promoted by molecular diffusion in the bulk, i.e. bulk diffusion, which can be even further enhanced by a surface diffusion.[147,149] The size of the aggregates was found to increase with annealing time (Fig. 4.22b, c). Atomic force microscopy images clearly visualized elongated aggregate structures formed after annealing on the surface of PS films (Fig. 4.22d). Importantly, no aggregates were detected by fluorescence or atomic force microscopy in analogously prepared and annealed PS films doped with CNPz-OMeDiHex-2. This result is in agreement with the unchanged emission properties for CNPz-OMeDiHex-2 after annealing, which signify resistance of the extended backbone molecules to aggregation.

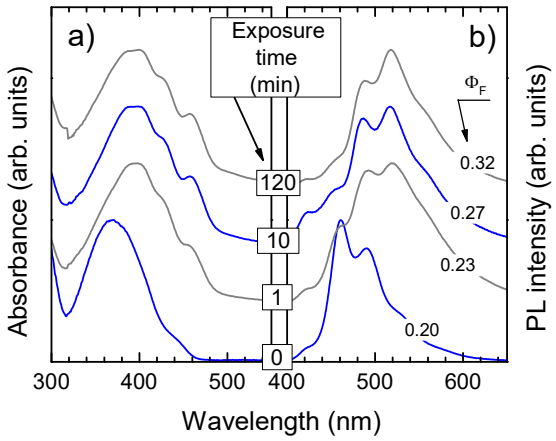

Fig. 4.23. Normalized absorption (a) and fluorescence (b) spectra of PS films doped with 5 wt % of CNPz-OMeDiHex as a function of exposure time to THF vapour. Spectra are arbitrarily shifted for clarity. Φ_F values are indicated.

Diffusion-induced molecular aggregation mechanism was also proved to work in the films exposed to solvent vapour [157], therefore this type of stimulus was also attempted for the PDACN-doped PS films. CNPz-OMeDiHex-doped PS films exposed to THF vapour showed similar optical response as upon annealing, i.e, featureless absorption spectrum became structured (Fig. 4.23) and fluorescence maximum exhibited a redshift of 60 nm just after 1 min exposure to THF vapour. Obviously, fast

solubilization of PS host promoted the diffusion of CNPz-OMeDiHex molecules causing formation of crystalline aggregates. Further treatment of the films by THF vapour resulted in the enhanced intensity of fluorescence peak at 520 nm. A minute-time response to THF vapour stimulus via change in the emission colour (from blue to green) of CNPz-OMeDiHex implies potential of the doped PS films in organic vapour sensing application.

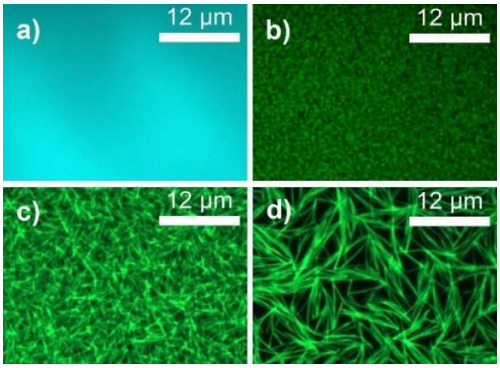

Fig. 4.24. Fluorescence microscopy images of the PS films doped with 5 wt % of CNPz-OMeDiHex and exposed to THF vapour for 0 (a), 1 (b), 10 (c) and 120 min (d). Images were taken under UV excitation.

The size of the formed CNPz-OMeDiHex aggregates increased rapidly with the exposure time to THF vapour as confirmed by fluorescence microscopy (Fig. 4.24). The obtained microscopy images indicated formation of nano-sized aggregates already after 1 min exposure to organic solvent vapour and dramatic enlargement of their size to tens of microns with further continuing treatment. The enlargement is attributed to deeper penetration of THF vapour over time, which triggers more molecules to aggregate. This suggests that reduction of the film thickness should give stronger and faster optical response of CNPz-OMeDiHex-doped polymer films to organic solvent vapour.

As expected, the morphology of CNPz-OMeDiHex aggregates formed by diffusion-induced process was also found to be crystalline. This was proved by polarized optical microscopy measurements, which

revealed nicely discernible aggregates under both parallel and crossed polarizers, thus implying their birefringence and hence crystallinity. In spite of the crystalline aggregates formed, Φ_F values of the annealed films (23%) were found to be very similar to those of untreated films. In contrast, a noticeable (1.5-fold) enhancement of Φ_F (up to 32%) was observed upon exposure of the films to THF vapour (Fig. 4.23b). The enhancement was evidently related to the greater dominance of the green fluorescence band peaking at 520 nm and attributed to aggregates (Figures 4.21b and 4.23b). To justify almost unchanged Φ_F after the annealing and rather distinct Φ_F enhancement after THF vapour treatment, excited state relaxation dynamics of the films was investigated. Excited state decay transients of the treated as well as untreated PS films doped with 5 wt % of CNPz-OMeDiHex are displayed in Fig. 4.25. The transients were fairly well described by employing

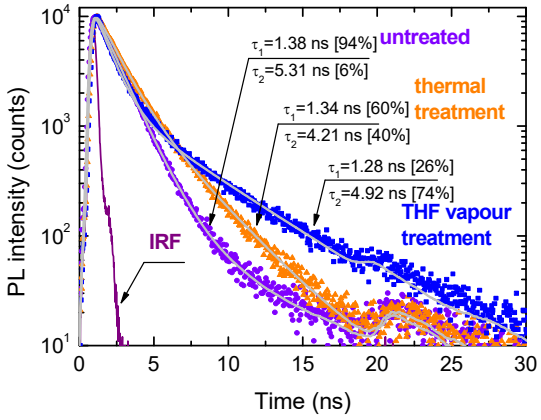

Fig. 4.25. Fluorescence transients of PS films doped with 5 wt % of CNPz-OMeDiHex before treatment (circles), after annealing at 110 °C for 4 h (triangles) and after exposure to THF vapour for 2 h (squares). Fluorescence lifetimes and fractional intensities (in the brackets) are indicated. IRF, instrument response function.

double-exponential decay model yielding two decay components with different fractional intensities. The fractional intensities (indicated in the brackets of Fig. 4.25) implied different contributions of each component to

the overall decay profile. The fluorescence transient of the untreated PS film exhibited almost single exponential decay profile with the fractional intensity of the dominant decay component (τ_1) well exceeding 90%. Since the untreated PS film was verified to contain mainly weakly interacting molecules, τ_1 of 1.4 ns corresponds to typical excitation deactivation in the single CNPz-OMeDiHex molecules. The slower decay component (τ_2 = 5.3 ns) is likely associated with minority crystalline aggregates amounting to only ~6% of CNPz-OMeDiHex load in PS matrix. The annealed or exposed to THF vapour PS films clearly showed double-exponential fluorescence decay profiles with the different contribution ratio of initial (faster) and later (slower) decay components. In all cases the initial decay component amounted to 1.3 ns, which corresponded to excitation relaxation in the weakly interacting molecules, whereas the slower component could be attributed to excitation decay in CNPz-OMeDiHex aggregates. Obviously, the contribution of the latter component was almost twice as large for the films treated with THF vapour for 2 hours as compared to those annealed for 4 hours. This result unambiguously indicates larger number of CNPz-OMeDiHex aggregates formed during the exposure to THF vapour than during the annealing, what is also confirmed by enhanced emission quantum yield and intensified green fluorescence. The enhanced optical response, and consequently, sensitivity to THF vapour stimulus can be explained by the enhanced softening of the PS matrix, which facilitates molecular diffusion and agglomeration into fluorescent crystalline aggregates.

To compare, neither THF vapour nor thermal treatment of PS films doped with extended backbone CNPz-OMeDiHex-2 molecules had noticeable impact on the spectral and transient fluorescence properties. This was evidently caused by the structural modification of the *p*-divinylbenzene backbone, i.e., extension of the backbone conjugation, resulting in molecular geometry changes, which precluded aggregation.

The latter findings implied potential of compound CNPz-OMeDiHex for the fluorescence sensing application, meanwhile ruled out utilization of phenylenediacetonitriles with extended backbone for this purpose. The suppression of aggregation for the compound bearing more planar and conjugated backbone CNPz-OMeDiHex-2 was in fact unexpected and counterintuitive, since commonly elongated and flatter molecules tend to enhance molecular aggregation.[158]

4.1.8 Summary

To summarize, phenylenediacetonitrile-based fluorescent nanoparticles with tunable morphology and emission properties were demonstrated. The tuning in the nanoparticles formed by simple precipitation technique was realized via adjusting solvent/non-solvent ratio in the mixture with the dissolved compound. Functionalization of the twisted phenylenediacetonitrile backbone with pyrazole and various peripheral alkoxy/cyclic moieties facilitated manipulation of packing morphology resulting in either crystalline nanostructures (in the case of long alkoxy side moieties) or amorphous spherical particles (in the case of shorter side moieties). Crystalline and amorphous phases were clearly discerned by their spectroscopic signatures, fluorescence quantum yield and lifetime behaviors and later confirmed by SEM and polarized optical microscopy. Of the tested compounds with various peripheral groups, the long and branchy dihexylmethoxy side groups were found to be optimal in achieving sharp morphology and emission tuning in the phenylenediacetonitrile nanoparticles. Particularly, the emission quantum yield could be tuned from 40% down to 2% and even up to 70% in correspondence with the morphology changes crystalline $\rightarrow$ amorphous $\rightarrow$ crystalline by adjusting THF/water ratio from 1/1 to 1/4 and to 1/9 in the mixture with the dissolved compound. Two

highly emissive states formed at THF/water ratio of 1/1 and 1/9 were associated with crystalline nanowire-like particles originating from different phenylenediacetonitrile polymorphs. THF vapor sensing via distinct change in emission colour or intensity was demonstrated implying potential application of the fluorescent phenylenediacetonitrile nanoparticles in volatile vapour sensors.

Additionally, easily solution-processed films based on phenylenediacetonitrile doped in polymer matrix (at the concentration of 5 wt %) have been utilized as fluorescence threshold temperature and volatile organic vapour sensors. A minute-time exposure to organic vapour or thermal stimulus was demonstrated to be sufficient to soften polymer host, and thus promote molecular diffusion and ordering into fluorescent crystalline nanoaggregates. The aggregates were shown to increase in size with the applied stimulus duration as verified by optical and atomic force microscopies. The aggregation triggered an emergence of the redshifted emission band causing the pronounced change in fluorescence colour (from blue to green), which was easily detectable by the naked eye. Moreover, as an additional benefit of utilization of AIEE compound, the diffusion-induced crystallization was accompanied by the enhanced emission intensity (at least in the case of THF vapour stimulus) resulting in a further increased detection sensitivity of the applied stimulus. The phenylenediacetonitrile compound featuring reduced conjugation was determined to be advantageous over the extended-backbone compound because of the stronger twisted backbone, which along with dihexyl-type of side-groups facilitated molecular arrangement into crystalline (highly emissive) aggregates. Relatively fast and distinct response to volatile organic solvent vapour and thermal stimuli implied potential for phenylenediacetonitrile-doped polymer films in fluorescence sensing.

4.2 Highly concentrated fluorene and benzo[c]fluorene films for low threshold light amplification

A series of low-molecular-weight compounds utilizing fluorene or benzo[c]fluorene core and bulky peripheral groups for prevention of concentration quenching were synthesized and investigated as potential lasing materials. The fluorene moieties, frequently used as the main building blocks for construction of organic lasers, were employed for their superior emission efficiency, large radiative decay rate, and thus, for high likelihood of low ASE threshold.[16,128] To enhance conjugation and rigidity of the compounds, the fluorene was fused with an additional benzene ring (so as to form benzo[c]fluorene – see Fig. 4.26 for chemical structures)

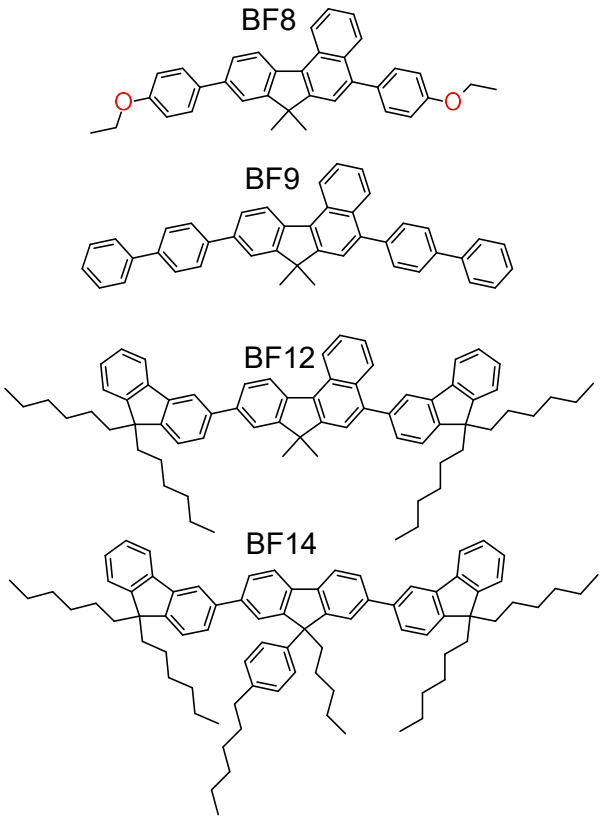

Fig. 4.26. Chemical structures of investigated benzo[c]fluorene and fluorene based compounds.

and used as the core, whereas to ensure weak concentration quenching the twisted molecular geometries resulting from sterically hindered

aromatic peripheral moieties decorated with branched alkyl chains (in some of the compounds) were employed. Benzofluorene derivatives were previously utilized in light-emitting devices as hosts or dopants mainly in spiro configuration,[159,160] however no data on the ASE properties of the compounds was reported yet. For comparison purposes, a similar fluorene-cored compound (BF14) was studied. The suitability of the benzo[c]fluorenes for light amplification was assessed by evaluating concentration quenching of spontaneous and amplified emission, by establishing relationship between pump thresholds of ASE and compound concentration as well as by quantifying radiative decay rates, photostability and carrier drift mobility.

4.2.1 Thermal properties

Thermal properties of the benzofluorenes were estimated by DSC. Fig. 4.27 illustrates first heating scans of DSC for all of the

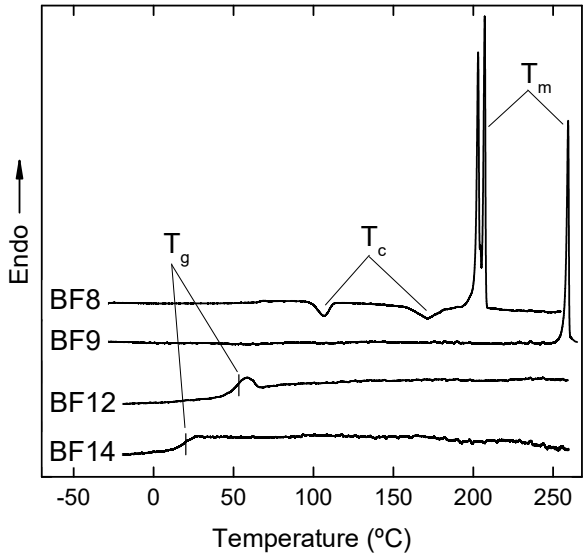

Fig. 4.27. DSC first-heating curves of the benzofluorenes BF8, BF9, BF12 and fluorene BF14.

compounds. Estimated glass transition (T_g), crystallization (T_c) and melting (T_m) temperatures of the compounds are summarized in Table 2.

Only two of the four compounds, i.e., benzofluorene BF12 and the fluorene BF14, both featuring bulky peripheral dihexylfluorenyl moieties showed glass transition. Lower T_g (20 °C) observed for BF14 as compared to that for BF12 (53 °C) is mainly due to the long aliphatic chains linked to the central fluorene moiety. Higher T_g of the benzfluorene compound BF12 implies higher thermal stability of the glassy state that is crucial for a device stability. No peaks due to crystallization or melting were detected during the first and second DSC scans of the compounds BF12 and BF14. Conversely, the benzofluorenes BF8 and BF9 with smaller phenyl-like peripheral moieties displayed crystallization/melting peaks and no traces of the glass transition (see Fig. 4.27 and Table 2). Two different crystallization and melting temperatures obtained for compound BF8 are assigned to different polymorphs. The amorphous nature of the compounds BF12 and BF14 accompanied with relatively low T_g can be attributed to loose molecular packing mainly due to the bulky dihexylfluorenyl peripheral groups.

Table 2. Thermal properties of the benzofluorenes BF8, BF9, BF12 and the fluorene based compound BF14.

Compound	T_g °C [a]	T_c °C [b]	T_m °C [c]
BF8	-	107, 172	203, 207
BF9	-	216	259
BF12	53	-	-
BF14	20	-	-

[a] Glass transition temperature. [b] Crystallization temperature. [c] Melting temperature.

4.2.2 Density functional theory calculations

Quantum chemical calculations of the benzofluorene derivatives in the gas phase were carried out using DFT at the B3LYP/6-31G* level as implemented in the Gaussian 09 software package. Geometry optimization revealed strongly twisted structures of the compounds in the ground state. The dihedral angles between the benzofluorene core and peripheral moieties linked to the 9th position of the core varied from 39° (for fluorenyl moiety) to 46° (for phenyl moiety), whereas the same angles for the side moieties linked to the 5th position of benzofluorene were substantially larger and varied from 53° (for dihexylfluorenyl moiety) to 69° (for phenyl moiety). The larger twisting angles were obviously induced by the naphthalene subunit of the benzofluorene core causing greater steric repulsion of the adjacent peripheral moieties. The calculated highest occupied molecular orbitals (HOMOs) and lowest unoccupied molecular orbitals (LUMOs) of the benzofluorenes BF8, BF9 were found to be localized primarily on the benzofluorene core and adjacent phenyl moieties (Fig. 4.28). Despite the utilization of conjugated fluorenyl side moieties in the compound BF12, the extension of molecular orbitals remained almost unchanged, *i.e.*, the orbitals remained localized mainly on the benzofluorene core and the nearest benzene rings of the peripheral moieties. The nearly unaltered configuration of molecular orbitals could be justified by the "angular" linking topology caused by the utilization of the 3rd linking position of the fluorenyl side moieties. Similar effect was observed for 3- and 3,6-substituted carbazole derivatives.[161,162] HOMO and LUMO of the fluorene only compound BF14 resembled those of BF12, however, the replacement of benzofluorene core with the fluorene obviously conditioned reduced conjugation (Fig. 4.28). Transition energies and oscillator strengths of the compounds were calculated using TD-DFT approach. The parameters involving two lowest singlet and triplet states

are summarized in Table 3. The calculations indicate the dominant $S_0 \rightarrow S_1$ transitions for all the compounds with oscillator strengths of about two orders of magnitude larger as those of $S_0 \rightarrow S_2$. The energies of the

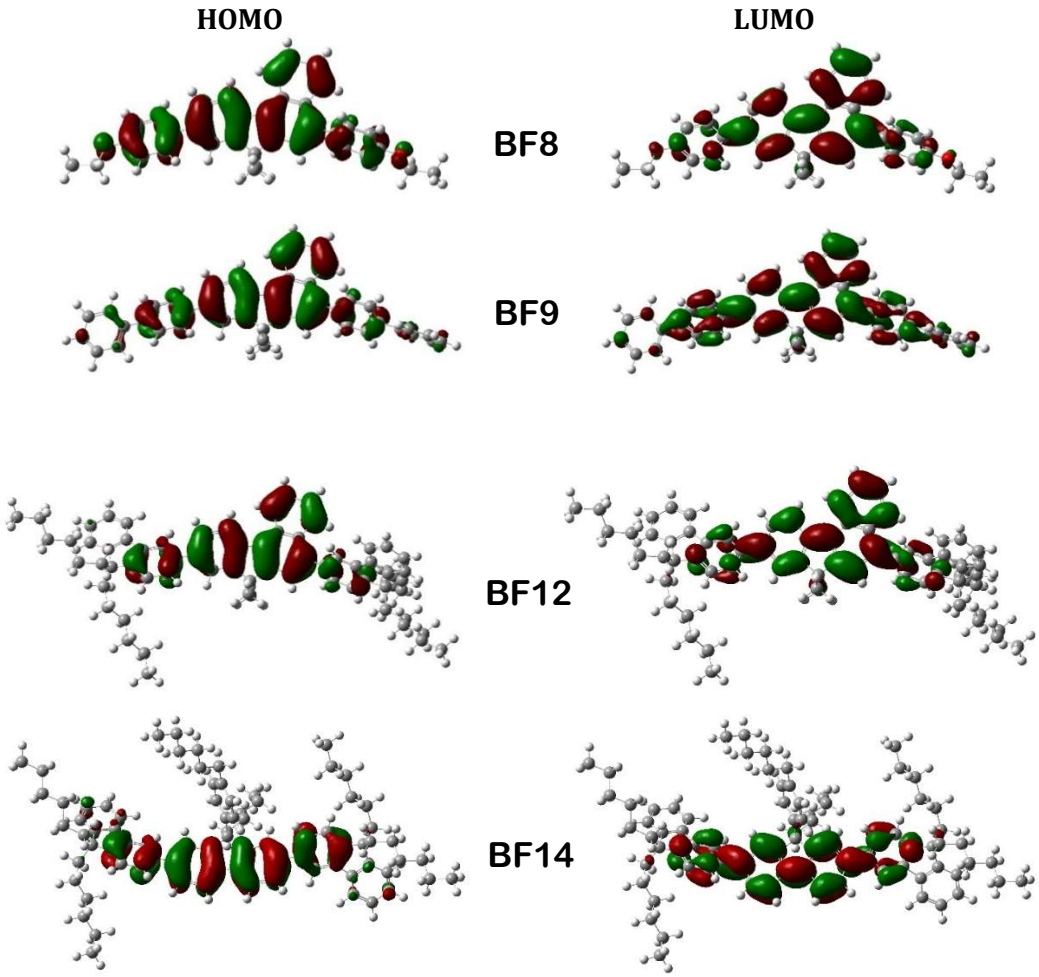

Fig. 4.28. HOMO and LUMO of the benzofluorene derivatives BF8, BF9, BF12 and BF14 calculated using the B3LYP/6-31G* basis set.

dominant transitions are located in the UV (3.46 – 3.67 eV). They are found within 20 meV for compounds BF8 and BF9, whereas the transition energy of compound BF12 bearing conjugated fluorenyl side moieties is by more than 100 meV lower as compared to those of BF8 and BF9. On the other hand, the lowest transition energy of BF14 bearing fluorene core is

~300 meV higher in respect to that of analogous benzofluorene compound BF12 due to the reduced conjugation of the core. The oscillator strengths of the lowest singlet transitions of compounds BF12 and BF14 are evidently larger as compared to those of BF8 and BF9 pointing out the importance of peripheral fluorenyl moieties. S_2 state for the benzofluorene compounds is found to be by 0.35 – 0.65 eV higher in energy, meanwhile T_1 by ~1.0 eV lower in energy in respect to S_1 state. The latter value indicates large singlet-triplet splitting in these molecules originating from excellent HOMO and LUMO overlap.[163]

Table 3. Calculated transition energies and oscillator strengths for the two lowest spin-allowed and spin-forbidden transitions of the benzofluorene compounds.

Compd.	$S_0 \rightarrow S_1$		$S_0 \rightarrow S_2$		$S_0 \rightarrow T_1$	$S_0 \rightarrow T_2$
	E (eV) [a]	f [b]	E (eV) [a]	f [b]	E (eV) [a]	E (eV) [a]
BF8	3.459	0.67	4.002	0.0033	2.365	3.272
BF9	3.443	0.81	4.088	0.0032	2.315	3.260
BF12	3.367	1.12	3.819	0.0173	2.281	2.927
BF14	3.674	1.66	4.021	0.0046	2.653	2.990

[a] Transition energy. [b] Oscillator strength.

4.2.3 Absorption and emission spectra

Absorption and fluorescence spectra of the dilute THF solutions and neat films of benzofluorene compounds are displayed in Fig. 4.29. The details of the optical properties are listed in Table 4. The studied benzofluorenes absorb in the UV spectral range (absorption maxima varies from 358 nm to 380 nm) while emit in the deep blue range (403 – 418 nm). Note a good agreement between experimentally determined $S_0 \rightarrow S_1$ absorption energies and the transition energies obtained from TD-DFT calculations. Obviously, the spectra of compounds are shifted to longer wavelengths as compared to those of single fluorene moiety as a

result of the enhanced conjugation of benzofluorene core. Indeed, the spectra of the fluorene-cored compound BF14 have peaks similar to those of single fluorene moiety. This is caused by the large twisting of sterically hindered peripheral groups and by utilization of the 3rd linking position of the fluorenyl side moieties, which disrupt the conjugation in BF14. The compounds BF8 and BF9 exhibit very similar shapes and spectral positions of absorption and fluorescence bands in solutions, whereas the compound BF12 shows almost 2-fold increase in absorbance and the redshift of absorption band (by 20 nm) as compared to BF8 and BF9. This increase in absorbance nicely correlates with a similar enhancement in oscillator strength revealed by TD-DFT calculations. These differences in BF12 arise due to the presence of more conjugated fluorenyl peripheral groups. Interestingly, the fluorescence band of benzofluorene BF12 has similar spectral location as that of BF8 and BF9 indicating minor role of dihexylfluorenyl peripheral groups in the excited state.

Fluorescence spectra of the neat films of benzofluorene derivatives are shifted to the long wavelengths as compared to those of dilute solutions due to the intermolecular interactions. The larger bathochromic shifts (~20 nm) and, consequently, stronger intermolecular coupling were observed for the compounds BF8 and BF9 featuring smaller phenyl-like peripheral groups as compared to those of BF12 and BF14. The latter compounds exhibited negligible bathochromic shifts amounting to only 3 nm as a result of the bulky dihexylfluorenyl peripheral groups acting as spacers, and thus, weakening intermolecular interaction.

Φ_F of the non-interacting benzofluorene molecules in dilute solutions was found to be rather high and ranged from 63% to 72%. Φ_F for the fluorene-cored BF14 was slightly smaller, 60% (see Table 4). Interestingly, high Φ_F (38 – 45%) was also observed for the neat films of benzofluorenes irrespectively of their peripheral moieties. Less than 2-

fold decrease of Φ_F in the neat films suggested weak concentration quenching, which was further explored in the next section.

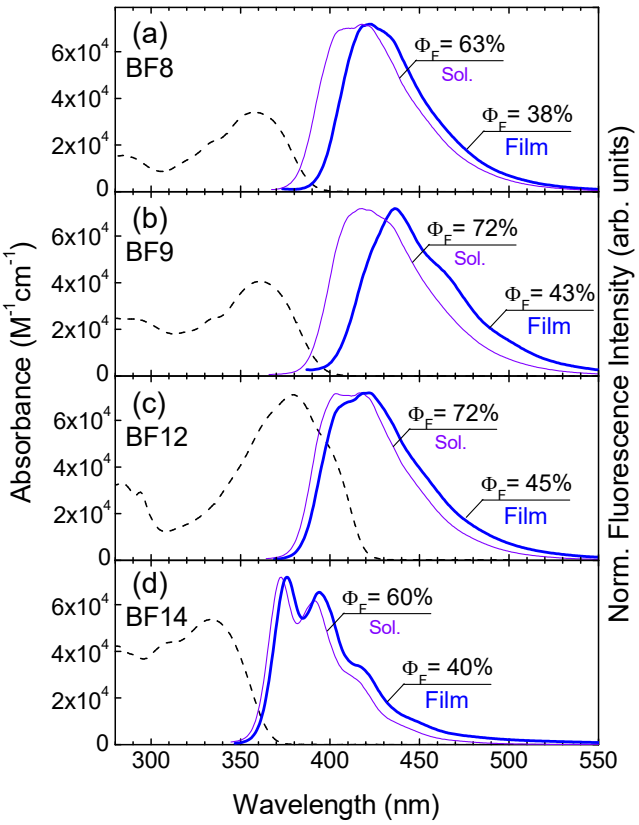

4.29. Absorption (dashed line) and fluorescence spectra of (a) BF8, (b) BF9, (c) BF12, and (d) BF14 in 10^{-5} M THF solutions (thin solid line) and neat films (thick solid line). Fluorescence quantum yields, indicated.

For light-emitting devices triplet energies of the compounds serving as guests or hosts are of crucial importance,[163,164] however they can be also important for lasing materials. Owing to the long lifetimes of the lowest-energy triplets, they are likely to be populated in electrically-driven lasers operating in continuous-wave, and thus may participate in the triplet absorption.[39,113] Triplet state energies (E_T) of the benzofluorenes were evaluated from the position of 0th vibronic band of the phosphorescence spectra measured at 20 K. E_T values of the compounds are listed in Table 4.

Table 4. Optical properties of the benzofluorene compounds in dilute (10^{-5} M) THF solutions and neat films. Phosphorescence data were obtained for the compounds dispersed in PS matrix at the concentration of 1 wt %.

	Dilute THF solution							Neat film			Phosphore sc.
	λ_{abs} (E_{S1}) [a]	ε [b]	λ_F [c]	Φ_F [d]	τ [e]	k_r [f]	k_{nr} [g]	λ_F [c]	Φ_F [d]	τ [e]	λ_{Ph} (E_{T1}) [h]
	nm (eV)	l mol^{-1} cm^{-1}	nm	%	ns	$\times 10^8$ s^{-1}	$\times 10^8$ s^{-1}	nm	%	ns	nm (eV)
BF8	358 (3.462)	34000	403 418	63	1.5	4.2	2.5	422	38	0.8 [64%] 2.6 [36%]	587 (2.112)
BF9	360 (3.443)	40600	418	72	1.1	6.5	2.5	436	43	0.5 [88%] 1.5 [12%]	589 (2.104)
BF12	380 (3.279)	71000	403 416	72	1.3	5.5	2.2	406 420	45	0.5 [93%] 2.3 [7%]	580 (2.137)
BF14	335 (3.700)	53600	373	60	0.9	6.7	4.4	376	40	0.4 [68%] 0.8 [29%] 5.3 [3%]	515 (2.407)

[a] Absorption band maximum. [b] Molar extinction coefficient. [c] Fluorescence band maximum. [d] Fluorescence quantum yield. [e] Excited state lifetime. [f] Radiative relaxation rate. [g] Nonradiative relaxation rate. [h] Phosphorescence band maximum at 20 K.

4.2.4 Excited state dynamics

Excited state relaxation dynamics of the benzofluorenes was assessed by measuring fluorescence transients of their dilute solutions and neat films (Fig. 4.30). The dilute solutions of BF8, BF9 and BF12 exhibited single exponential decay with a similar decay time constants (τ_F) of 1.1 – 1.5 ns, which are typical of organic fluorophores. Compound BF14 bearing fluorene core showed slightly shorter τ_F of 0.9 ns. Fluorescence transients of the neat films expressed clear multiexponential behavior with faster excited state relaxation occurring during the first 3-4 ns after excitation pulse and a slower relaxation at a later stage (ca. 4 ns after excitation). The multiexponential temporal profile accompanied by the redshifted fluorescence bands in the solid films indicated energy transfer arising via exciton hopping through the localized states in disordered media.[165] The fluorescence decay profiles were fitted by using two- or three-component exponential decay models to reveal the major component and its fractional intensity (see Table 4). The fractional

intensity of the component signifies its actual contribution to the overall excited-state decay and is indicated in the brackets next to the τ_F value. Evidently, the major contribution was afforded by the fast component with τ_F < 1.0 ns. τ_F of the component was roughly half as that obtained in solution and could be associated mainly with exciton migration and enhanced nonradiative relaxation in the solid phase at the early decay stage.[166,167] This was also supported by the reduced Φ_F in the neat films amounting to < 50% and signifying the nonradiative decay channel as the governing one. Meanwhile, the slower decay component could be attributed to stronger localized excitons capable of evading fast nonradiative decay. Generally, more pronounced exciton migration, and thus migration-induced fluorescence quenching accompanied by the excited state lifetime shortening is expected for more ordered films with the tighter molecular packing.[168] Therefore, bulky peripheral groups such as dihexylfluorenyl moieties in the benzofluorene BF12 and the fluorene-cored BF14 should cause much less ordered, *i.e*, amorphous films as compared to more dense films of BF8 and BF9. However, no significant differences among the benzofluorene compounds in Φ_F quenching or shortening of the major component of τ_F in the neat films were observed (see Table 4). Calculations of radiative and nonradiative relaxation rates, k_r and k_{nr} respectively, by using the relations $k_r = \Phi_F/\tau$, $k_{nr} = (1 - \Phi_F)/\tau$ yielded similar k_{nr} of ~2.5×10^8 s^{-1} and only slightly different k_r [$(4.2 - 6.5)\times10^8$ s^{-1}] for benzofluorenes BF8, BF9 and BF12 in dilute solutions. For comparison, the fluorene-cored BF14 exhibited somewhat larger k_r, but also nearly twice as large k_{nr}. Large k_r is important for lasing materials as it allows attaining low ASE threshold.[165]

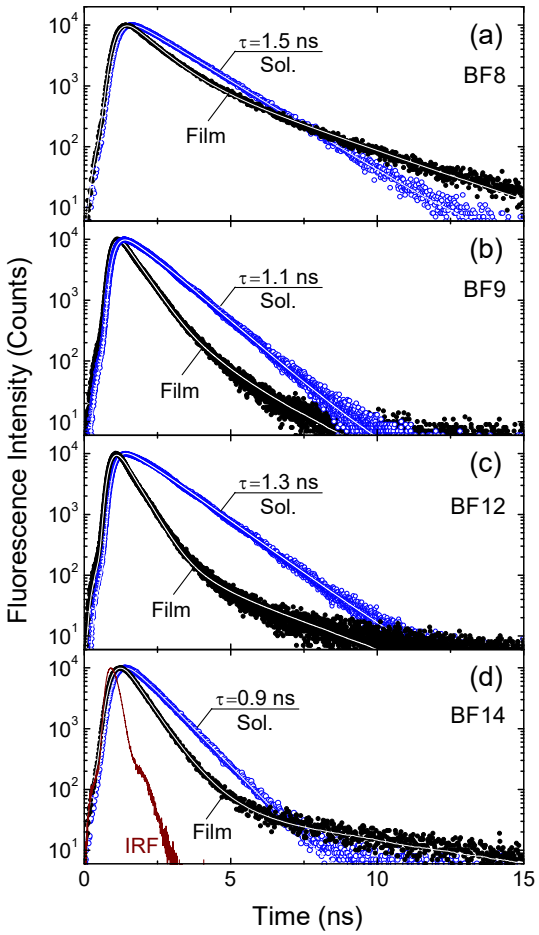

Fig. 4.30. Fluorescence transients of the benzofluorenes (a) BF8, (b) BF9, (c) BF12, and (d) BF14 in 10^{-5} M THF solutions (grey circles) and neat films (black points). Lines mark exponential or multiexponential fits to the experimental data. Instrument response function (IRF) and fluorescence lifetimes for solutions, indicated.

4.2.5 Concentration quenching

High radiative relaxation rates and emission efficiencies are essential for achieving low ASE threshold in lasing materials.[40] Preserving these properties at high chromophore concentration is just as important for realization of efficient laser.[23] The concentration quenching of the benzofluorene derivatives was investigated by evaluating Φ_F of the compounds dispersed in polystyrene matrix as a function of their concentration from 0.5 to 100 wt % (Fig. 4.31). At low concentrations in

PS matrix all the benzofluorene compounds exhibited similar Φ_F (70 – 80%), which were up to 10% higher as compared to those estimated in dilute solutions. The slight enlargement of Φ_F could be attributed to the suppressed intramolecular torsions in the environment of increased rigidity.[165] It is worth highlighting that increasing compound concentration up to 10 wt % in PS matrix had negligible influence on the fluorescence efficiency, whereas further increase of the concentration up to 100 wt % resulted in about 2-fold drop of Φ_F. Similar tendency was also obtained for average fluorescence lifetime ($<\tau>$) estimated independently from Φ_F (see Fig. 4.31). Roughly, similar behavior and drop of $<\tau>$ with increasing compound concentration were observed for all the benzofluorenes. The simultaneous reduction of both Φ_F and $<\tau>$ could only be justified by the enhanced nonradiative processes originating from increased intermolecular coupling at high compound concentration. Enhanced intermolecular coupling facilitates exciton migration to the quenching (or so-called "dark") states consequently promoting the nonradiative deactivation. The "dark" states are commonly associated with non-emissive molecular aggregates, however, even in the absence of aggregation, *e.g.* in purely amorphous films, excimer species, intrinsic defects, distortions or other non-intentionally added quenching defects such as impurity traps might also serve as the "dark" states. Essentially, the concentration quenching effect of BF8, BF9, BF12, and BF14 is weak, and moreover, the degree of quenching does not depend notably on peripheral groups. For comparison, well-known bay-substituted perylene diimide dyes exhibited huge concentration quenching resulting in more than 10-fold reduction of Φ_F already at the concentration of 10 wt %.[59] The 10-fold drop of Φ_F with increasing compound percentage in PS up to 100 wt % was obtained for triphenylamine derivatives[168] and also for diphenylanthracene-based compounds.[64]

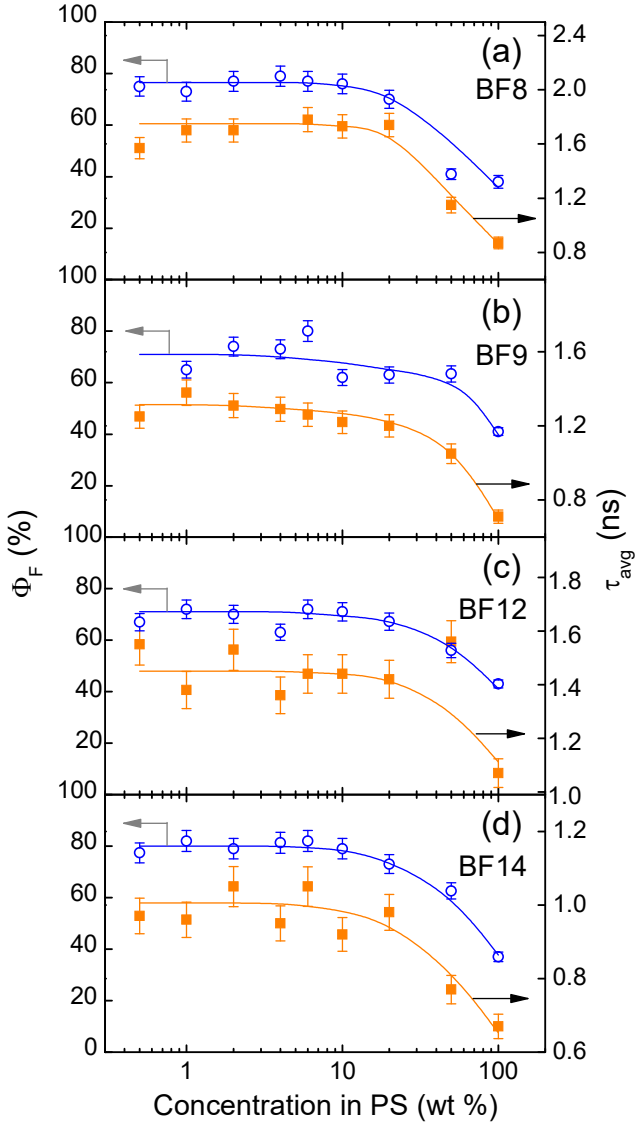

Fig. 4.31. Fluorescence quantum yields (grey circles) and average fluorescence lifetimes (black rectangles) of the benzofluorenes (a) BF8, (b) BF9, (c) BF12, and the reference compound (d) BF14 as a function of their concentration in PS matrix.

The weak quenching of the studied benzofluorene compounds can be attributed to their twisted molecular geometries resulting from singly-bridged multi-fragment structures and to a lesser extent to the volume of peripheral moieties.

4.2.6 Amplified spontaneous emission

The potential of benzofluorenes for light amplification was tested by carrying out ASE measurements in one of the simplest mirrorless configurations, the so-called thin excitation stripe configuration. This is by far the most appropriate technique used to compare the performance of different materials for lasing application excluding resonant cavity effects, *i.e.* external resonators or distributed feedback gratings.[115] The technique is based on the excitation of slab waveguide samples with a pulsed laser stripe and registration of emission spectra from a sample edge.[136] Essentially, spontaneous emission travelling along the excitation path (stripe) is amplified by the stimulated transitions causing spectral narrowing of the emission above certain pump intensity referred to as ASE threshold (I_{th}^{ASE}).

ASE of the benzofluorenes was investigated as a function of their concentration in PS matrix to reveal the impact of intermolecular coupling, possible aggregate formation on the ASE performance. Importantly, all the compounds expressed ASE in their neat films, which is often difficult to achieve due to the strong concentration quenching of emission.[26] Fig. 4.32 shows excitation power dynamics of the edge emission spectra of the neat films of BF8, BF9, BF12 and BF14. At the lowest pump density all the compounds demonstrate broad spontaneous emission band, which spectrally narrows with the onset of ASE. The ASE peaks appear redshifted by 5 – 20 nm in respect to the spontaneous band maxima due to the absorptive losses at the short-wavelength slope of emission spectra (reabsorption effect). The sudden emission band narrowing with the increasing pump is accompanied by an abrupt change in the emission intensity from linear to superlinear at I_{th}^{ASE} (see insets of Fig. 4.32). The notable deviation from the linear to sublinear dependence of emission intensity *vs* pump was observed for BF9 below I_{th}^{ASE}. This was

caused by the enormously high I_{th}^{ASE} (200 kW/cm²) obtained for the neat film of BF9, which implied utilization of high pump fluences in ASE measurements eventually resulting in gradual material and emission degradation.

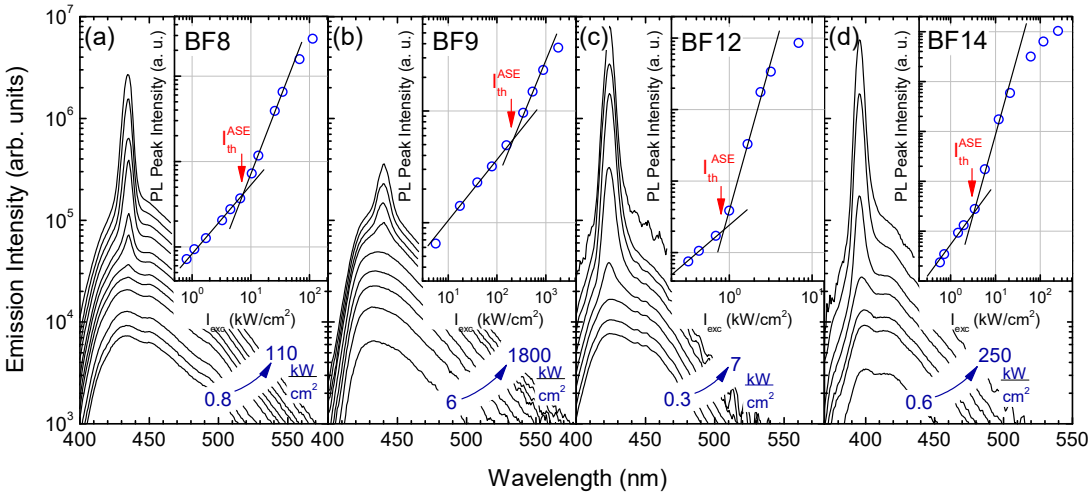

Fig. 4.32. Excitation power dependence of the edge emission spectra of the neat films of benzofluorenes (a) BF8, (b) BF9, (c) BF12, and the reference compound (d) BF14. Insets show emission peak intensity *vs* excitation power density (I_{exc}). Lines are guides for the eye. Arrows indicate onset of ASE.

Concentration dependence of I_{th}^{ASE} for the studied benzofluorenes and the BF14 compound dispersed in PS matrix are illustrated in Fig. 4.33a. Elucidation of this dependence is crucial for determination of the optimal compound concentration for laser operation.[169,170] Moreover, I_{th}^{ASE} is one of the key parameters describing the feasibility of the material to be employed in lasing systems as an active medium. Generally, the benzofluorenes BF8, BF9 and BF12 show different behavior of I_{th}^{ASE} with increasing concentration. I_{th}^{ASE} decreases for all the compounds up to the concentration of 5 wt %. Further on, it continues to decrease for BF12 as well as for BF14 up to the highest concentrations, whereas for the compounds BF8 and BF9, the saturation and even steep increase of I_{th}^{ASE}, respectively, is observed just above 5 wt %.

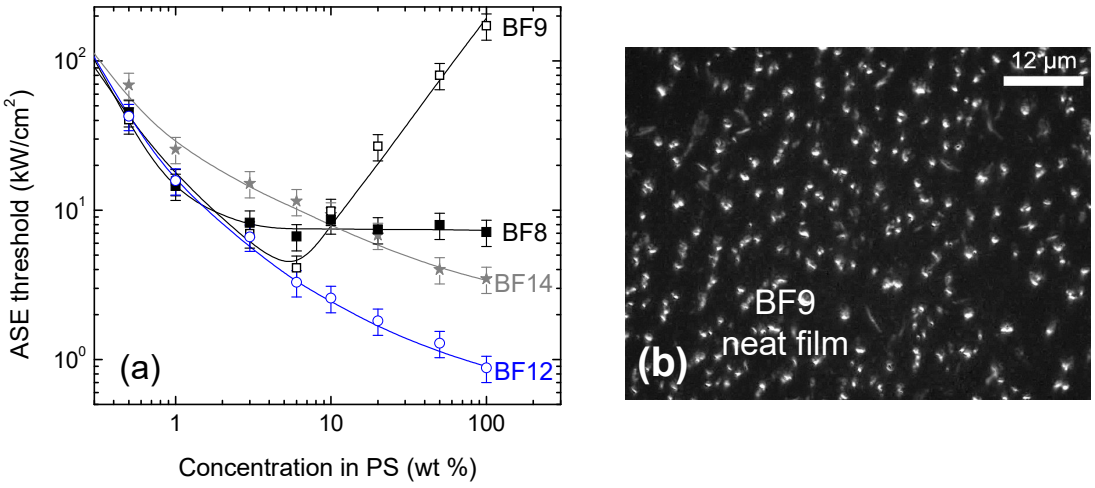

Fig. 4.33. (a) ASE threshold as a function of compound BF8, BF9, BF12 and BF14 concentration in a PS matrix. Lines are guides for the eye. (b) Dark field optical image of the neat film of BF9.

The decrease of I_{th}^{ASE} with increasing concentration is related to the reduction of optical losses due to the reduced intermolecular distances. Higher compound concentration in PS matrix facilitates attaining of critical exciton density required to achieve I_{th}^{ASE}. Note that at low concentrations (<5 wt %) the studied benzofluorenes exhibit similar I_{th}^{ASE}. This can be explained by the inverse proportionality of I_{th}^{ASE} to Einstein's coefficient B, which directly relates to k_r as $B \propto (c^3/8\pi h\nu_0^3)k_r$, where h is Planck's constant, ν_0 is the frequency of light, and c is the velocity of light.[171] The insignificant differences in k_r obtained for the benzofluorenes BF8, BF9 and BF12 in dilute solutions (see Table 4) therefore correspond to small variations in I_{th}^{ASE}. Taking into account that k_r values were estimated for the dilute solutions, the similarity of I_{th}^{ASE} pertains only to low compound concentrations.

For compounds BF12 and BF14 the lowest I_{th}^{ASE} was attained at their highest concentrations in PS matrix, *i.e.*, in their neat films (see Fig. 4.33a). In contrast, for BF9 the lowest I_{th}^{ASE} was achieved at the concentration of ~6 wt %. However, the steep increase of I_{th}^{ASE} with

further increasing concentration could not be related to concentration quenching, because it was found to be weak and similar for all the benzofluorenes studied (see Fig. 4.31). Examination of the PS films with high BF9 concentration under optical microscope in the dark field enabled to discern (sub)micron size aggregates, which are displayed in Fig. 4.33b for the neat film. The aggregates had a tendency to increase in size with increasing concentration, and obviously, were a prime cause of drastically enlarged I_{th}^{ASE} due to the increased scattering of directional ASE. Aggregation-induced absorption in the spectral region of the amplified emission might also contribute to the enlarged I_{th}^{ASE}. However in this case it can be ruled out, since all the benzofluorenes demonstrate similar concentration quenching (see Fig. 5) and similar Φ_F of the neat films signifying negligible role of aggregates in emission quenching.

Similar aggregate formation, although of greatly reduced extent was identified in the PS films of BF8 at high concentrations. Most likely, the saturation of I_{th}^{ASE} above ~6 wt % for BF8 was caused by the competing processes of reduced intermolecular separation (conditioning reduced optical losses) and aggregation-induced scattering of amplified emission (conditioning increased losses). No traces of aggregation were detected in the neat films of BF12 and BF14 verifying their amorphous nature as revealed from DSC measurements (see Fig. 4.27). The amorphous morphology of the neat films of compounds BF12 and BF14 was also confirmed by atomic force microscopy. Evidently, the bulky dihexylfluorenyl peripheral moieties in the compounds BF12 and BF14, conversely to the smaller phenyl-like moieties, are able to suppress aggregation, and hence, aggregation-induced light scattering.

The lowest ASE threshold obtained in the neat film of benzofluorene BF12 (I_{th}^{ASE} = 900 W/cm^2) indicates advantage over analogous fluorene-cored compound BF14 demonstrating somewhat higher I_{th}^{ASE} (3 kW/cm^2) in the neat film. This can be attributed partly to

the larger extinction coefficient of BF12 assuming similar packing density of the neat films (see Table 4). I_{th}^{ASE} value of 900 W/cm^2 (4.5 μJ/cm^2) achieved for the benzofluorene film in air was found to be comparable or lower than, *e.g.* that reported for polyspirobifluorenes (4.4 μJ/cm^2)[172], oligofluorenes (9 - 16 μJ/cm^2),[173,174] various bisfluorene-cored dendrimers (16 – 50 μJ/cm^2),[175] etc., measured under similar nanosecond excitation in a mirrorless configuration.

Table 5. Amplified spontaneous emission properties of the benzofluorene compounds.

	λ_{ASE} [a]	I_{th}^{ASE} [b]	$t_{1/2}^{ASE}$ [c]
Compound	nm	kW/cm^2	pump pulses
BF8	435	8 (neat film)	8×10^3 @16 kW/cm^2
BF9	440	4 (6 wt % in PS)	9×10^3 @8 kW/cm^2
BF12	424	0.9 (neat film)	20×10^3 @1.8 kW/cm^2
BF14	395	3 (neat film)	5×10^3 @6 kW/cm^2

[a] ASE band maximum. [b] ASE threshold. [c] Photostability lifetime.

Still, this I_{th}^{ASE} value was an order of magnitude higher as compared to possibly the lowest ever reported I_{th}^{ASE} value (0.43 μJ/cm^2) attained in the neat film of 2,7-bis[4-(N-carbazole)phenylvinyl]-9,9′-spirobifluorene.[128] Note however that the record energy threshold value was obtained by using the shorter pulse (500 ps) excitation source, which implied nearly the same threshold density value for power (860 W/cm^2) as that achieved here in benzofluorene BF12. Moreover, unlike in our case, where ASE measurements were performed in air, the record value was obtained in a nitrogen atmosphere with the photooxidative degradation eliminated. Taking this into account, such low ASE threshold achieved in the neat film prepared from solution by spin-coating in air shows great potential for benzofluorene-cored molecular glasses as active media for lasing applications.

4.2.7 Photostability and carrier drift mobility

Photostability is important for lasing materials for it allows maintaining sufficiently high photon flux in operating conditions. The photostability of the benzofluorene compounds was assessed by monitoring ASE intensity as a function of the number of pump pulses at the constant pump density in an ambient atmosphere (Fig. 4.34). The compound concentrations in PS matrix resulting in the lowest I_{th}^{ASE} were chosen for these measurements. To approach the real working conditions of a laser device, the measurements were performed at the pump density equal to $2 \times I_{th}^{ASE}$. All the studied compounds exhibited drop in the total ASE output with the number of pump pulses indicating material degradation. The degradation is commonly associated with the photooxidation, *i.e.*, creation of carbonyl defects (also known as keto defects in fluorene-based compounds)[175] in the active medium leading to a quenching of emission as well as the optical loss at the pump wavelengths.[113] The photostability of the benzofluorenes was compared by comparing their stability lifetimes ($t_{1/2}^{ASE}$) defined as the number of pump pulses resulting in a drop of ASE intensity to half its initial value (see Table 5). The estimated $t_{1/2}^{ASE}$ for the benzofluorenes BF8, BF9 and BF12 varied from 8×10^3 to 20×10^3 pulses and was comparable to the lifetimes of other small-molecules or polymers evaluated under similar conditions (in nanosecond/picosecond pulse regime).[59]

The largest $t_{1/2}^{ASE}$ of 20×10^3 pump pulses, and thus the highest photostability was determined for the neat film of benzofluorene BF12. This is mainly because of the significantly reduced ASE threshold as compared to that of the rest compounds (see Table 5). The fluorene-cored compound BF14 exhibited the worst photostability with $t_{1/2}^{ASE}$ of 5×10^3 pulses. Latter result may be caused by high excitation photon energy due to the shorter conjugation of BF14 and low glass transition temperature.

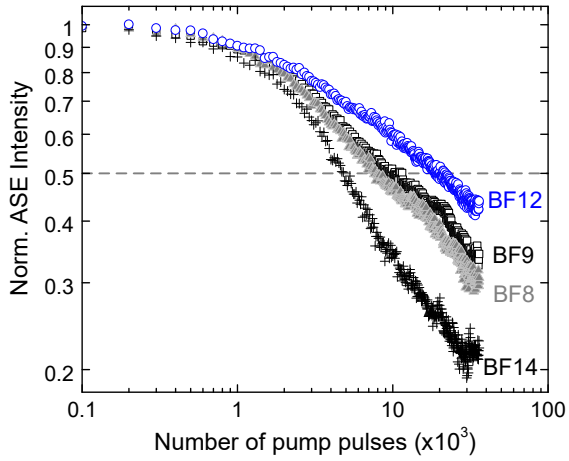

Fig. 4.34. Normalized ASE intensity dependence on the number of pump pulses for benzofluorenes BF8, BF9, BF12, and the reference BF14 dispersed in PS matrix at the concentration corresponding to the lowest I_{th}^{ASE}, *i.e.*, 100, 6, 100 and 100 wt%, respectively. The excitation power densities were $2 \times I_{th}^{ASE}$, *i.e.*, 16, 8, 1.8 and 6 kW/cm^2, respectively.

Carrier drift mobilities of the wet-casted neat films of the investigated compounds were measured by xerographic time-of-light (XTOF) technique. Unfortunately, the XTOF measurements for compound **BF9** were impossible as the film readily crystallized upon casting. The neat film of the reference **BF14** featuring low T_g (20 °C) was by far too soft resulting in film thickness changes under applied electric field making the measurements unreliable. The benzofluorene **BF8** exhibited rather high hole drift mobility (μ_h) of 2×10^{-3} cm^2/Vs at an electric field of 0.5 MV/cm, whereas **BF12** expressed only moderate μ_h (8×10^{-5} cm^2/Vs) at the same conditions. Significantly lower μ_h estimated for the neat film of **BF12** is attributed to a loose molecular packing caused by the bulky dihexylfluorenyl peripheral groups. Thus, although the bulky groups at periphery ensure formation of aggregate-free amorphous films with ASE scattering due to aggregates avoided, and hence ASE threshold reduced, they obviously deteriorate carrier drift mobility hampering material utilization in organic lasers. On the other hand, the more compact ethoxyphenyl peripheral moieties in **BF8**

facilitate denser packing thereby enhancing carrier transport. However, the dense packing facilitates formation of aggregates in the films, which act as ASE scatterers causing increased ASE threshold. This implies a certain trade-off between ASE threshold and charge transport properties for lasing materials employed as neat films.

4.2.8 Impact of the fluorene sidegroup linking position

Inspired by promising light amplification properties of fluorene and benzo[c]fluorene compounds bearing fluorene sidegroups linked at 3rd position (compounds BF12 and BF14) new analogous compounds with fluorene moieties linked at 2nd position were designed (see insets in Fig. 4.35). Such linking topology is expected to enhance conjugation, k_r, Φ_F values and thus, result in even lower I_{th}^{ASE}. Fluorene sidegroups were decorated with short ethyl (BF12-et and BF14-et) and long hexyl (BF12-hex and BF14-hex) sidegroups to evaluate their impact to the packing morphology and photophysical properties in the highly concentrated films.

Fig. 4.35 shows spontaneous emission and ASE spectra of the oligomers in a rigid PS matrix at a concentration of 10 wt %. The employed concentration is sufficiently low for these compounds to neglect intermolecular interactions. Clearly, at such low concentrations different-length alkyl moieties (ethyl or hexyl) play no role in the emission, since they are not conjugated. The spontaneous emission spectra are broad and exhibit characteristic vibronic structure. As expected both fluorene and benzofluorene core bearing oligomers show redshifted fluorescence spectra as compared with their analogues BF12 and BF14 (see Fig. 4.29). The spectra of BF12-et and BF12-hex oligomers are shifted by 25 nm to longer wavelengths as compared to those of BF14-et and BF14-hex as a result of enhanced conjugation of benzofluorene core. Much narrower ASE

bands obtained at high pumps emerge at the 0-1 vibronic transition of spontaneous emission, which is typical for a quasi-four-level vibronic systems.[16]

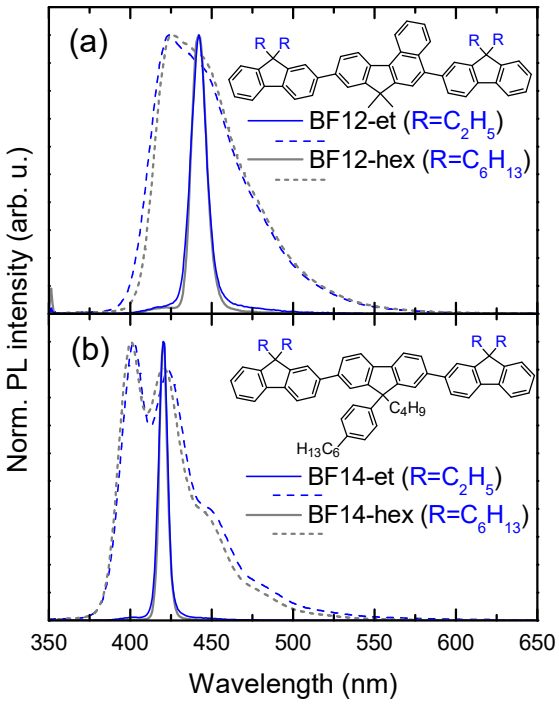

Fig. 4.35. Spontaneous (dashed line) and amplified (solid line) emission spectra of the benzofluorene-cored (a) and fluorene-cored (b) oligomers in PS matrix at 10 wt % concentration. Insets: chemical structure of the oligomers.

Since high chromophore concentration is essential for attaining high carrier mobility, and ultimately, for efficient lasing,[23] low emission quenching and high k_r must be ensured at such conditions. To this end, concentration quenching of spontaneous emission was evaluated by dispersing fluorene- and benzofluorene-cored oligomers in an inert PS matrix and estimating Φ_F dynamics *vs* molecule concentration in the range of 0.5 – 100 wt % (Fig. 4.36). Φ_F values in the Fig. 4.36 are accompanied by τ data estimated from fluorescence transients measured at different oligomer concentrations in PS. Interestingly at low concentrations, all the compounds demonstrated higher Φ_F values as compared with their analogues with linking topology at 3rd position. Fluorene-cored oligomers

expressed somewhat higher Φ_F (90%) and shorter τ (0.7 ns) as compared to these values (Φ_F = 78% and τ = 1.0 ns) for benzofluorene-cored compounds. This implies significantly larger k_r (1.3×10^9 s^{-1}) in fluorene-cored oligomers BF14-et and BF14-hex in respect to that (7.8×10^8 s^{-1}) in BF12-et and BF12-hex making the former oligomers more promising for light amplification. It is worth noting that increasing compound concentration up to 10 wt % (for benzofluorenes) or 20 wt % (for fluorenes) had negligible influence on the Φ_F and τ, whereas further increase of the concentration up to 100 wt % resulted in roughly 2-fold drop of these values. Only 2-fold reduction of Φ_F and τ in the neat films is caused by enhanced nonradiative relaxation induced by exciton migration and infers rather weak emission quenching and thereby weak intermolecular coupling. This was also confirmed by the small red shift of emission spectra as well as single exponential decay of the transients preserved up to the highest oligomer concentrations in PS. A similar quenching efficiency observed for oligomers BF12-et(BF14-et) and BF12-hex(BF14-hex) with increasing concentration indicates minor influence of the length of alkyl moieties attached to the peripheral fluorenyl groups. Meanwhile the onset of quenching at higher concentrations (>20 wt %) for fluorene-cored oligomers is due to the longer alkyl moieties attached to the core. The longer alkyls result in a less dense intermolecular packing, and therefore, are more efficient in suppressing concentration effects. Generally, the weak concentration quenching observed for the studied oligomers can be also attributed to their twisted molecular geometries resulting from significant steric hindrance of the neighbouring bulky fragments as confirmed by the density functional theory calculations. The calculations revealed large dihedral angles (up to 59°) between the core and peripheral fragments.

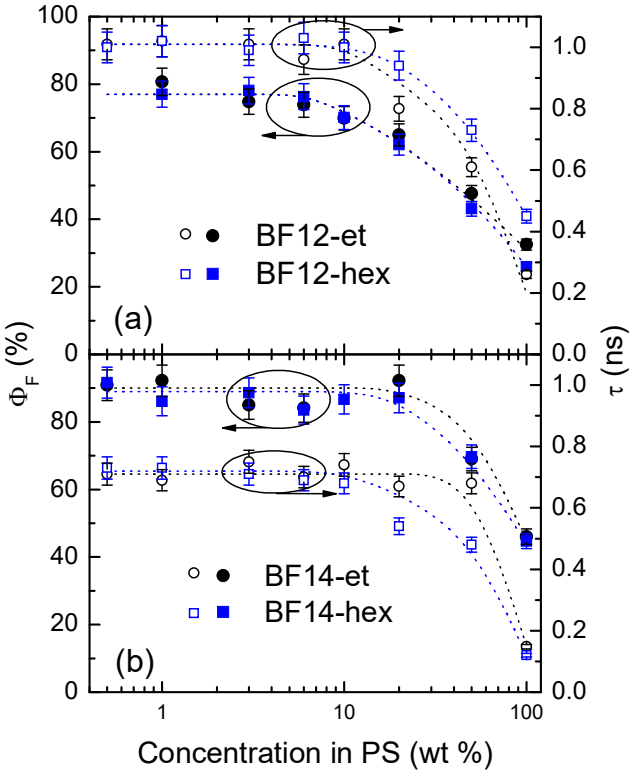

Fig. 4.36. Fluorescence quantum yields (solid points) and average fluorescence lifetimes (empty points) of the benzofluorene-cored (a) and fluorene-cored (b) oligomers as a function of their concentration in PS matrix.

The impact of intermolecular coupling on the amplified emission of oligomers was investigated by evaluating I_{th}^{ASE} as a function of their concentration in PS matrix. The sudden emission band narrowing with the increasing pump, which was accompanied by an abrupt change in the emission intensity from linear to superlinear (inset of Fig. 4.37a) served as a signature of I_{th}^{ASE}. All the studied oligomers exhibited continuous decrease of I_{th}^{ASE} with increasing concentration up to a certain point (optimal concentration) and further increase of I_{th}^{ASE} after this point (Fig. 4.37b). The initial decrease of I_{th}^{ASE} is related to the reduction of absorptive optical losses due to the reduced intermolecular distances. In fact, compensation for the optical losses by expressing I_{th}^{ASE} in the units of absorbed (not incident) power density should result in the independence of I_{th}^{ASE} as a function of compound concentration up to the point where

intermolecular interactions are still negligible. However, the later increase of I_{th}^{ASE} occurring above the optimal concentration of 6 - 10 wt % for BF-et and BF-hex, and 10 - 50 wt % for F-hex and F-et is determined by the concentration quenching effect as discussed above. Evidently, the smaller concentration quenching obtained for fluorene-cored oligomers (see Fig. 4.26) favored higher optimal concentrations for ASE. Furthermore, owing to the larger k_r fluorene-cored oligomers exhibited down to one order of magnitude lower ASE thresholds as compared to those (~3 kW/cm²) of benzofluorene counterparts. The lowest I_{th}^{ASE} of 300 W/cm² (1.5 μJ/cm²) was attained for the fluorene-cored oligomer BF14-et at the concentration of 50 wt % in PS. Remarkably, this is one of the lowest ASE thresholds reported for solution-processed amorphous films prepared and measured in ambient conditions under nanosecond excitation.[173–175] The optimal concentration (50 wt %) is also very high as compared to that found for other lasing materials. It emphasizes strongly suppressed concentration quenching for BF14-et oligomer.

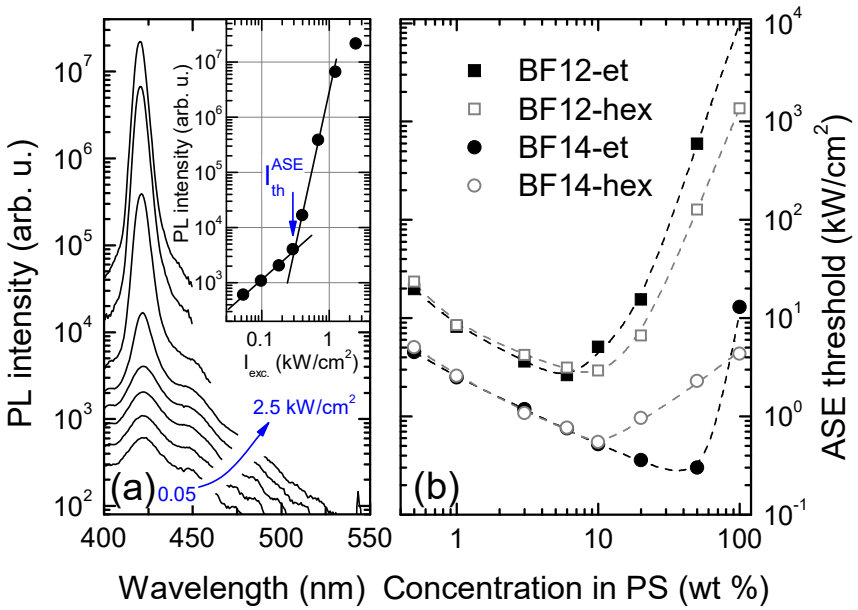

Fig. 4.37. (a) Excitation power dependence of the edge emission spectra of BF14-et in PS matrix at 50 wt % concentration. Inset: emission peak intensity *vs* excitation power density (I_{exc}), arrow indicates onset of ASE. (b) ASE threshold as a function of oligomer concentration in PS matrix. Lines are guides for the eye.

The PS films containing optimal oligomer concentration were pumped at different excitation densities with the pump length gradually increasing from 0 to 0.2 cm to determine their optical gain. The emission intensity, $I(\lambda)$, recorded as a function of the stripe length, l, was modeled using the Eq. (1) to estimate the net optical gain coefficient, $g(\lambda)$,

$$I(\lambda, l) = \frac{AI_S(\lambda,l)}{g(\lambda)}\{\exp[g(\lambda)l] - 1\}, \quad (1)$$

where $AI_s(\lambda, l)$ defines spontaneous emission proportional to the pumping intensity. The modeling of $I(\lambda)$ was carried out at the wavelength corresponding to maximum of ASE intensity. The fitted data for BF12-hex

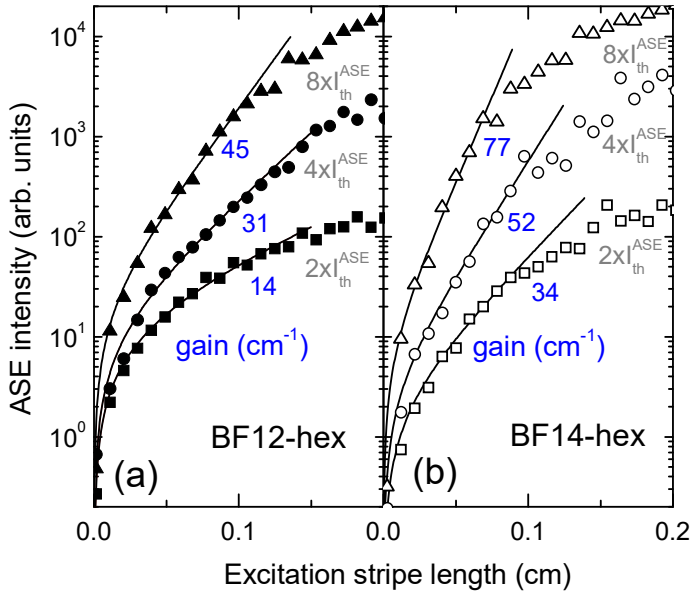

Fig. 4.38. ASE peak intensity as a function of excitation stripe length for BF12-hex (a) and BF14-hex (b) in PS matrix at 10 wt % concentration. Pump densities ($2\times I_{th}^{ASE}$, $4\times I_{th}^{ASE}$, $8\times I_{th}^{ASE}$) and estimated optical gain values, indicated.

and BF14-hex oligomers are displayed in Fig. 4.38. The inconsistence of experimental and modeling results for large stripe lengths (l > 0.1 cm) was caused by the gain saturation. The variation of pump intensity from $2\times I_{th}^{ASE}$

to $8\times I_{th}^{ASE}$ resulted in the boost of g from 14 to 45 cm^{-1} and from 34 to 77 cm^{-1} for BF12-hex and BF14-hex, respectively. The obtained maximum experiment limited g of 77 cm^{-1} is among the highest reported for organic compounds.[176–179] High gain is advantageous since it enables manufacturing of compact lasers, which are more tolerant to fabrication defects.[16165]

To assess the photostability of the oligomers at the conditions approaching those of a working laser device, ASE intensity was monitored as a function of the number of pump pulses at the pump density equal to $2 \times I_{th}^{ASE}$ (Fig. 4.39). $t_{1/2}^{ASE}$ values were estimated for the oligomers in air and nitrogen atmosphere to reveal the influence of detrimental photo-oxidation, *i.e.*, generation of carbonyl defects.[180] BF12-et and BF12-hex expressed similar $t_{1/2}^{ASE}$ of 1.3×10^4 and 4×10^4 pump pulses in air and inert

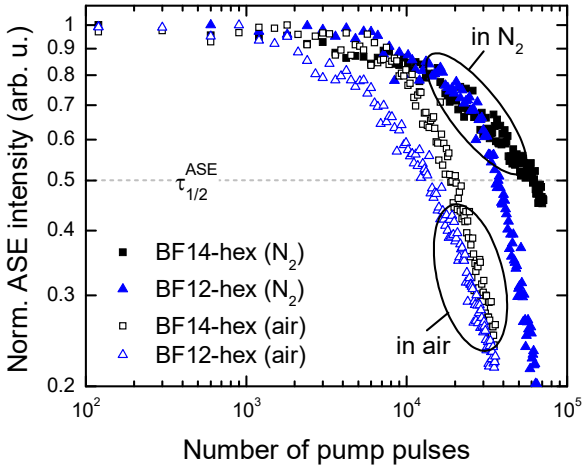

Fig. 4.39. Normalized ASE intensity dependence on the number of pump pulses in air (empty points) and nitrogen atmosphere (solid points) for BF12-hex and BF14-hex dispersed in PS matrix at the concentration corresponding to the lowest I_{th}^{ASE}. The excitation power densities were $2\times I_{th}^{ASE}$.

atmosphere, respectively, whereas for BF14-et and BF14-hex these lifetimes were 2×10^4 and 6×10^4 pulses. The greater photostability revealed for fluorene-cored oligomers was mainly due to the reduced ASE threshold, whereas 3-fold worse photostability obtained in air as that in

inert atmosphere was evidently conditioned by photo-oxidation. The estimated $t_{1/2}^{ASE}$ well exceeding 1×10^4 pump pulses was found to be comparable or even better as the lifetimes of analogous BF12 and BF14 compounds with fluorene sidegroups linked at 3rd position.

The estimation of the drift mobility for oligomer BF12-et was impossible due to the extremely dispersive carrier transport in the film. The rest oligomers BF14-et, BF14-hex and BF12-hex exhibited much less dispersive transport accompanied by the substantial increase of μ_h with the electric field. Essentially, the oligomers exhibited rather high μ_h ranging from 3×10^{-3} cm^2/V/s to 8×10^{-3} cm^2/V/s at an electric field of 1 MV/cm.[181] Such mobilities (approaching 10^{-2} cm^2/V/s) obtained in solution-casted amorphous films of the studied oligomers are considered to be very high. Unfortunately, the studied oligomers suffer from steep increase in ASE thresholds in the neat films (see Fig. 4.37). These results support the trade-off (discussed above) between low ASE threshold and good charge carrier transport properties.

4.2.9 Summary

A series of low-molecular-weight compounds utilizing fluorene and benzo[c]fluorene core and emitting in the deep-blue spectral range were synthesized and studied as potential lasing materials. The compounds were designed to have biphenyl, methoxyphenyl or more bulky dialkylfluorene sidegroups linked at 2nd or 3rd position in order to evaluate the impact of fluorene sidegroup linking topology. Unlike the majority of high-emission-efficiency chromophores, the investigated compounds were found to express small concentration quenching of emission, and thus, weak intermolecular interactions as a result of sterically-hindered peripheral groups (different-length alkyl moieties). High emission quantum yield (70-90%) was preserved up to the

concentrations of 10 wt % in polymer matrix and was reduced only by a factor of 2 in the neat films. ASE properties assessed in the so-called mirrorless configuration enabled to reveal intrinsic potential of fluorene and benzofluorene compounds as low ASE threshold (I_{th}^{ASE}) media for lasing applications. The weak concentration quenching of benzo[c]fluorene compound with fluorene sidegroups attached at the 3rd position accompanied by high radiative decay rates (>4×10^8 s^{-1}) ensured a very low I_{th}^{ASE} (900 W/cm^2) in the neat amorphous film, which was spin-coated from solution in an ambient atmosphere. Interestingly, the appearance of aggregates had minimal impact on the emission efficiency, meanwhile the aggregates severely enhanced scattering of directional ASE thus dramatically increasing I_{th}^{ASE}. Utilization of bulky dihexylfluorenyl groups at the periphery prevented aggregation and favored formation of homogeneous glassy benzofluorene films with markedly reduced I_{th}^{ASE}. Additionally, spontaneous and amplified emission properties of fluorene and benzofluorene oligomers with different (2nd and 3rd) linking position of fluorene sidegroups were assessed as a function of their concentration in polystyrene matrix. 2nd linking position of fluorene sidegroups was shown to be superior over the 3rd position for achieving higher radiative decay rates, higher fluorescence efficiencies and lower ASE thresholds in isolated state. Exhibiting higher emission quantum yields (90%) and larger radiative decay rates (>1.0×10^9 s^{-1}) accompanied by weak concentration quenching of emission 2-substituted fluorene-cored oligomers demonstrated even lower ASE thresholds at higher oligomer concentrations as compared to those of 2-substituted benzofluorene-cored compounds. This made the fluorene-cored oligomers more attractive as the light amplifying medium. High value of maximum net gain (77 cm^{-1}) followed by the lowest ASE threshold (300 W/cm^2) attained for the fluorene-cored oligomers at remarkably high concentration (50 wt %) in polymer matrix indicated great potential of these compounds for lasing

application. Importantly, the photostability of the studied oligomers was demonstrated to be as good as that of the other organic lasing compounds. Additionally, a trade-off between low ASE thresholds and good charge carrier transport properties in the wet-casted amorphous fluorene and benzo[c]fluorene films was revealed.

4.3 Low threshold light amplification in bifluorene single crystals

So far, the lowest ASE thresholds attained in the organic single crystals are on the order of tens of kilowatts per square centimeter (kW/cm^2),[13,182] meanwhile the lowest thresholds observed in the amorphous neat or doped films are typically one or two orders of magnitude lower.[14,39,128,129,173,175,177] The higher thresholds in the crystals are mainly caused by the enhanced absorption losses in the bulk (reabsorption), which manifest particularly for larger, e.g. millimeter-sized crystals. Importance of intra- and intermolecular contributions to amplification process in the single-crystals has been recently highlighted.[13] Although ASE in the crystals with both H- and J-type excitonic coupling was observed, the strong coupling for both types possesses serious drawbacks such as reduced radiative decay in the former case (with strong π-π overlap) or enhanced reabsorption and exciton diffusion in the latter case. Thereby weak intermolecular coupling ensuring reduced reabsorption due to large Stokes shift, high radiative and low nonradiative decay rates similar to those of single emitting molecules, seems to be promising. Additionally, on the molecular level, moderately strong electron-vibronic coupling, i.e. reasonably high Huang-Rhys factor is desired as this also contributes to increased Stokes shift.[183] Taking all this into account, molecules exhibiting strong electron-vibronic coupling yet capable to form weakly intermolecularly coupled crystals hold great potential for light amplification.

To this end, a series of bifluorene compounds featuring either planar or twisted backbone were synthesized and investigated for light amplification. The fluorene groups, proved to be successful ingredient of organic gain materials in the previous section, were employed due to their superior emission efficiency, large radiative decay rate, and high likelihood of low ASE threshold. ASE properties of the compounds were

explored in isolated molecular state (to discern intra- and intermolecular contributions) as well as in single crystals obtained by sublimation.

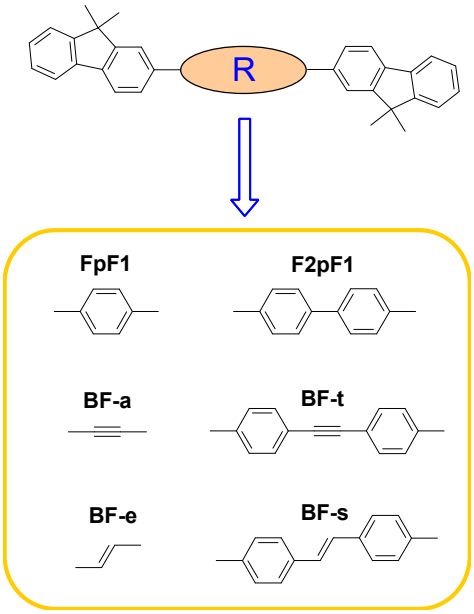

Fig. 4.40. Chemical structures bifluorene compounds used to grow single crystals.

The compounds were designed to contain either single phenyl (FpF1), biphenyl (F2pF1), acetylene (BF-a), ethylene (BF-e), tolane (BF-t) and stilbene (BF-s) bridging groups of different rigidity to reveal the effects of conjugation length and molecular packing on photophysical, and in particular, ASE properties. Thorough characterization of the optical properties of sublimation-grown crystals revealed the significant differences in their ASE performance.

4.3.1 DFT calculations and thermal properties

Ground-state geometries of the bifluorene compounds were optimized at the B3LYP/6-31G(d) level using DFT as implemented in the Gaussian 09 software package. Transition energies and oscillator strengths of the compounds were calculated using TD-DFT approach. The

calculated transition energies and corresponding oscillator strengths for the $S_0 \rightarrow S_1$ transition are summarized in Table 6.

Table 6. Calculated transitions energies and oscillator strengths for $S_0 \rightarrow S_1$, and $T_0 \rightarrow T_1$ transitions of the bifluorene compounds FpF1, F2pF1, BF-a, BF-t, BF-e and BF-s.

Compound	$E^{S_0 \rightarrow S_1}$(eV)	$f^{S_0 \rightarrow S_1}$	$E^{S_0 \rightarrow T_1}$(eV)
FpF1	3.594	1.670	2.642
F2pF1	3.550	2.0723	2.637
BF-a	3.341	1.848	2.281
BF-t	3.240	2.629	2.337
BF-e	3.216	1.875	2.008
BF-s	3.121	2.584	2.064

The HOMOs and LUMOs of FpF1 and F2pF1 are illustrated in Fig. 4.41. The calculations revealed twisted geometries of both compounds in the ground state with dihedral angles of 36° between all the neighboring fragments. Dimethyl moieties attached to the fluorene end-groups, as expected, were found to be out-of-plane twisted, i.e. oriented perpendicularly to the plane of fluorene units, providing increased intermolecular separation in the crystalline phase. In contrast, molecular backbones of rigid acetylene and ethylene groups bearing BF-a and BF-e compounds were found to be planar. The electron density in HOMO and LUMO was extended throughout the whole backbone for all the investigated compounds, which is a prominent feature of well-conjugated 2,7-substituted fluorene-based oligomers.[173,184] Obviously, the longer backbones of F2pF1, BF-t and BF-s conditioned greater conjugation, and consequently, enhanced oscillator strength as compared to those of FpF1, BF-a and BF-e. It is worth noting that increased oscillator strength is essential for higher radiative decay rates, and thus reduced ASE threshold.

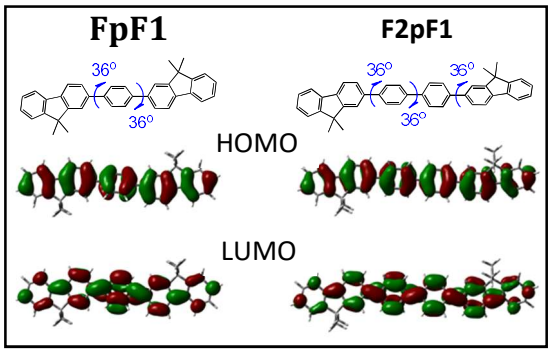

Fig. 4.41. Optimized geometry and HOMO and LUMO of bifluorene compounds FpF1 and F2pF1 calculated using the B3LYP/6-31G(d) basis set.

Relatively high planarity and the absence of long bulky alkyl groups in investigated bifluorene compounds resulted in their high crystallinity, which was proved by DSC measurements. Fig. 4.42 shows DSC second heating and cooling curves of FpF1 and F2pF1 compounds.

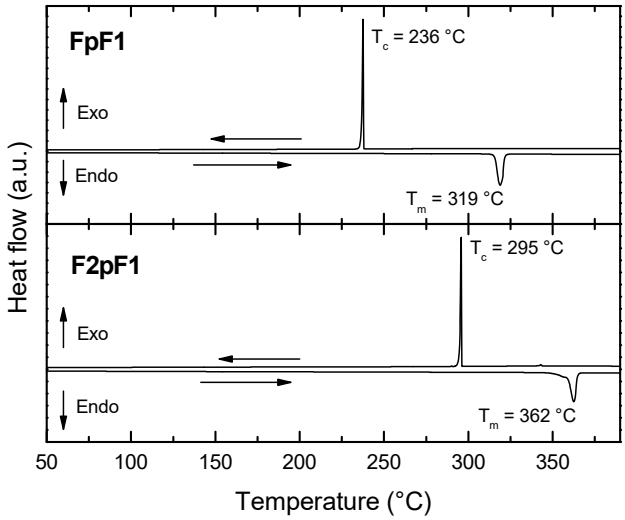

Fig. 4.42. DSC second heating and cooling scans of the bifluorene compounds FpF1 and F2pF1. DSC thermograms were taken at 10 K/min heating/cooling rate.

Thermal properties of all the bifluorene compounds are summarized in Table 7. High melting point and crystallization temperatures suggest high morphological stability of investigated compounds. Note, that for all six bifluorene compounds glass transition was not observed. No indications

off possible crystal polymorphs were found in DSC data, i.e. all the compounds exhibited single sharp crystallization peaks. Such thermal properties make bifluorene compounds extremely attractive for the growth of single crystals by physical vapour transport technique.

Table 7. Thermal properties of investigated bifluorene compounds evaluated from DSC second heating and cooling curves.

Compound	T_m (°C)	T_c (°C)
FpF1	319	236
Fp2F1	362	295
BF-a	214	180
BF-t	316	285
BF-e	294	260
BF-s	363	291

4.3.2 Absorption and emission properties

Optical microcopy images of the investigated bifluorene based single crystals grown by physical vapour transport are shown in Fig 4.43. Absorption and fluorescence spectra of the FpF1 and F2pF1 compounds dispersed in PS matrix at the concentration of 1 wt % as well as of their single crystals are displayed in Fig. 4.44. Relatively low concentration of the compounds in PS matrix ensured conditions of non-interacting molecules and enabled to investigate intramolecular properties of the compounds in a rigid and inert medium. PS films of both bifluorene compounds bearing phenyl or biphenyl core were found to exhibit strong absorption bands in the UV range peaking at 3.72 eV (for FpF1) and 3.69 eV (for F2pF1) with extinction coefficients of 3.2×10^4 and 4.5×10^4 M^{-1} cm^{-1}, respectively. The bands were attributed to $S_0\rightarrow S_1$ optical transition.

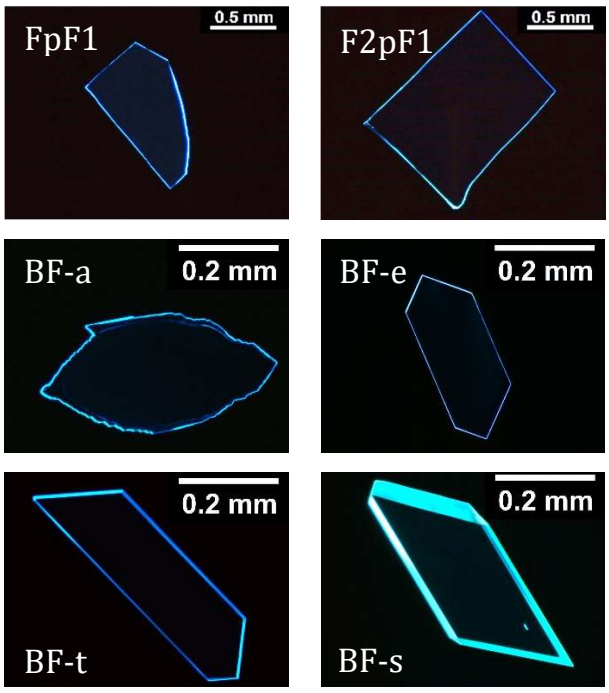

Fig. 4.43. Optical fluorescence microscopy images of singles crystals grown from bifluorene compounds by physical vapour transport technique.

Slightly lower peak energy and larger oscillator strength observed for more conjugated F2pF1 is in agreement with DFT calculations. Broad and structureless absorption bands of the compounds in PS films indicated presence of variety of conformers caused by differently-twisted labile molecular backbones.[143,183]

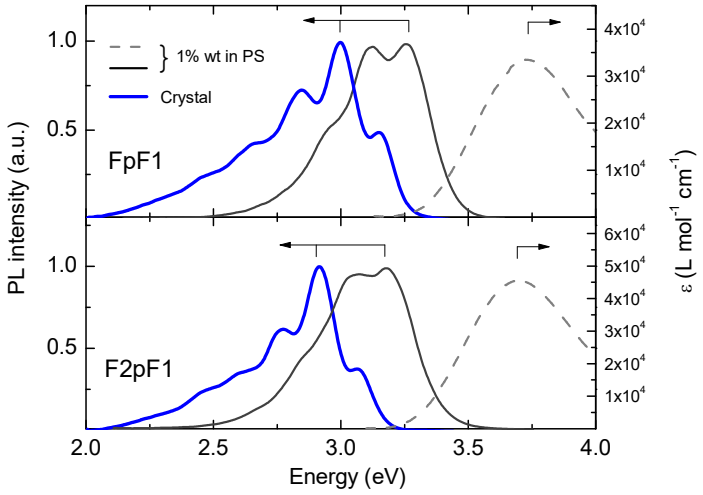

Fig. 4.44. Absorption (dashed line) and fluorescence (solid line) spectra of FpF1 and F2pF1 in 1 wt% PS films and of their single crystals.

On the other hand, resolved vibronic progression (0-0, 0-1, 0-2, 0-3) in the fluorescence spectra of PS films most likely signified only the emissive part of conformers, which were twisted at a certain angle. A comparable intensity of 0-0 and 0-1 vibronic bands indicating substantial Huang-Rhys factor and the remarkable Stokes shift of 0.5 eV confirmed an enhanced electron-vibronic coupling feasible for molecules with labile backbone. Increase of compound concentration above 1 wt% in PS films showed early signs of aggregation. The spectral shifts to lower energies as well as formation of micro-crystallites proved by fluorescence microscopy were observed. PL spectra of the single crystals of FpF1 and F2pF1 were found to be considerably redshifted (>0.1 eV) in respect to 1 wt% PS films as a result of increased intermolecular coupling (Fig. 4.44). Moreover, substantial increase of the intensity of 0-1 vibronic peak as compared to that of 0-0 peak in the single crystals indicated enhanced electron-vibronic coupling. It is worth noting that absorption and emission spectra were found to be highly anisotropic indicating preferable alignment of the molecules (transition dipole moments) in the crystal lattice.

Fig. 4.45 shows spectrally-integrated excited state relaxation dynamics of compounds FpF1 and F2pF1 dispersed in 1 wt% PS films as well as of their single crystals. In PS films the bifluorene compounds exhibited single exponential decay profiles with τ_F of 0.67 ns and 0.58 ns for FpF1 and F2pF1, respectively. τ_F constants were found to be very similar to those obtained in dilute solutions. High fluorescence quantum yields (Φ_F ~90%) estimated for the compounds in PS films confirmed the radiative decay to be the major excited state relaxation pathway. Estimated very large radiative decay rates of FpF1 (k_r =1.30×10^9 s^{-1}) and F2pF1 (k_r =1.55×10^9 s^{-1}) and nearly an order of magnitude lower nonradiative rate proved the superiority of compounds for light amplification.[128]

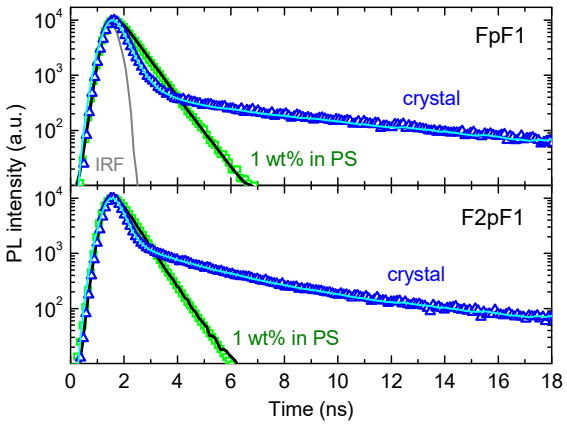

Fig. 4.45. Spectrally-integrated fluorescence decay transients of FpF1 and F2pF1 in 1 wt% PS films (rectangles) and of their single crystals (triangles). Exponential decay fits of the transients (colour solid lines) and instrument response function - IRF (grey line) are indicated.

Interestingly, fluorescence transients of FpF1 and F2pF1 single crystals displayed multi-exponential behavior with the dominant decay component (with fractional intensity >50%) 2-fold shorter as compared to τ_F determined in PS films. The transients additionally contained long-lived red-shifted decay component (τ_F ~10 ns), which was associated with impurities (trap states). However, the traps contributed to less than 25% of overall decay resulting in the corresponding drop of Φ_F from 90% in PS films to 61% and 65% in FpF1 and F2pF1 single crystals, respectively.

Enhanced planarity of BF-a, BF-e, BF-t and BF-s compounds resulted in a fast aggregate formation even at low compound concentrations in PS host. To examine the photophysical properties of these compounds in the isolated state their dilute THF solutions were prepared. Absorption and fluorescence spectra of these bifluorene compounds in dilute solution indicate bathochromic shift for ethylene-bridged compounds BF-e and BF-s as compared to those possessing acetylene linkage (BF-a and BF-t) (Fig. 4.46). Moreover, slight enhancement in molar extinction coefficients was observed for compounds featuring longer backbones (BF-t and BF-s) as compared to

those with the shorter ones (BF-a and BF-e). These results were found to be in a good agreement with DFT calculations. Note that the absorption

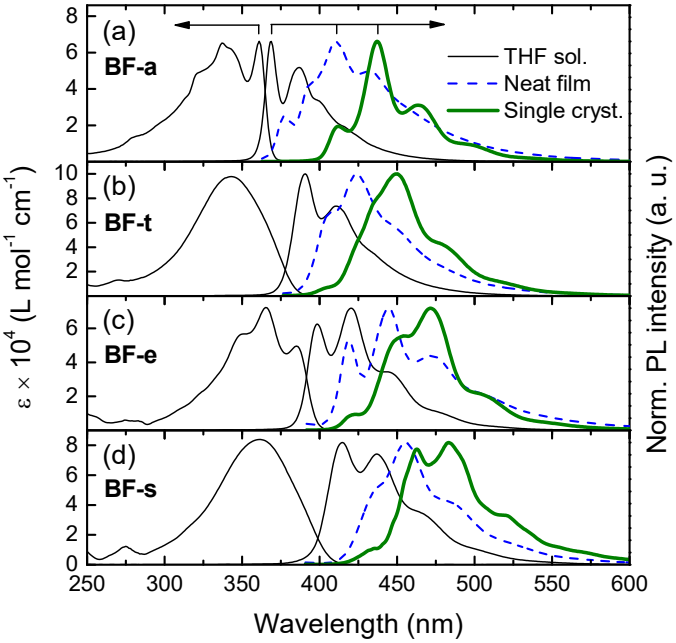

Fig. 4.46. Absorption and fluorescence spectra of bifluorene compounds a) BF-a, b) BF-t, c) BF-e and d) BF-s in 10^{-5} M THF solutions (thin solid line) along with their fluorescence spectra in the neat films (dashed line) and single crystals (thick solid line).

spectra of compounds with co-planar geometry (BF-a and BF-e) exhibit nicely resolved vibronic structure, whereas compounds BF-t and BF-s with twisted geometry yield smoothened absorption bands. The unstructured bands are most likely caused by non-rigid molecular backbones giving rise to the absorption contributing from a variety of differently twisted conformers as in the case of compounds FpF1 and F2pF1. On the other hand, a well resolved vibronic structure of the emission spectra is a result of an ultrafast torsional relaxation to a defined lower-energy excited state, known to occur in single bonded molecular structures.[185] Emission spectra of isolated molecules in the solution in most cases have dominating 0th vibronic band. Conversely, the 1st and 2nd vibronic replicas prevail in the spectra of the neat films and single crystals. Rather typical bathochromic

shift of fluorescence spectra for the bifluorene neat films and single crystals as compared to the spectra of isolated molecules is attributed to enhanced intermolecular interaction. Generally, the positions of vibronic peaks of the polycrystalline neat films match those of the single crystalss (except for BF-a), however their intensity distribution is different. Lower intensity of the higher energy vibronic replicas in the single crystals as compared to those in the neat films is due to larger reabsorption in the bulk of the crystal. The origin of the 0^{th} and 1^{st} vibronic replicas, which are observed in the neat film, but are not present in the single crystals of BF-a will be discussed below.

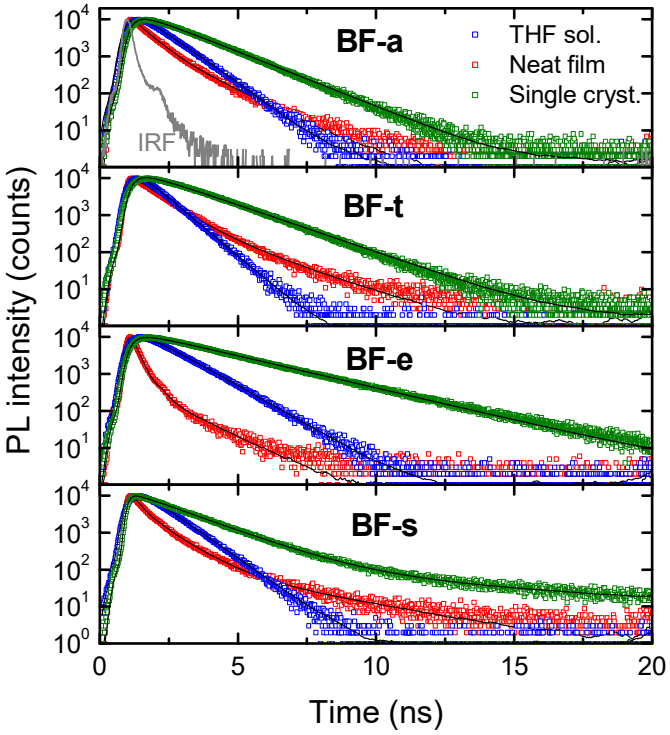

Fig. 4.47. Fluorescence decay transients at the PL peak of BF-a, BF-t, BF-e and BF-s in 10^{-5} M THF solutions (blue points), neat films (red points) and single crystals (green points). Exponential decay fits of the transients (black solid lines) and IRF (grey line) are indicated.

Φ_F of the rigidified bifluorene compounds in dilute solutions were estimated to be very high (82 - 94%), which accompanied by rather short fluorescence lifetimes τ (0.66 – 0.99 ns) resulted in high radiative

decay rates, k_r ~10^9 s^{-1}. Although emission spectra of the neat films and crystals revealed that both sample types should share similar intermolecular coupling properties, pronounced differences in emission efficiency and decay lifetimes have been observed.

Strongly reduced Φ_F (down to 7%) and τ was obtained in the polycrystalline neat films signifying enhanced non-radiative decay most likely occurring at the grain boundaries of the sub-micron sized crystallites. Although fluorescence transients of the isolated molecules in solution exhibited single exponential decay, the transients of neat films expressed non-exponential decay, which could be explained by the different time required for the excitons to reach quenching sites (e.g. grain boundaries etc.). Plots of fluorescence decay transients are provided in Fig. 4.47. Importantly, the single crystals of rigidified bifluorene compounds showed intense blue emission with very high Φ_F (72 - 82%), close to those estimated for isolated molecules, indicating only small amount of defects present, and consequently, excellent quality of the crystals obtained by sublimation technique. Strong emission from the crystal edges observed by optical microscope under UV excitation confirmed efficient light confinement in the singles, and thereby their excellent waveguiding properties (Fig. 4.43). Fluorescence transients of the crystals followed single exponential decay profile with τ (1.5 – 2.5 ns) about twice as long as for isolated molecules. This implied 2-3 times reduced k_r (down to ~0.4×10^9 s^{-1}) in the single crystals as compared to that in the isolated molecules and suggested molecular packing to be more of H-type.[13,33,186,187] However, the reduced k_r was found to be sufficiently high to dominate over k_{nr}, what encouraged to test these crystals for light amplification.

4.3.3 Amplified spontaneous emission

Amplified spontaneous emission properties of bifluorene single crystals were investigated by using thin excitation stripe technique. Fig. 4.48a shows typical excitation power dependence of the edge emission spectra of F2pF1 dispersed in PS film at a concentration of 1 wt%, whereas such dependence for F2pF1 single crystal is displayed in Figure 4.48b. The analogous excitation power dynamics was also observed for compound FpF1 in PS matrix and single crystal. Generally, broad spontaneous emission bands at low pump density transform to spectrally narrower bands with the increasing pump intensity above the onset of ASE. The ASE bands of the single crystals are narrower as compared to those of compounds in PS films due to significantly diminished inhomogeneous broadening in highly ordered crystalline phase. The ASE peaks emerge at the 1st vibronic replica due to the reabsorption of higher-energy slope of edge emission spectra. The emission band narrowing with increasing pump is followed by an abrupt change in the emission intensity profile from linear to superlinear at I_{th}^{ASE} (see insets of 4.48a and 4.48b).

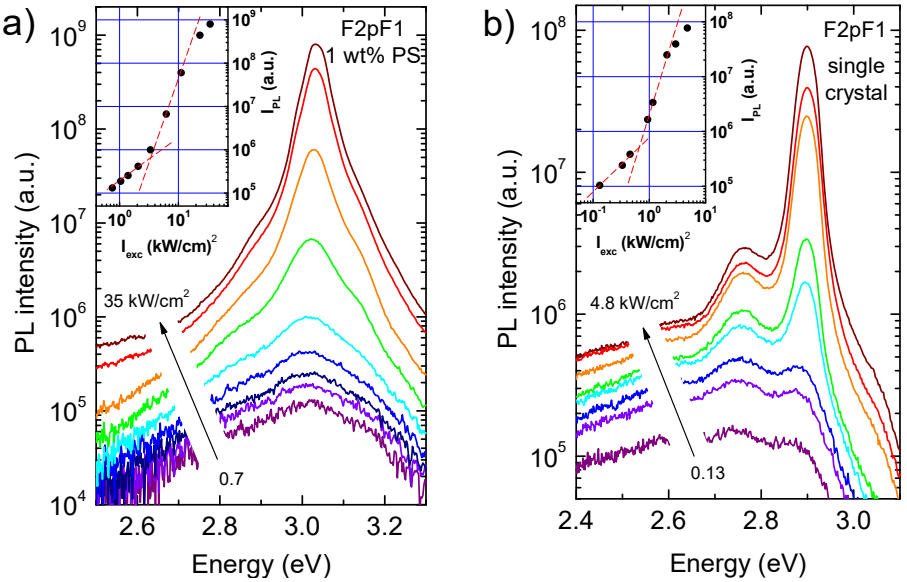

Figure 4.48. Excitation power dependence of the edge emission spectra of F2pF1 in a) 1 wt% PS film and b) single crystal. Insets show emission peak intensity *vs.* excitation power density ($I_{exc.}$).

I_{th}^{ASE} values as a function of FpF1 and F2pF1 concentration in PS matrix is plotted in Fig. 4.49 along with the data obtained for single crystals. An increase of compound concentration up to 1 wt% (for F2pF1) or 4 wt% (for FpF1) causes drop of I_{th}^{ASE}, which is followed by steep increase of the threshold values above these concentrations. High I_{th}^{ASE} at low compound concentrations is associated with enhanced absorptive losses due to the large intermolecular distances. Increasing concentration in PS matrix reduces intermolecular spacing resulting in smaller critical exciton density and thus lower I_{th}^{ASE}. Note somewhat lower I_{th}^{ASE} for F2pF1 as compared to that for FpF1 in the low concentration range (<1 wt%), which is due to the larger k_r of F2pF1. The minimum I_{th}^{ASE} values, i.e. 2 kW/cm² and 3 kW/cm², were attained at the optimal concentrations of 4 wt% and 1 wt% for FpF1 and F2pF1, respectively. The difference in the optimal concentrations is evidently caused by the different onsets of the steep I_{th}^{ASE} increase with the compound mass fraction in PS matrix. This can be explained either by

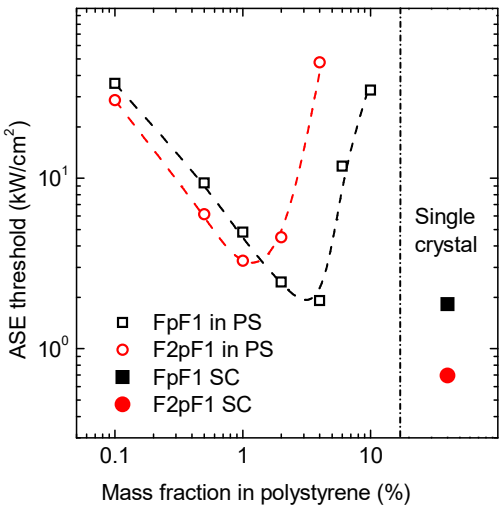

Fig. 4.49. ASE threshold as a function of compound concentration in PS films with single crystal values indicated. Lines are guides for the eye.

unequally strong concentration quenching or light scattering induced by formation of microcrystallites. Since F2pF1 featuring larger biphenyl core

is more prone to aggregation, the concentration quenching effects for this compound in PS films start earlier. However, the concentration quenching of emission is insignificant. For instance, initially high Φ_F (~90%) is quenched only down to ~60% with the increase of F2pF1 concentration up to 10 wt%, whereas I_{th}^{ASE} increases by more than one order of magnitude. On the other hand, sufficiently large compound concentration causes formation of aggregates, which increase in their number and size along with the compound mass fraction in PS films resulting in the enhanced light scattering. The light-scattering of directional amplified emission increases optical losses and I_{th}^{ASE}. Thus, appearance of microcrystallites in PS matrix already above 1 wt% for F2pF1 conditions earlier increase of I_{th}^{ASE}, and consequently, lower optimal concentration for light amplification as compared to those for FpF1.

Single crystals as highly ordered and homogeneous media offer an attractive solution in minimizing scattering losses while simultaneously allowing to maintain high exciton density required for low I_{th}^{ASE}. For the optimal ASE performance, sublimation-grown plate-like single crystals of FpF1 and F2pF1 with a thickness of ~500 nm were employed. Excellent quality of the crystal facets was confirmed by atomic force microscopy measurements, which revealed very low surface roughness (RMS <0.6 nm) across 50×50 μm area. High crystal quality was also confirmed by SEM measurements. Additionally, optical microscopy images (Fig. 4.43) showing bright emission at the crystal edges indicated good waveguiding properties of the crystals. In contrast to concentrated PS films, significantly lower I_{th}^{ASE} were obtained for FpF1 and F2pF1 single crystals, i.e. 1.8 kW/cm^2 (9.2 μJ/cm^2) and 0.7 kW/cm^2 (3.5 μJ/cm^2), respectively. The reduced I_{th}^{ASE} in the bifluorene single crystals can be justified by severely reduced optical losses associated with light-scattering as well as enhanced waveguiding. Lower I_{th}^{ASE} of F2pF1 single crystal as compared to that of FpF1 is possibly a consequence of higher radiative rate, that is,

somewhat higher Φ_F and shorter dominant τ_F, since the impact of excited state absorption in the gain region was neglected.[188]

To evaluate the impact of molecular structure planarity and rigidity on light amplification, ASE properties of BF-a, BF-t, BF-e and BF-s single crystals were examined. Excitation power dynamics of the edge emission spectra of BF-a and BF-e featuring rigid co-planar molecular structure is displayed in Fig. 4.50. Evidently, broad spontaneous emission bands observed at low excitation density become narrower with the increasing pump density above the onset of stimulated optical transitions. The ASE peaks emerge at the 1st (BF-a) or 1st and 2nd (BF-e) vibronic replicas, while the highest energy 0th vibronic band of both samples is reabsorbed in the bulk of the crystal. The spectral narrowing with increasing excitation power density is accompanied by an abrupt change in the emission intensity profile from linear to superlinear at I_{th}^{ASE} (see insets of Fig. 4.50a and 4.50b). Interestingly, an order of magnitude

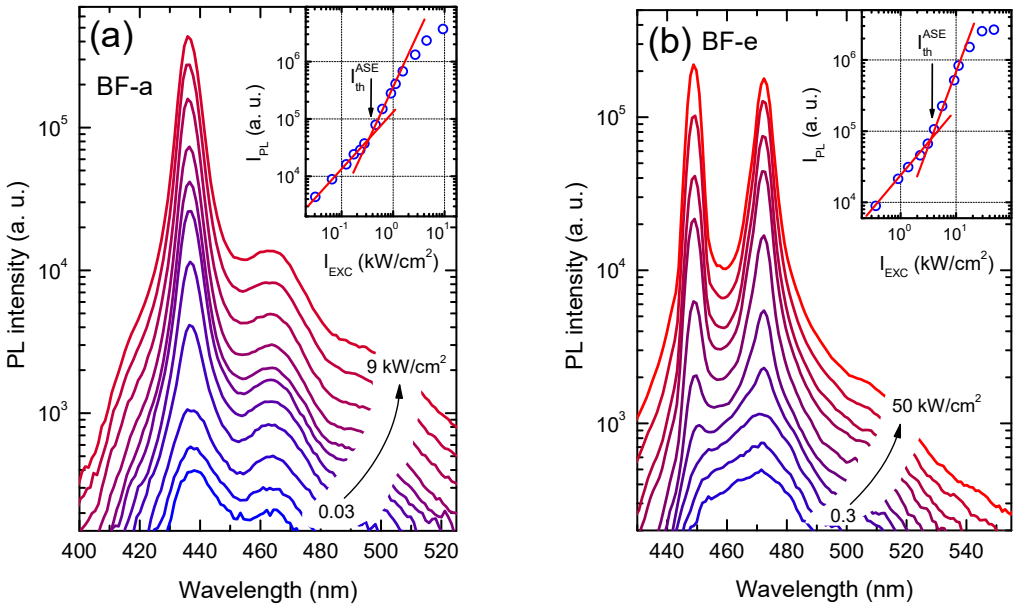

Figure 4.50. Edge emission spectra at different excitation power densities for bifluorene SCs a) BF-a and b) BF-e. Insets show emission peak intensity *vs.* $I_{exc.}$.

lower I_{th}^{ASE} for BF-a crystal (0.4 kW/cm^2) as compared to that for BF-e (3.4 kW/cm^2) was obtained. Single crystals of BF-t and BF-s exhibited up to two orders of magnitude higher I_{th}^{ASE}, 30 and 50 kW/cm^2, respectively, as compared to that of BF-a, due to the enhanced excited state absorption in the gain region.[189] Such low I_{th}^{ASE} observed for BF-a crystal was found to be even lower to that demonstrated in labile biphenylyl core containing F2pF1. Such differences in I_{th}^{ASE} of bifluorene studied crystals can be caused by several reasons, i.e. different radiative decay rates, exciton annihilation impeding attainment of critical exciton density, excited state absorption overlapping with the gain region, molecular dipole orientation, etc. Since differences in radiative decay rates among the different investigated crystals are less than 2-fold, they can be considered as insignificant for ASE properties. Exciton annihilation can play a remarkable role at high excitation densities by reducing exciton concentration, and thus preventing population inversion. The signs of annihilation could be traced by the deviation from linear fluorescence intensity dependence vs excitation power density before the onset of ASE. Since no noticeable deviations were observed (see insets of Fig. 4.50) the impact of exciton annihilation to I_{th}^{ASE} was disregarded. The impact of molecular dipole orientation was eliminated (to some extent) by estimating I_{th}^{ASE} at various crystal directions and selecting the one with the lowest I_{th}^{ASE}. Finally, analysis of the excited state absorption and population dynamics revealed potential mechanisms of energy transfer to lower-energy trap states, which could explain significant differences in I_{th}^{ASE} values of all the investigated bifluorene crystals containing rigid core.

4.3.4 Emissive trap states

Important differences were revealed in the absorption spectra of single crystals of BF-a and and BF-e. These spectra along with

fluorescence spectra for BF-a and BF-e are depicted in Fig. 4.51. In the absorption spectrum of BF-e the dominant absorption band corresponds to the lowest 0-0^{C} vibronic replica at 415 nm, meanwhile the strongest absorption band of BF-a is 0-0^{C} vibronic transition at 375 nm. However, an additional lower-energy band 0-0^{T} was observed at 405 nm, which was found to be two orders of magnitude weaker in intensity as compared to that of 0-0^{C}. In the crystals of BF-e, BF-s and BF-t Stokes shift between 0-0 bands of absorption and fluorescence was estimated to be small in accordance with the rigid structure of molecules. Due to the strong reabsorption in the crystals the first vibronic bands of fluorescence spectrum are much weaker. Interestingly, since 0-0^{T} band of fluorescence spectrum of BF-a coincides with the 0-0^{T} band in absorption spectrum, the origin of fluorescence may be attributed to this low-energy state (ultrafast transient absorption experiments provided support for this assignment).[189] Importantly, although the low-energy state has weak absorption it exhibits high Φ_F (78%) and short τ_F (1.46 ns) indicating strong oscillator strength of the transition. Thus, it cannot be associated with the forbidden excitonic state and thereby must be attributed to some emissive traps constituting less than 1% of the crystal states (see Figure 4.51a). The nature of emissive traps was also supported by temperature independent PL spectra.[189] Obviously, the emissive traps play a crucial role in achieving extremely low I_{th}^{ASE} in BF-a based crystals implying the essential difference from the other studied bifluorene single crystals. Note that ASE in doped organic crystals was observed already in 1970.[190] Generally, introduction of dopants is an attractive approach enabling to reduce reabsorption as well as non-radiative decay due to exciton trapping, and thus permitting to lower I_{th}^{ASE}.[134]

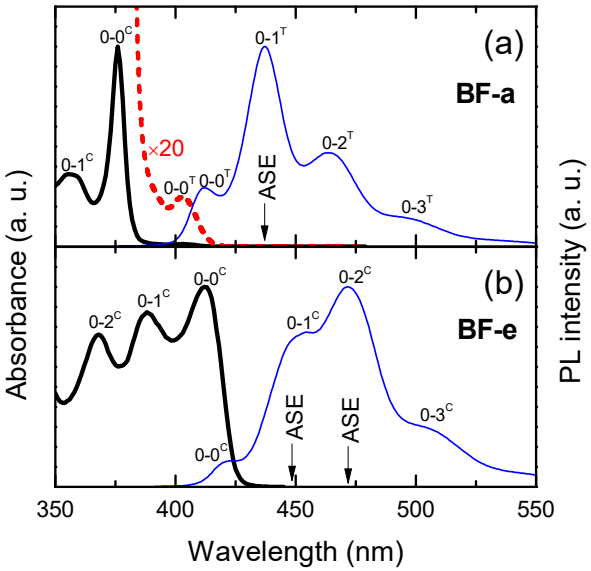

Figure 4.51. Absorption (thick solid lines) and fluorescence (thin solid lines) spectra of bifluorene SCs a) BF-a and b) BF-e. Dashed line, absorption spectrum multiplied by a factor of 20. Arrows indicate ASE peaks.

4.3.5 Summary

Bifluorene compounds were designed to possess twisted or planar molecular structure to evaluate the impact of intermolecular interactions in single crystals on their ASE properties. Singly-bonded phenyl and biphenyl central groups and out-of-plane sticking dimethyl moieties in bifluorene chromophores reduced intermolecular coupling and enhanced fluorescence and ASE properties in the solid state. The flexible molecular backbone also facilitated increased electron-vibronic coupling implying large Stokes shift (0.5 eV) and thereby reduced reabsorption of emission. Indeed, initially high fluorescence quantum yields (Φ_F ~90%) of deep-blue emitting bifluorene with phenylyl central groups dispersed in PS films at low concentrations remained sufficiently high (Φ_F >60%) in their single crystals. Moreover, twisted bifluorene compounds showed great potential in light amplification expressing low ASE thresholds (down to 2 kW/cm^2) when dispersed in PS matrix and even lower ones (down to 700 W/cm^2) for single-crystalline phase. Such

low thresholds were found to be caused by high radiative rates (inherent intramolecular property), absence of excited-state absorption in the gain region and favorable orientation of transition dipole moments accompanied by excellent waveguiding properties of the single crystals. Furthermore, another group of bifluorene compounds investigated in this work were designed to possess molecular structure comprising of ethylene and acetylene bridging moieties. Introduction of rigid ethylene and acetylene linking groups enabled high Φ_F (82 - 94%) and short excited state decay time (0.7 – 1.0 ns) in the isolated bifluorene molecules, whereas sublimation grown single crystals were found to express low non-radiative decay rate ensuring high Φ_F (72 – 82%) and short fluorescence lifetime (1.5 – 2.5 ns). This implied high radiative decay rates ($\sim 0.5 \times 10^9\ s^{-1}$) of the crystals also making them highly promising for lasing applications. Amplified spontaneous emission measurements revealed ASE thresholds in the crystalline medium ranging from 0.4 to 50 kW/cm^2. The lowest ASE threshold of 400 W/cm^2 estimated for bifluorene compound bearing acetylene linkage is among the lowest ever reported for organic crystals. The lowest ASE threshold was caused by low density (<1%) emissive trap states, which were populated via efficient energy transfer from intrinsic excitonic (crystal) states. The origin of emissive trap states remains to be disclosed in the future studies. Up to two orders of magnitude higher ASE thresholds were obtained for the bifluorene single crystals featuring linkages with extended conjugation. This was caused by enhanced excited state absorption in the gain region. The obtained results indicate that rational design of the molecules enables to realize weak intermolecular (and excitonic) coupling in the crystalline solids to the extent resembling non-interacting chromophores in diluted media, what results in very low ASE thresholds. This study also suggests that the crystal doping approach allows to achieve even lower ASE thresholds required for organic electrically-pumped lasers.

5 Conclusions

1. Morphology and emission tuning was realized in phenylenediacetonitrile-based nanoparticles. Crystalline (highly fluorescent) and amorphous (weakly fluorescent) morphologies of formed nanoparticles and films were clearly discerned. High fluorescence efficiency (Φ_F=70%) was achieved in crystalline nanoparticles of PDACN compound decorated with branchy dihexyloxy groups by exploiting aggregation induced enhancement phenomenon. THF vapour sensing via the change of emission colour and intensity of PDACN-based nanoparticle films was demonstrated. A minute time exposure of THF vapour or thermal stimulus resulted in the change of fluorescence spectra and intensity of PDACN-doped polystyrene films via aggregate formation induced by molecular diffusion in the softened polymer. Phenylenediacetonitriles were demonstrated to have a potential to be utilized as volatile vapour or threshold-temperature fluorescence sensors.
2. Intermolecular interactions and fluorescence concentration quenching in fluorene- and benzo[c]fluorene-cored oligomers were suppressed by bulky dialkylfluorene sidegroups and twisted molecular geometry. Efficient fluorescence (Φ_F=70-90%), high radiative decay rates (>4x10^8 s^{-1}) and weak concentration quenching allowed to achieve very low amplified spontaneous emission threshold in benzo[c]fluorene-dihexylfluorene-based neat film (900 W/cm^2) and fluorene-diethylfluorene-doped (50 wt%) polystyrene film (300 W/cm^2). Low amplified spontaneous emission thresholds ensured sufficient photostability of fluorene and benzo[c]fluorene oligomers. 2nd linking position of fluorene sidegroups in fluorene/benzo[c]fluorene oligomers is superior to the 3rd position for achieving high radiative decay rates, high fluorescence quantum yield

and low amplified spontaneous emission threshold in the isolated state. A trade-off between low amplified spontaneous emission threshold and good charge transport properties was revealed.

3. Intermolecular coupling was reduced in bifluorene-biphenyl single crystals by twisted molecular structure and out-of-plane sticking dimethyl groups. This resulted in high fluorescence quantum yields (Φ_F >60%) in single crystals. Weak intermolecular coupling combined with high radiative decay rates (up to $1.5x10^9$ s^{-1}) and small reabsorption ensured very low amplified spontaneous emission threshold (700 W/cm^2). High fluorescence efficiencies (Φ_F=72-82%) and high radiative decay rates ($0.5x10^9$ s^{-1}) were also demonstrated for single crystals based on bifluorene compounds bearing rigid acetylene and ethylene linkages. ASE performance in these crystals was decreased by enhanced excited state absorbtion. The lowest amplified spontaneous emission threshold in crystalline state (400 W/cm^2) demonstrated for bifluorene compound linked with acetylene group was caused by emissive trap states. Bifluorene-based single crystals and crystal doping approach are promising for designing organic laser gain medium.

6 References

(1) Ostroverkhova, O. Organic Optoelectronic Materials: Mechanisms and Applications. *Chem. Rev.* **2016**, *116* (22), 13279–13412.

(2) Liao, C.; Zhang, M.; Yao, M. Y.; Hua, T.; Li, L.; Yan, F. Flexible Organic Electronics in Biology: Materials and Devices. *Adv. Mater.* **2015**, *27* (46), 7493–7527.

(3) Suzuki, A. Recent Advances in the Cross-Coupling Reactions of Organoboron Derivatives with Organic Electrophiles, 1995–1998. *J. Organomet. Chem.* **1999**, *576* (1–2), 147–168.

(4) Ripaud, E.; Demeter, D.; Rousseau, T.; Boucard-Cétol, E.; Allain, M.; Po, R.; Leriche, P.; Roncali, J. Structure–properties Relationships in Conjugated Molecules Based on Diketopyrrolopyrrole for Organic Photovoltaics. *Dye. Pigment.* **2012**, *95* (1), 126–133.

(5) Duan, L.; Hou, L.; Lee, T.-W.; Qiao, J.; Zhang, D.; Dong, G.; Wang, L.; Qiu, Y. Solution Processable Small Molecules for Organic Light-Emitting Diodes. *J. Mater. Chem.* **2010**, *20* (31), 6392.

(6) Miwa, T.; Kubo, S.; Shizu, K.; Komino, T.; Adachi, C.; Kaji, H. Blue Organic Light-Emitting Diodes Realizing External Quantum Efficiency over 25% Using Thermally Activated Delayed Fluorescence Emitters. *Sci. Rep.* **2017**, *7* (1), 284.

(7) Dimitrakopoulos, C. D.; Malenfant, P. R. L. Organic Thin Film Transistors for Large Area Electronics. *Adv. Mater.* **2002**, *14* (2), 99–117.

(8) Zhao, W.; Li, S.; Yao, H.; Zhang, S.; Zhang, Y.; Yang, B.; Hou, J. Molecular Optimization Enables over 13% Efficiency in Organic Solar Cells. *J. Am. Chem. Soc.* **2017**, *139* (21), 7148–7151.

(9) Gonçalves, M. S. T. Fluorescent Labeling of Biomolecules with Organic Probes. *Chem. Rev.* **2009**, *109* (1), 190–212.

(10) Wolfbeis, O. S. Materials for Fluorescence-Based Optical Chemical Sensors. *J. Mater. Chem.* **2005**, *15* (27–28), 2657.

(11) Shen, J.-S.; Li, D.-H.; Ruan, Y.-B.; Xu, S.-Y.; Yu, T.; Zhang, H.-W.; Jiang, Y.-B. Supramolecular Aggregation/disaggregation-Based Molecular Sensing: A Review Focused on Investigations from China. *Luminescence* **2012**, *27* (5), 317–327.

(12) Feng, J.; Xiong, L.; Wang, S.; Li, S.; Li, Y.; Yang, G. Fluorescent Temperature Sensing Using Triarylboron Compounds and Microcapsules for Detection of a Wide Temperature Range on the Micro- and Macroscale. *Adv. Funct. Mater.* **2013**, *23* (3), 340–345.

(13) Gierschner, J.; Varghese, S.; Park, S. Y. Organic Single Crystal Lasers: A Materials View. *Adv. Opt. Mater.* **2016**, *4* (3), 348–364.

(14) Wang, Y. Low Threshold Organic Semiconductor Lasers. **2014**, 9--32.

(15) Chénais, S.; Forget, S. Recent Advances in Solid-State Organic Lasers. *Polym. Int.* **2012**, *61* (3), 390–406.

(16) Samuel, I. D. W.; Turnbull, G. A. Organic Semiconductor Lasers. *Chem. Rev.* **2007**.

(17) Ho, S.; Liu, S.; Chen, Y.; So, F. Review of Recent Progress in Multilayer Solution-Processed Organic Light-Emitting Diodes. *J. Photonics Energy* **2015**, *5* (1), 57611.

(18) Müller, C. D.; Falcou, A.; Reckefuss, N.; Rojahn, M.; Wiederhirn, V.; Rudati, P.; Frohne, H.; Nuyken, O.; Becker, H.; Meerholz, K. Multi-Colour Organic Light-Emitting Displays by Solution Processing. *Nature* **2003**, *421* (6925), 829–833.
(19) Duan, L.; Hou, L.; Lee, T.-W.; Qiao, J.; Zhang, D.; Dong, G.; Wang, L.; Qiu, Y. Solution Processable Small Molecules for Organic Light-Emitting Diodes. *J. Mater. Chem.* **2010**, *20* (31), 6392.
(20) *Applications of Organic and Printed Electronics*; Cantatore, E., Ed.; Integrated Circuits and Systems; Springer US: Boston, MA, 2013.
(21) Sekine, C.; Tsubata, Y.; Yamada, T.; Kitano, M.; Doi, S. Recent Progress of High Performance Polymer OLED and OPV Materials for Organic Printed Electronics. *Sci. Technol. Adv. Mater.* **2014**, *15* (3), 34203.
(22) Geffroy, B.; le Roy, P.; Prat, C. Organic Light-Emitting Diode (OLED) Technology: Materials, Devices and Display Technologies. *Polym. Int.* **2006**, *55* (6), 572–582.
(23) Clark, J.; Lanzani, G. Organic Photonics for Communications. *Nat. Photonics* **2010**, *4* (7), 438–446.
(24) Wang, X.; Wolfbeis, O. S.; Meier, R. J. Luminescent Probes and Sensors for Temperature. *Chem. Soc. Rev.* **2013**, *42* (19), 7834–7869.
(25) Hong, Y.; Lam, J. W. Y.; Tang, B. Z. Aggregation-Induced Emission. *Chem. Soc. Rev.* **2011**, *40* (11), 5361.
(26) Heller, C. M.; Campbell, I. H.; Laurich, B. K.; Smith, D. L.; Bradley, D. D. C.; Burn, P. L.; Ferraris, J. P.; Müllen, K. Solid-State-Concentration Effects on the Optical Absorption and Emission of Poly(*P* -Phenylene Vinylene)-Related Materials. *Phys. Rev. B* **1996**, *54* (8), 5516–5522.
(27) Ma, Y.-S.; Wang, C.-H.; Zhao, Y.-J.; Yu, Y.; Han, C.-X.; Qiu, X.-J.; Shi, Z. Perylene Diimide Dyes Aggregates: Optical Properties and Packing Behavior in Solution and Solid State. *Supramol. Chem.* **2007**, *19* (3), 141–149.
(28) An, B. K.; Kwon, S. K.; Jung, S. D.; Park, S. Y. Enhanced Emission and Its Switching in Fluorescent Organic Nanoparticles. *J. Am. Chem. Soc.* **2002**, *124* (48), 14410–14415.
(29) Horn, D.; Rieger, J. Organic Nanoparticles in Aqueous Phase. *Angew. Chem. Int. Ed. Engl.* **2001**, *40* (23), 4330–4361.
(30) Li, Z.; Dong, Y. Q.; Lam, J. W. Y.; Sun, J.; Qin, A.; Häußler, M.; Dong, Y. P.; Sung, H. H. Y.; Williams, I. D.; Kwok, H. S.; et al. Functionalized Siloles: Versatile Synthesis, Aggregation-Induced Emission, and Sensory and Device Applications. *Adv. Funct. Mater.* **2009**, *19* (6), 905–917.
(31) Zhu, L. L.; Zhao, Y. L. Cyanostilbene-Based Intelligent Organic Optoelectronic Materials. *J. Mater. Chem. C* **2013**, *1*, 1059–1065.
(32) Wang, M.; Zhang, G.; Zhang, D.; Zhu, D.; Tang, B. Z. Fluorescent Bio/chemosensors Based on Silole and Tetraphenylethene Luminogens with Aggregation-Induced Emission Feature. *J. Mater. Chem.* **2010**, *20* (10), 1858.
(33) Gierschner, J.; Park, S. Y. Luminescent Distyrylbenzenes: Tailoring Molecular Structure and Crystalline Morphology. *J. Mater. Chem. C* **2013**, *1* (37), 5818.
(34) Dou, C.; Chen, D.; Iqbal, J.; Yuan, Y.; Zhang, H.; Wang, Y. Multistimuli-Responsive Benzothiadiazole-Cored Phenylene Vinylene Derivative with

Nanoassembly Properties. *Langmuir* **2011**, *27* (10), 6323–6329.
(35) Mei, J.; Hong, Y.; Lam, J. W. Y.; Qin, A.; Tang, Y.; Tang, B. Z. Aggregation-Induced Emission: The Whole Is More Brilliant than the Parts. *Adv. Mater.* **2014**, *26* (31), 5429–5479.
(36) Oelkrug, D.; Tompert, A.; Gierschner, J.; Egelhaaf, H.; Hanack, M.; Hohloch, M.; Steinhuber, E. Tuning of Fluorescence in Films and Nanoparticles of Oligophenylenevinylenes. *J. Phys. Chem. B* **1998**, *102* (11), 1902–1907.
(37) Kim, S.; Yoon, S. J.; Park, S. Y. Highly Fluorescent Chameleon Nanoparticles and Polymer Films: Multicomponent Organic Systems That Combine FRET and Photochromic Switching. *J. Am. Chem. Soc.* **2012**, *134* (29), 12091–12097.
(38) Diaz-Garcia, M. A.; Schwartz, B. J.; Hide, F.; Heeger, A. J. Conjugated Polymers as Materials for Solid-State Lasers. **1999**, No. 5,881,083, 1655–1668.
(39) McGehee, M. D.; Heeger, A. J. Semiconducting (Conjugated) Polymers as Materials for Solid-State Lasers. *Adv. Mater.* **2000**, *12* (22), 1655–1668.
(40) Fang, H.-H.; Yang, J.; Feng, J.; Yamao, T.; Hotta, S.; Sun, H.-B. Functional Organic Single Crystals for Solid-State Laser Applications. *Laser Photon. Rev.* **2014**, *8* (5), 687–715.
(41) Allard, S.; Forster, M.; Souharce, B.; Thiem, H.; Scherf, U. Organic Semiconductors for Solution-Processable Field-Effect Transistors (OFETs). *Angew. Chemie Int. Ed.* **2008**, *47* (22), 4070–4098.
(42) Takeya, J.; Yamagishi, M.; Tominari, Y.; Hirahara, R.; Nakazawa, Y.; Nishikawa, T.; Kawase, T.; Shimoda, T.; Ogawa, S. Very High-Mobility Organic Single-Crystal Transistors with in-Crystal Conduction Channels. *Appl. Phys. Lett.* **2007**, *90* (10), 102120.
(43) Tang, C. W.; VanSlyke, S. A. Organic Electroluminescent Diodes. *Appl. Phys. Lett.* **1987**, *51* (12), 913.
(44) Chan, C. Y. K.; Zhao, Z.; Lam, J. W. Y.; Liu, J.; Chen, S.; Lu, P.; Mahtab, F.; Chen, X.; Sung, H. H. Y.; Kwok, H. S.; et al. Efficient Light Emitters in the Solid State: Synthesis, Aggregation-Induced Emission, Electroluminescence, and Sensory Properties of Luminogens with Benzene Cores and Multiple Triarylvinyl Peripherals. *Adv. Funct. Mater.* **2012**, *22* (2), 378–389.
(45) Zhang, Q.; Li, B.; Huang, S.; Nomura, H.; Tanaka, H.; Adachi, C. Efficient Blue Organic Light-Emitting Diodes Employing Thermally Activated Delayed Fluorescence. *Nat. Photonics* **2014**, *8* (March), 1–7.
(46) Yamaguchi, Y.; Matsubara, Y.; Ochi, T.; Wakamiya, T.; Yoshida, Z. How the π Conjugation Length Affects the Fluorescence Emission Efficiency. *J. Am. Chem. Soc.* **2008**, *130* (42), 13867–13869.
(47) Niko, Y.; Hiroshige, Y.; Kawauchi, S.; Konishi, G. Fundamental Photoluminescence Properties of Pyrene Carbonyl Compounds through Absolute Fluorescence Quantum Yield Measurement and Density Functional Theory. *Tetrahedron* **2012**, *68* (31), 6177–6185.
(48) Lavanya Devi, C.; Yesudas, K.; Makarov, N. S.; Jayathirtha Rao, V.; Bhanuprakash, K.; Perry, J. W. Fluorenylethynylpyrene Derivatives with Strong Two-Photon Absorption: Influence of Substituents on Optical Properties. *J. Mater. Chem. C* **2015**, *3* (15), 3730–3744.
(49) Strickler, S. J.; Berg, R. A. Relationship between Absorption Intensity and

Fluorescence Lifetime of Molecules. *J. Chem. Phys.* **1962**, *37* (4), 814–822.
(50) Prathapan, S.; Yang, S. I.; Seth, J.; Miller, M. A.; Bocian, D. F.; Holten, D.; Lindsey, J. S. Synthesis and Excited-State Photodynamics of Perylene−Porphyrin Dyads. 1. Parallel Energy and Charge Transfer via a Diphenylethyne Linker. *J. Phys. Chem. B* **2001**, *105* (34), 8237–8248.
(51) Ford, W. E.; Kamat, P. V. Photochemistry of 3,4,9,10-Perylenetetracarboxylic Dianhydride Dyes. 3. Singlet and Triplet Excited-State Properties of the bis(2,5-Di-Tert-Butylphenyl)imide Derivative. *J. Phys. Chem.* **1987**, *91* (25), 6373–6380.
(52) Hanhela, P.; Paul, D. Evaluation of Fluorescent Materials for Colour Control of Peroxylate Chemiluminescence. IV. Fluorescence Quantum Yields of Some Phenyl and Phenylethynyl Aromatic Compounds. *Aust. J. Chem.* **1984**, *37* (3), 553.
(53) Más-Montoya, M.; Janssen, R. A. J. The Effect of H- and J-Aggregation on the Photophysical and Photovoltaic Properties of Small Thiophene-Pyridine-DPP Molecules for Bulk-Heterojunction Solar Cells. *Adv. Funct. Mater.* **2017**, *27* (16), 1605779.
(54) Eisfeld, A.; Briggs, J. S. The J- and H-Bands of Organic Dye Aggregates. *Chem. Phys.* **2006**, *324* (2–3), 376–384.
(55) Würthner, F.; Kaiser, T. E.; Saha-Möller, C. R. J-Aggregates: From Serendipitous Discovery to Supramolecular Engineering of Functional Dye Materials. *Angew. Chemie Int. Ed.* **2011**, *50* (15), 3376–3410.
(56) Nakul C. Maiti; Shyamalava Mazumdar, and; Periasamy*, N. J- and H-Aggregates of Porphyrin−Surfactant Complexes: Time-Resolved Fluorescence and Other Spectroscopic Studies†. **1998**.
(57) Hunter, C. A.; Sanders, J. K. M. The Nature of .pi.-.pi. Interactions. *J. Am. Chem. Soc.* **1990**, *112* (14), 5525–5534.
(58) Liao, Q.; Zhang, H.; Zhu, W.; Hu, K.; Fu, H. Perylene Crystals: Tuning Optoelectronic Properties by Dimensional-Controlled Synthesis. *J. Mater. Chem. C* **2014**, *2* (45), 9695–9700.
(59) Miasojedovas, A.; Kazlauskas, K.; Armonaite, G.; Sivamurugan, V.; Valiyaveettil, S.; Grazulevicius, J. V.; Jursenas, S. Concentration Effects on Emission of Bay-Substituted Perylene Diimide Derivatives in a Polymer Matrix. *Dye. Pigment.* **2012**, *92* (3), 1285–1291.
(60) Ferreira, J. A.; Porter, G. Concentration Quenching and Excimer Formation by Perylene in Rigid Solutions. *J. Chem. Soc. Faraday Trans. 2* **1977**, *73* (3), 340.
(61) Chen, L.; Xu, S.; McBranch, D.; Whitten, D. Tuning the Properties of Conjugated Polyelectrolytes through Surfactant Complexation. *J. Am. Chem. Soc.* **2000**, *122* (38), 9302–9303.
(62) Nguyen, B. T.; Gautrot, J. E.; Ji, C.; Brunner, P.-L.; Nguyen, M. T.; Zhu, X. X. Enhancing the Photoluminescence Intensity of Conjugated Polycationic Polymers by Using Quantum Dots as Antiaggregation Reagents. *Langmuir* **2006**, *22* (10), 4799–4803.
(63) Jia Wang; Yunfeng Zhao; Chuandong Dou; Hui Sun; Peng Xu; Kaiqi Ye; Jingying Zhang; Shimei Jiang; Fei Li, and; Wang*, Y. Alkyl and Dendron Substituted Quinacridones: Synthesis, Structures, and Luminescent Properties. **2007**.
(64) Serevičius, T.; Komskis, R.; Adomėnas, P.; Adomėnienė, O.; Jankauskas, V.;

Gruodis, A.; Kazlauskas, K.; Juršėnas, S. Non-Symmetric 9,10-Diphenylanthracene-Based Deep-Blue Emitters with Enhanced Charge Transport Properties. *Phys. Chem. Chem. Phys.* **2014**, *16* (15), 7089–7101.

(65) Sivamurugan, V.; Kazlauskas, K.; Jursenas, S.; Gruodis, A.; Simokaitiene, J.; Grazulevicius, J. V.; Valiyaveettil, S. Synthesis and Photophysical Properties of Glass-Forming Bay-Substituted Perylenediimide Derivatives. *J. Phys. Chem. B* **2010**, *114* (5), 1782–1789.

(66) Oelkrug, D.; Tompert, A.; Egelhaaf, H.-J.; Hanack, M.; Steinhuber, E.; Hohloch, M.; Meier, H.; Stalmach, U. Towards Highly Luminescent Phenylene Vinylene Films. *Synth. Met.* **1996**, *83* (3), 231–237.

(67) Luo, J.; Xie, Z.; Lam, J. W. Y.; Cheng, L.; Tang, B. Z.; Chen, H.; Qiu, C.; Kwok, H. S.; Zhan, X.; Liu, Y.; et al. Aggregation-Induced Emission of 1-Methyl-1,2,3,4,5-Pentaphenylsilole. *Chem. Commun.* **2001**, *0* (18), 1740–1741.

(68) Nie, H.; Huang, J.; Zhao, Z.; Tang, B. Z. Aggregation-Induced Emission Luminogens (AIEgens) for Non-Doped Organic Light-Emitting Diodes; 2016; pp 173–198.

(69) Guo, J.; Li, X.-L.; Nie, H.; Luo, W.; Hu, R.; Qin, A.; Zhao, Z.; Su, S.-J.; Tang, B. Z. Robust Luminescent Materials with Prominent Aggregation-Induced Emission and Thermally Activated Delayed Fluorescence for High-Performance Organic Light-Emitting Diodes. *Chem. Mater.* **2017**, *29* (8), 3623–3631.

(70) Lo, D.; Chang, C.-H.; Krucaite, G.; Volyniuk, D.; Grazulevicius, J. V.; Grigalevicius, S. Sky-Blue Aggregation-Induced Emission Molecules for Non-Doped Organic Light-Emitting Diodes. *J. Mater. Chem. C* **2017**, *5* (24), 6054–6060.

(71) Deng, J.; Xu, Y.; Liu, L.; Feng, C.; Tang, J.; Gao, Y.; Wang, Y.; Yang, B.; Lu, P.; Yang, W.; et al. An Ambipolar Organic Field-Effect Transistor Based on an AIE-Active Single Crystal with a High Mobility Level of 2.0 $Cm^{2} V^{-1} S^{-1}$. *Chem. Commun.* **2016**, *52* (11), 2370–2373.

(72) Zhao, Z.; Gao, S.; Zheng, X.; Zhang, P.; Wu, W.; Kwok, R. T. K.; Xiong, Y.; Leung, N. L. C.; Chen, Y.; Gao, X.; et al. Rational Design of Perylenediimide-Substituted Triphenylethylene to Electron Transporting Aggregation-Induced Emission Luminogens (AIEgens) with High Mobility and Near-Infrared Emission. *Adv. Funct. Mater.* **2018**, *28* (11), 1705609.

(73) Fang, H.-H.; Chen, Q.-D.; Yang, J.; Xia, H.; Gao, B.-R.; Feng, J.; Ma, Y.-G.; Sun, H.-B. Two-Photon Pumped Amplified Spontaneous Emission from Cyano-Substituted Oligo(*P* -Phenylenevinylene) Crystals with Aggregation-Induced Emission Enhancement. *J. Phys. Chem. C* **2010**, *114* (27), 11958–11961.

(74) Cheng, K. H.; Zhong, Y.; Xie, B. Y.; Dong, Y. Q.; Hong, Y.; Sun, J. Z.; Tang, B. Z.; Wong, K. S. Fabrication of and Ultraviolet Lasing in TPE/PMMA Polymer Nanowires. *J. Phys. Chem. C* **2008**, *112* (45), 17507–17511.

(75) Wu, J.; Liu, W.; Ge, J.; Zhang, H.; Wang, P. New Sensing Mechanisms for Design of Fluorescent Chemosensors Emerging in Recent Years. *Chem. Soc. Rev.* **2011**, *40* (7), 3483.

(76) Ding, D.; Li, K.; Liu, B.; Tang, B. Z. Bioprobes Based on AIE Fluorogens. *Acc. Chem. Res.* **2013**, *46* (11), 2441–2453.

(77) Kwok, R. T. K.; Leung, C. W. T.; Lam, J. W. Y.; Tang, B. Z. Biosensing by Luminogens with Aggregation-Induced Emission Characteristics. *Chem.*

Soc. Rev. **2015**, *44* (13), 4228–4238.
(78) Song, P.; Xiang, Y.; Wei, R. R.; Tong, A. A Fluorescent Chemosensor for Cu2+ Detection in Solution Based on Aggregation-Induced Emission and Its Application in Fabricating Cu2+ Test Papers. *J. Lumin.* **2014**, *153*, 215–220.
(79) Zhan, C.; You, X.; Zhang, G.; Zhang, D. Bio-/Chemosensors and Imaging with Aggregation-Induced Emission Luminogens. *Chem. Rec.* **2016**, *16* (4), 2142–2160.
(80) Shustova, N. B.; Ong, T.-C.; Cozzolino, A. F.; Michaelis, V. K.; Griffin, R. G.; Dincă, M. Phenyl Ring Dynamics in a Tetraphenylethylene-Bridged Metal–Organic Framework: Implications for the Mechanism of Aggregation-Induced Emission. *J. Am. Chem. Soc.* **2012**, *134* (36), 15061–15070.
(81) Qin, A.; Lam, J. W. Y.; Tang, B. Z. Luminogenic Polymers with Aggregation-Induced Emission Characteristics. *Prog. Polym. Sci.* **2012**, *37* (1), 182–209.
(82) Feng, X.; Tong, B.; Shen, J.; Shi, J.; Han, T.; Chen, L.; Zhi, J.; Lu, P.; Ma, Y.; Dong, Y. Aggregation-Induced Emission Enhancement of Aryl-Substituted Pyrrole Derivatives. *J. Phys. Chem. B* **2010**, *114* (50), 16731–16736.
(83) He, J.; Xu, B.; Chen, F.; Xia, H.; Li, K.; Ye, L.; Tian, W. Aggregation-Induced Emission in the Crystals of 9,10-Distyrylanthracene Derivatives: The Essential Role of Restricted Intramolecular Torsion. *J. Phys. Chem. C* **2009**, *113* (22), 9892–9899.
(84) An, B. K.; Gierschner, J.; Park, S. Y. ??-Conjugated Cyanostilbene Derivatives: A Unique Self-Assembly Motif for Molecular Nanostructures with Enhanced Emission and Transport. *Acc. Chem. Res.* **2012**, *45* (4), 544–554.
(85) Gao, B.-R.; Wang, H.-Y.; Hao, Y.-W.; Fu, L.-M.; Fang, H.-H.; Jiang, Y.; Wang, L.; Chen, Q.-D.; Xia, H.; Pan, L.-Y.; et al. Time-Resolved Fluorescence Study of Aggregation-Induced Emission Enhancement by Restriction of Intramolecular Charge Transfer State. *J. Phys. Chem. B* **2010**, *114* (1), 128–134.
(86) Dai, Q.; Liu, W.; Zeng, L.; Lee, C.-S.; Wu, J.; Wang, P. Aggregation-Induced Emission Enhancement Materials with Large Red Shifts and Their Self-Assembled Crystal Microstructures. *CrystEngComm* **2011**, *13* (14), 4617.
(87) An, B.-K.; Lee, D.-S.; Lee, J.-S.; Park, Y.-S.; Song, H.-S.; Park, S. Y. Strongly Fluorescent Organogel System Comprising Fibrillar Self-Assembly of a Trifluoromethyl-Based Cyanostilbene Derivative. *J. Am. Chem. Soc.* **2004**, *126* (33), 10232–10233.
(88) Yamaguchi, M.; Ito, S.; Hirose, A.; Tanaka, K.; Chujo, Y. Control of Aggregation-Induced Emission versus Fluorescence Aggregation-Caused Quenching by Bond Existence at a Single Site in Boron Pyridinoiminate Complexes. *Mater. Chem. Front.* **2017**, *1* (8), 1573–1579.
(89) Li, Z.; Dong, Y. Q.; Lam, J. W. Y.; Sun, J.; Qin, A.; Häußler, M.; Dong, Y. P.; Sung, H. H. Y.; Williams, I. D.; Kwok, H. S.; et al. Functionalized Siloles: Versatile Synthesis, Aggregation-Induced Emission, and Sensory and Device Applications. *Adv. Funct. Mater.* **2009**, *19* (6), 905–917.
(90) Gierschner, J.; Park, S. Y. Luminescent Distyrylbenzenes: Tailoring Molecular Structure and Crystalline Morphology. *J. Mater. Chem. C* **2013**, *1* (37), 5818.
(91) Li, C.; Hanif, M.; Li, X.; Zhang, S.; Xie, Z.; Liu, L.; Yang, B.; Su, S.; Ma, Y. Effect of Cyano-Substitution in Distyrylbenzene Derivatives on Their

Fluorescence and Electroluminescence Properties. *J. Mater. Chem. C* **2016**, *4* (31), 7478–7484.
(92) Shustova, N. B.; Ong, T. C.; Cozzolino, A. F.; Michaelis, V. K.; Griffin, R. G.; Dincă, M. Phenyl Ring Dynamics in a Tetraphenylethylene-Bridged Metal-Organic Framework: Implications for the Mechanism of Aggregation-Induced Emission. *J. Am. Chem. Soc.* **2012**, *134* (36), 15061–15070.
(93) Dong, W.; Fei, T.; Palma-Cando, A.; Scherf, U. Aggregation Induced Emission and Amplified Explosive Detection of Tetraphenylethylene-Substituted Polycarbazoles. *Polym. Chem.* **2014**, *5* (13), 4048.
(94) Bao, S.; Wu, Q.; Qin, W.; Yu, Q.; Wang, J.; Liang, G.; Tang, B. Z. Sensitive and Reliable Detection of Glass Transition of Polymers by Fluorescent Probes Based on AIE Luminogens. *Polym. Chem.* **2015**, *6* (18), 3537–3542.
(95) Li, X.-F.; Chi, Z.-G.; Xu, B.-J.; Li, H.-Y.; Zhang, X.-Q.; Zhou, W.; Zhang, Y.; Liu, S.-W.; Xu, J.-R. Synthesis and Characterization of Triphenylethylene Derivatives with Aggregation-Induced Emission Characteristics. *J. Fluoresc.* **2011**, *21* (5), 1969–1977.
(96) Ou, D.; Yu, T.; Yang, Z.; Luan, T.; Mao, Z.; Zhang, Y.; Liu, S.; Xu, J.; Chi, Z.; Bryce, M. R. Combined Aggregation Induced Emission (AIE), Photochromism and Photoresponsive Wettability in Simple Dichloro-Substituted Triphenylethylene Derivatives. *Chem. Sci.* **2016**, *7* (8), 5302–5306.
(97) Gopikrishna, P.; Iyer, P. K. Monosubstituted Dibenzofulvene-Based Luminogens: Aggregation-Induced Emission Enhancement and Dual-State Emission. *J. Phys. Chem. C* **2016**, *120* (46), 26556–26568.
(98) Chang, C.-W.; Bhongale, C. J.; Lee, C.-S.; Huang, W.-K.; Hsu, C.-S.; Diau, E. W.-G. Relaxation Dynamics and Structural Characterization of Organic Nanobelts with Aggregation-Induced Emission. *J. Phys. Chem. C* **2012**, *116* (28), 15146–15154.
(99) Feng, Y.; Wang, N.; Ju, H. Highly Efficient Electrochemiluminescence of Cyanovinylene-Contained Polymer Dots in Aqueous Medium and Its Application in Imaging Analysis. *Anal. Chem.* **2018**, *90* (2), 1202–1208.
(100) Yoon, S.-J.; Park, S. Polymorphic and Mechanochromic Luminescence Modulation in the Highly Emissive Dicyanodistyrylbenzene Crystal: Secondary Bonding Interaction in Molecular Stacking Assembly. *J. Mater. Chem.* **2011**, *21* (23), 8338.
(101) Chung, J. W.; You, Y.; Huh, H. S.; An, B.-K.; Yoon, S.-J.; Kim, S. H.; Lee, S. W.; Park, S. Y. Shear- and UV-Induced Fluorescence Switching in Stilbenic π-Dimer Crystals Powered by Reversible [2 + 2] Cycloaddition. *J. Am. Chem. Soc.* **2009**, *131* (23), 8163–8172.
(102) Palakollu, V.; Kanvah, S. α-Cyanostilbene Based Fluorophores: Aggregation-Induced Enhanced Emission, Solvatochromism and the pH Effect. *New J. Chem.* **2014**, *38* (12), 5736–5746.
(103) Qian, L.; Tong, B.; Shen, J.; Shi, J.; Zhi, J.; Dong, Y.; Yang, F.; Dong, Y.; Lam, J. W. Y.; Liu, Y.; et al. Crystallization-Induced Emission Enhancement in a Phosphorus-Containing Heterocyclic Luminogen. *J. Phys. Chem. B* **2009**, *113* (27), 9098–9103.
(104) Zhang, Y.; Sun, J.; Zhuang, G.; Ouyang, M.; Yu, Z.; Cao, F.; Pan, G.; Tang, P.; Zhang, C.; Ma, Y. Heating and Mechanical Force-Induced Luminescence On–off Switching of Arylamine Derivatives with Highly Distorted

Structures. *J. Mater. Chem. C* **2014**, *2* (1), 195–200.
(105) Gong, Y.; Tan, Y.; Liu, J.; Lu, P.; Feng, C.; Yuan, W. Z.; Lu, Y.; Sun, J. Z.; He, G.; Zhang, Y. Twisted D–π–A Solid Emitters: Efficient Emission and High Contrast Mechanochromism. *Chem. Commun.* **2013**, *49* (38), 4009.
(106) Zhang, H. Y.; Zhang, Z. L.; Ye, K. Q.; Zhang, J. Y.; Wang, Y. Organic Crystals with Tunable Emission Colors Based on a Single Organic Molecule and Different Molecular Packing Structures. *Adv. Mater.* **2006**, *18* (18), 2369–2372.
(107) Kunzelman, J.; Crenshaw, B. R.; Weder, C. Self-Assembly of Chromogenic Dyes—a New Mechanism for Humidity Sensors. *J. Mater. Chem.* **2007**, *17* (29), 2989–2991.
(108) Grzelczak, M.; Vermant, J.; Furst, E. M.; Liz-Marzán, L. M. Directed Self-Assembly of Nanoparticles. *ACS Nano* **2010**, *4* (7), 3591–3605.
(109) Sagara, Y.; Kato, T. Mechanically Induced Luminescence Changes in Molecular Assemblies. *Nat. Chem.* **2009**, *1* (8), 605–610.
(110) Luo, X.; Li, J.; Li, C.; Heng, L.; Dong, Y. Q.; Liu, Z.; Bo, Z.; Tang, B. Z. Reversible Switching of the Emission of Diphenyldibenzofulvenes by Thermal and Mechanical Stimuli. *Adv. Mater.* **2011**, *23* (29), 3261–3265.
(111) Forrest, S. R. The Path to Ubiquitous and Low-Cost Organic Electronic Appliances on Plastic. *Nature* **2004**, *428* (6986), 911–918.
(112) Kozlov, V. G.; Forrest, S. R. Lasing Action in Organic Semiconductor Thin Films. *Curr. Opin. Solid State Mater. Sci.* **1999**, *4* (2), 203–208.
(113) Grivas, C.; Pollnau, M. Organic Solid-State Integrated Amplifiers and Lasers. *Laser Photon. Rev.* **2012**, *6* (4), 419–462.
(114) Karnutsch, C.; Pflumm, C.; Heliotis, G.; deMello, J. C.; Bradley, D. D. C.; Wang, J.; Weimann, T.; Haug, V.; Gärtner, C.; Lemmer, U. Improved Organic Semiconductor Lasers Based on a Mixed-Order Distributed Feedback Resonator Design. *Appl. Phys. Lett.* **2007**, *90* (13), 131104.
(115) Tessler, N. Lasers Based on Semiconducting Organic Materials. *Adv. Mater.* **1999**, *11* (5), 363–370.
(116) Kim, Y. C.; Lee, T.-W.; Park, O. O.; Kim, C. Y.; Cho, H. N. Low-Threshold Amplified Spontaneous Emission in a Fluorene-Based Liquid Crystalline Polymer Blend. *Adv. Mater.* **2001**, *13* (9), 646–649.
(117) Baldo, M. A.; Holmes, R. J.; Forrest, S. R. Prospects for Electrically Pumped Organic Lasers. *Phys. Rev. B* **2002**, *66* (3), 35321.
(118) Pope, M.; Swenberg, C. E. *Electronic Processes in Organic Crystals and Polymers*; Oxford University Press, 1999.
(119) Takenobu, T.; Bisri, S. Z.; Takahashi, T.; Yahiro, M.; Adachi, C.; Iwasa, Y. High Current Density in Light-Emitting Transistors of Organic Single Crystals. *Phys. Rev. Lett.* **2008**, *100* (6), 66601.
(120) Komori, T.; Nakanotani, H.; Yasuda, T.; Adachi, C. Light-Emitting Organic Field-Effect Transistors Based on Highly Luminescent Single Crystals of Thiophene/phenylene Co-Oligomers. *J. Mater. Chem. C* **2014**, *2* (25), 4918.
(121) Fang, H.-H.; Yang, J.; Ding, R.; Chen, Q.-D.; Wang, L.; Xia, H.; Feng, J.; Ma, Y.-G.; Sun, H.-B. Polarization Dependent Two-Photon Properties in an Organic Crystal. *Appl. Phys. Lett.* **2010**, *97* (10), 101101.
(122) Kabe, R.; Nakanotani, H.; Sakanoue, T.; Yahiro, M.; Adachi, C. Effect of Molecular Morphology on Amplified Spontaneous Emission of Bis-Styrylbenzene Derivatives. *Adv. Mater.* **2009**, *21* (40), 4034–4038.

(123) Yoon, S.-J.; Park, S. Polymorphic and Mechanochromic Luminescence Modulation in the Highly Emissive Dicyanodistyrylbenzene Crystal: Secondary Bonding Interaction in Molecular Stacking Assembly. *J. Mater. Chem.* **2011**, *21* (23), 8338.
(124) Xu, B.; Fang, H.; Dong, Y.; Chen, F.; Chen, Q.; Sun, H.; Tian, W. Solid State Emission Enhancement of 9,10-Distyrylanthracene Derivatives and Amplified Spontaneous Emission from a Large Single Crystal. *New J. Chem.* **2010**, *34* (9), 1838.
(125) Camposeo, A.; Polo, M.; Del Carro, P.; Silvestri, L.; Tavazzi, S.; Pisignano, D. Random Lasing in an Organic Light-Emitting Crystal and Its Interplay with Vertical Cavity Feedback. *Laser Photon. Rev.* **2014**, *8* (5), 785–791.
(126) Wang, K.; Zhang, H.; Chen, S.; Yang, G.; Zhang, J.; Tian, W.; Su, Z.; Wang, Y. Organic Polymorphs: One-Compound-Based Crystals with Molecular-Conformation- and Packing-Dependent Luminescent Properties. *Adv. Mater.* **2014**, *26* (35), 6168–6173.
(127) Zhu, X.; Gindre, D.; Mercier, N.; Frère, P.; Nunzi, J.-M. Stimulated Emission from a Needle-like Single Crystal of an End-Capped Fluorene/Phenylene Co-Oligomer. *Adv. Mater.* **2003**, *15* (11), 906–909.
(128) Nakanotani, H.; Akiyama, S.; Ohnishi, D.; Moriwake, M.; Yahiro, M.; Yoshihara, T.; Tobita, S.; Adachi, C. Extremely Low-Threshold Amplified Spontaneous Emission of 9,9′-Spirobifluorene Derivatives and Electroluminescence from Field-Effect Transistor Structure. *Adv. Funct. Mater.* **2007**, *17* (14), 2328–2335.
(129) Ribierre, J.-C.; Zhao, L.; Inoue, M.; Schwartz, P.-O.; Kim, J.-H.; Yoshida, K.; Sandanayaka, A. S. D.; Nakanotani, H.; Mager, L.; Méry, S.; et al. Low Threshold Amplified Spontaneous Emission and Ambipolar Charge Transport in Non-Volatile Liquid Fluorene Derivatives. *Chem. Commun.* **2016**, *52* (15), 3103–3106.
(130) Inoue, M.; Matsushima, T.; Adachi, C. Low Amplified Spontaneous Emission Threshold and Suppression of Electroluminescence Efficiency Roll-off in Layers Doped with ter(9,9′-Spirobifluorene). *Appl. Phys. Lett.* **2016**, *108* (13), 133302.
(131) Kim, D.-H.; Sandanayaka, A. S. D.; Zhao, L.; Pitrat, D.; Mulatier, J. C.; Matsushima, T.; Andraud, C.; Ribierre, J. C.; Adachi, C. Extremely Low Amplified Spontaneous Emission Threshold and Blue Electroluminescence from a Spin-Coated Octafluorene Neat Film. *Appl. Phys. Lett.* **2017**, *110* (2), 23303.
(132) Sandanayaka, A. S. D.; Matsushima, T.; Bencheikh, F.; Yoshida, K.; Inoue, M.; Fujihara, T.; Goushi, K.; Ribierre, J.-C.; Adachi, C. Toward Continuous-Wave Operation of Organic Semiconductor Lasers. *Sci. Adv.* **2017**, *3* (4), e1602570.
(133) Varghese, S.; Park, S. K.; Casado, S.; Resel, R.; Wannemacher, R.; Lüer, L.; Park, S. Y.; Gierschner, J. Polymorphism and Amplified Spontaneous Emission in a Dicyano-Distyrylbenzene Derivative with Multiple Trifluoromethyl Substituents: Intermolecular Interactions in Play. *Adv. Funct. Mater.* **2016**, *26* (14), 2349–2356.
(134) Wang, H.; Li, F.; Gao, B.; Xie, Z.; Liu, S.; Wang, C.; Hu, D.; Shen, F.; Xu, Y.; Shang, H.; et al. Doped Organic Crystals with High Efficiency, Color-Tunable Emission toward Laser Application. *Cryst. Growth Des.* **2009**, *9*

(11), 4945–4950.
(135) de Mello, J. C.; Wittmann, H. F.; Friend, R. H. An Improved Experimental Determination of External Photoluminescence Quantum Efficiency. *Adv. Mater.* **1997**, *9* (3), 230–232.
(136) Shaklee, K. L.; Leheny, R. F. DIRECT DETERMINATION OF OPTICAL GAIN IN SEMICONDUCTOR CRYSTALS. *Appl. Phys. Lett.* **1971**, *18* (11), 475–477.
(137) Frisch, Æ. Gaussian 09W Reference. **2009**.
(138) An, B.-K.; Gierschner, J.; Park, S. Y. π-Conjugated Cyanostilbene Derivatives: A Unique Self-Assembly Motif for Molecular Nanostructures with Enhanced Emission and Transport. *Acc. Chem. Res.* **2012**, *45* (4), 544–554.
(139) Willy, B.; Müller, T. J. J. Regioselective Three-Component Synthesis of Highly Fluorescent 1,3,5-Trisubstituted Pyrazoles. *European J. Org. Chem.* **2008**, *2008* (24), 4157–4168.
(140) Peng, Q.; Yi, Y.; Shuai, Z.; Shao, J. Toward Quantitative Prediction of Molecular Fluorescence Quantum Efficiency: Role of Duschinsky Rotation. *J. Am. Chem. Soc.* **2007**, *129* (30), 9333–9339.
(141) Arbačiauskiene, E.; Kazlauskas, K.; Miasojedovas, A.; Juršenas, S.; Jankauskas, V.; Holzer, W.; Getautis, V.; Šačkus, A. Pyrazolyl-Substituted Polyconjugated Molecules for Optoelectronic Applications. *Dye. Pigment.* **2010**, *85* (3), 79–85.
(142) Arbačiauskiene, E.; Kazlauskas, K.; Miasojedovas, A.; Juršenas, S.; Jankauskas, V.; Holzer, W.; Getautis, V.; Šačkus, A. Multifunctional Polyconjugated Molecules with Carbazolyl and Pyrazolyl Moieties for Optoelectronic Applications. *Synth. Met.* **2010**, *160* (5–6), 490–498.
(143) Krotkus, S.; Kazlauskas, K.; Miasojedovas, A.; Gruodis, A.; Tomkeviciene, A.; Grazulevicius, J. V.; Jursenas, S. Pyrenyl-Functionalized Fluorene and Carbazole Derivatives as Blue Light Emitters. *J. Phys. Chem. C* **2012**, *116* (13), 7561–7572.
(144) Gierschner, J.; Oelkrug, D.; Egelhaaf, H. Highly Emissive H Aggregates or Aggregation-Induced Emission Quenching? The Photophysics of All-Trans Para -Distyrylbenzene. *J. Phys. Chem. Lett.* **2013**, *4*, 2686–2697.
(145) An, B. K.; Gihm, S. H.; Chung, J. W.; Park, C. R.; Kwon, S. K.; Park, S. Y. Color-Tuned Highly Fluorescent Organic Nanowires/nanofabrics: Easy Massive Fabrication and Molecular Structural Origin. *J. Am. Chem. Soc.* **2009**, *131* (11), 3950–3957.
(146) Főrster, T. 10th Spiers Memorial Lecture. Transfer Mechanisms of Electronic Excitation. *Discuss. Faraday Soc.* **1959**, *27* (0), 7–17.
(147) M. J. Frisch, G. W. Trucks, H. B. Schlegel, G. E. Scuseria, M. A. Robb, J. R. Cheeseman, G. Scalmani, V. Barone, G. A. Petersson, H. Nakatsuji, X. Li, M. Caricato, A. Marenich, J. Bloino, B. G. Janesko, R. Gomperts, B. Mennucci, H. P. Hratchian, J. V. Ort, and D. J. F. Fast Surface Crystallization of Molecular Glasses: Creation of Depletion Zones by Surface Diffusion and Crystallization Flux. *J. Phys. Chem. B* **2015**, *119* (7), 3304–3311.
(148) Gnutzmann, T.; Rademann, K.; Emmerling, F. Fast Crystallization of Organic Glass Formers. *Chem. Commun.* **2012**, *48* (11), 1638–1640.
(149) M. Gunn, E.; A. Guzei, I.; Yu, L. Does Crystal Density Control Fast Surface Crystal Growth in Glasses? A Study with Polymorphs. *Cryst. Growth Des.* **2011**, *11* (9), 3979–3984.

(150) Hasebe, M.; Musumeci, D.; Powell, C. T.; Cai, T.; Gunn, E.; Zhu, L.; Yu, L. Fast Surface Crystal Growth on Molecular Glasses and Its Termination by the Onset of Fluidity. *J. Phys. Chem. B* **2014**, *118* (27), 7638–7646.
(151) Karlsson, O. J.; Stubbs, J. M.; Karlsson, L. E.; Sundberg, D. C. Estimating Diffusion Coefficients for Small Molecules in Polymers and Polymer Solutions. *Polymer (Guildf).* **2001**, *42* (11), 4915–4923.
(152) Kinami, M.; Crenshaw, B. R.; Weder, C. Polyesters with Built-in Threshold Temperature and Deformation Sensors. *Chem. Mater.* **2006**, *18* (4), 946–955.
(153) Pucci, A.; Di Cuia, F.; Signori, F.; Ruggeri, G. Bis(benzoxazolyl)stilbene Excimers as Temperature and Deformation Sensors for Biodegradable poly(1,4-Butylene Succinate) Films. *J. Mater. Chem.* **2007**, *17* (8), 783.
(154) Jang, H.-S.; Wang, Y.; Lei, Y.; Nieh, M.-P. Controllable Formation of Pyrene (C 16 H 10) Excimers in Polystyrene/Tetrabutylammonium Hexafluorophosphate Films through Solvent Vapor and Temperature Annealing. *J. Phys. Chem. C* **2013**, *117* (3), 1428–1435.
(155) Chung, J. W.; An, B.-K.; Hirato, F.; Kim, J. H.; Jinnai, H.; Park, S. Y. Selected-Area in Situ Generation of Highly Fluorescent Organic Nanowires Embedded in a Polymer Film: The Solvent-Vapor-Induced Self-Assembly Process. *J. Mater. Chem.* **2010**, *20* (36), 7715.
(156) An, B. K.; Kwon, S. K.; Park, S. Y. Photopatterned Arrays of Fluorescent Organic Nanoparticles. *Angew. Chemie - Int. Ed.* **2007**, *46* (12), 1978–1982.
(157) Ding, Z.; Xing, R.; Sun, Y.; Zheng, L.; Wang, X.; Ding, J.; Wang, L.; Han, Y. Effects of Molecular Structures and Solvent Properties on the Self-Assembly of Carbazole-Based Conjugated Dendrimers by Solvent Vapor Annealing. *RSC Adv.* **2013**, *3* (21), 8037.
(158) Wang, Y.; Parkin, S. R.; Gierschner, J.; Watson, M. D. Highly Fluorinated Benzobisbenzothiophenes. *Org. Lett.* **2008**, *10* (15), 3307–3310.
(159) Liang, H.; Wang, X.; Zhang, X.; Ge, Z.; Ouyang, X.; Wang, S. Efficient Tuning of Electroluminescence from Sky-Blue to Deep-Blue by Changing the Constitution of Spirobenzofluorene Derivatives. *Dye. Pigment.* **2014**, *108*, 57–63.
(160) Kim, K.-S.; Jeon, Y.-M.; Kim, J.-W.; Lee, C.-W.; Gong, M.-S. Blue Light-Emitting OLED Using New Spiro[fluorene-7,9′-Benzofluorene] Host and Dopant Materials. *Org. Electron.* **2008**, *9* (5), 797–804.
(161) Tomkeviciene, A.; Grazulevicius, J. V.; Kazlauskas, K.; Gruodis, A.; Jursenas, S.; Ke, T.-H.; Wu, C.-C. Impact of Linking Topology on the Properties of Carbazole Trimers and Dimers. *J. Phys. Chem. C* **2011**, *115* (11), 4887–4897.
(162) Dias, F. B.; Bourdakos, K. N.; Jankus, V.; Moss, K. C.; Kamtekar, K. T.; Bhalla, V.; Santos, J.; Bryce, M. R.; Monkman, A. P. Triplet Harvesting with 100% Efficiency by Way of Thermally Activated Delayed Fluorescence in Charge Transfer OLED Emitters. *Adv. Mater.* **2013**, *25* (27), 3707–3714.
(163) Köhler, A.; Bässler, H. Triplet States in Organic Semiconductors. *Mater. Sci. Eng. R Reports* **2009**, *66* (4–6), 71–109.
(164) Sun, Y.; Giebink, N. C.; Kanno, H.; Ma, B.; Thompson, M. E.; Forrest, S. R. Management of Singlet and Triplet Excitons for Efficient White Organic Light-Emitting Devices. *Nature* **2006**, *440* (7086), 908–912.
(165) Kersting, R.; Mollay, B.; Rusch, M.; Wenisch, J.; Leising, G.; Kauffmann, H. F.

Femtosecond Site-Selective Probing of Energy Relaxing Excitons in Poly(phenylenevinylene): Luminescence Dynamics and Lifetime Spectra. *J. Chem. Phys.* **1998**, *106* (7), 2850.
(166) Karpicz, R.; Puzinas, S.; Krotkus, S.; Kazlauskas, K.; Jursenas, S.; Grazulevicius, J. V.; Grigalevicius, S.; Gulbinas, V. Impact of Intramolecular Twisting and Exciton Migration on Emission Efficiency of Multifunctional Fluorene-Benzothiadiazole-Carbazole Compounds. *J. Chem. Phys.* **2011**, *134* (20), 1–9.
(167) Cekaviciute, M.; Simokaitiene, J.; Jankauskas, V.; Raisys, S.; Kazlauskas, K.; Jursenas, S.; Grazulevicius, J. V. Structure-Properties Relationship of Phenylethenyl-Substituted Triphenylamines. *J. Phys. Chem. C* **2013**, *117* (16), 7973–7980.
(168) Malinauskas, T.; Daskeviciene, M.; Bubniene, G.; Petrikyte, I.; Raisys, S.; Kazlauskas, K.; Gaidelis, V.; Jankauskas, V.; Maldzius, R.; Jursenas, S.; et al. Phenylethenyl-Substituted Triphenylamines: Efficient, Easily Obtainable, and Inexpensive Hole-Transporting Materials. *Chem. - A Eur. J.* **2013**, *19* (44), 15044–15056.
(169) Calzado, E. M.; Villalvilla, J. M.; Boj, P. G.; Quintana, J. A.; Gómez, R.; Segura, J. L.; Díaz-García, M. A. Effect of Structural Modifications in the Spectral and Laser Properties of Perylenediimide Derivatives. *J. Phys. Chem. C* **2007**, *111* (36), 13595–13605.
(170) Camposeo, A.; Mele, E.; Persano, L.; Pisignano, D.; Cingolani, R. Role of Doping Concentration on the Competition between Amplified Spontaneous Emission and Nonradiative Energy Transfer in Blends of Conjugated Polymers. *Phys. Rev. B* **2006**, *73* (16), 165201.
(171) Aimono, T.; Kawamura, Y.; Goushi, K.; Yamamoto, H.; Sasabe, H.; Adachi, C. 100% Fluorescence Efficiency of 4,4[sup ']-bis[(N-Carbazole)styryl]biphenyl in a Solid Film and the Very Low Amplified Spontaneous Emission Threshold. *Appl. Phys. Lett.* **2005**, *86* (7), 71110.
(172) Wallikewitz, B. H.; Hertel, D.; Meerholz, K. Cross-Linkable Polyspirobifluorenes: A Material Class Featuring Good OLED Performance and Low Amplified Spontaneous Emission Thresholds. *Chem. Mater.* **2009**, *21* (13), 2912–2919.
(173) Choi, E. Y.; Mazur, L.; Mager, L.; Gwon, M.; Pitrat, D.; Mulatier, J. C.; Monnereau, C.; Fort, A.; Attias, A. J.; Dorkenoo, K.; et al. Photophysical, Amplified Spontaneous Emission and Charge Transport Properties of Oligofluorene Derivatives in Thin Films. *Phys. Chem. Chem. Phys.* **2014**, *16* (32), 16941–16956.
(174) Tsiminis, G.; Wang, Y.; Shaw, P. E.; Kanibolotsky, A. L.; Perepichka, I. F.; Dawson, M. D.; Skabara, P. J.; Turnbull, G. A.; Samuel, I. D. W. Low-Threshold Organic Laser Based on an Oligofluorene Truxene with Low Optical Losses. *Appl. Phys. Lett.* **2009**, *94* (24), 243304.
(175) Ribierre, J. C.; Tsiminis, G.; Richardson, S.; Turnbull, G. A.; Samuel, I. D. W.; Barcena, H. S.; Burn, P. L. Amplified Spontaneous Emission and Lasing Properties of Bisfluorene-Cored Dendrimers. *Appl. Phys. Lett.* **2007**, *91* (8), 81108.
(176) Ning, S.; Wu, Z.; Dong, H.; Yuan, F.; Ma, L.; Yu, Y.; Jiao, B.; Hou, X. Enhancement of Amplified Spontaneous Emission in Organic Gain Media by the Metallic Film. *Org. Electron.* **2014**, *15* (9), 2052–2058.

(177) Rabbani-Haghighi, H.; Forget, S.; Chénais, S.; Siove, A.; Castex, M.-C.; Ishow, E. Laser Operation in Nondoped Thin Films Made of a Small-Molecule Organic Red-Emitter. *Appl. Phys. Lett.* **2009**, *95* (3), 33305.
(178) Yap, B. K.; Xia, R.; Campoy-Quiles, M.; Stavrinou, P. N.; Bradley, D. D. C. Simultaneous Optimization of Charge-Carrier Mobility and Optical Gain in Semiconducting Polymer Films. *Nat. Mater.* **2008**, *7* (5), 376–380.
(179) Heliotis, G.; Bradley, D. D. C.; Turnbull, G. A.; Samuel, I. D. W. Light Amplification and Gain in Polyfluorene Waveguides. *Appl. Phys. Lett.* **2002**, *81* (3), 415–417.
(180) Kranzelbinder, G.; Leising, G. Organic Solid-State Lasers. *Reports Prog. Phys.* **2000**, *63* (5), 729–762.
(181) Kazlauskas, K.; Kreiza, G.; Bobrovas, O.; Adomeniene, O.; Adomenas, P.; Jankauskas, V.; Jursenas, S. Fluorene- and Benzofluorene-Cored Oligomers as Low Threshold and High Gain Amplifying Media. *Appl. Phys. Lett.* **2015**, *107* (4).
(182) Kuehne, A. J. C.; Gather, M. C. Organic Lasers: Recent Developments on Materials, Device Geometries, and Fabrication Techniques. *Chem. Rev.* **2016**, *116* (21), 12823–12864.
(183) Karabunarliev, S.; Bittner, E. R.; Baumgarten, M. Franck–Condon Spectra and Electron-Libration Coupling in Para-Polyphenyls. *J. Chem. Phys.* **2001**, *114* (13), 5863–5870.
(184) Venkataraman, L.; Klare, J. E.; Nuckolls, C.; Hybertsen, M. S.; Steigerwald, M. L. Dependence of Single-Molecule Junction Conductance on Molecular Conformation. *Nature* **2006**, *442* (7105), 904–907.
(185) Gallaher, J. K.; Chen, K.; Huff, G. S.; Prasad, S. K. K.; Gordon, K. C.; Hodgkiss, J. M. Evolution of Nonmirror Image Fluorescence Spectra in Conjugated Polymers and Oligomers. *J. Phys. Chem. Lett.* **2016**, *7* (17), 3307–3312.
(186) Varghese, S.; Park, S. K.; Casado, S.; Fischer, R. C.; Resel, R.; Milián-Medina, B.; Wannemacher, R.; Park, S. Y.; Gierschner, J. Stimulated Emission Properties of Sterically Modified Distyrylbenzene-Based H-Aggregate Single Crystals. *J. Phys. Chem. Lett.* **2013**, *4* (10), 1597–1602.
(187) Spano, F. C. The Spectral Signatures of Frenkel Polarons in H- and J-Aggregates. *Acc. Chem. Res.* **2010**, *43* (3), 429–439.
(188) Kreiza, G.; Baronas, P.; Radiunas, E.; Adomėnas, P.; Adomėnienė, O.; Kazlauskas, K.; Ribierre, J.-C.; Adachi, C.; Juršėnas, S. Bifluorene Single Crystals with Extremely Low-Threshold Amplified Spontaneous Emission. *Adv. Opt. Mater.* **2017**, *5* (5), 1600823.
(189) Baronas, P.; Kreiza, G.; Adomenas, P.; Adomeniene, O.; Kazlauskas, K.; Ribierre, J.-C.; Adachi, C.; Juršėnas, S. Low-Threshold Light Amplification in Bifluorene Single Crystals: Role of the Trap States. *ACS Appl. Mater. Interfaces* **2018**, *10* (3).
(190) Karl, N. Laser Emission from an Organic Molecular Crystal. *Phys. status solidi* **1972**, *13* (2), 651–655.